

# Magnetic substitution in $\text{CePt}_2\text{Si}_2$ and $\text{CeCu}_5\text{In}$ Kondo lattice

By

Zwelithini Melford Mahlubi

A thesis submitted

To

The faculty of Science, University of the Western Cape,



In fulfilment of the requirements for the degree of

**Magister Scientiae (MSc)**

Supervisor: Prof. M.B.Tchoula Tchokonté

Cape Town 2013

# Contents

---

Declaration.....	iv
Abstract.....	v
Dedication.....	vi
Acknowledgements.....	vii
List of figures.....	1
List of tables.....	6

## I Theoretical background

I-1	Introduction.....	8
I-2	Rare earth (RE) elements and rare earth intermetallic compounds.....	8
I-3	Overview of heavy-fermion and Kondo systems.....	12
	I-3-1 Competition between RKKY interaction and Kondo effect.....	14
	I-3-2 Kondo effect.....	16
I-4	Electrical resistivity and magnetic properties of heavy-Fermions and Kondo systems.....	18
	I-4-1 Electrical resistivity.....	19
	I-4-1-a: Magnetic resistivity of RE intermetallic compounds.....	22
	I-4-1-b: Magnetic resistivity of Kondo and HF systems.....	25
	I-4-2: Magnetic susceptibility and magnetization.....	30
I-5	Specific heat capacity.....	34
	<i>References</i> .....	36

## II Experimental techniques

II-1	Sample preparation.....	40
------	-------------------------	----

II-2	Sample characterization.....	42
II-3	Electrical resistivity measurements.....	44
II-4	Magnetic susceptibility and magnetization measurements.....	47

### **III Theoretical overview of CePt<sub>2</sub>Si<sub>2</sub> and CeCu<sub>5</sub>In**

III-1	CePt <sub>2</sub> Si <sub>2</sub> compound.....	49
III-2	CeCu <sub>5</sub> In compound.....	50
	<i>References</i> .....	52

### **IV Competition between RKKY interaction and the Kondo effect in (Ce<sub>1-x</sub>RE<sub>x</sub>)Pt<sub>2</sub>Si<sub>2</sub>, RE = Tb, Dy**

IV-1	X-ray diffraction.....	55
	IV-1-1 Structural characterization.....	55
	IV-1-2 Lattice parameters.....	55
IV-2	Electrical resistivity.....	59
IV-3	Magnetization and magnetic susceptibility.....	66
	IV-3-1 Magnetization.....	66
	IV-3-2 Magnetic susceptibility.....	68
IV-4	Conclusion.....	74
	<i>References</i> .....	75

### **V Kondo behaviour in (Ce<sub>1-x</sub>Tb<sub>x</sub>)Cu<sub>5</sub>In**

V-1	X-ray diffraction.....	76
	V-1-1 Structural characterization.....	76

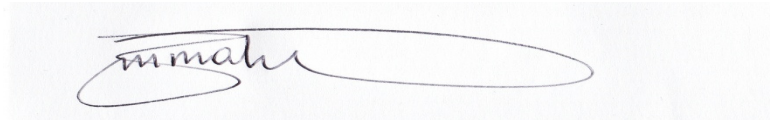
V-1-2	Lattice parameters.....	76
V-2	Electrical resistivity.....	80
V-3	Magnetization and magnetic susceptibility .....	85
V-3	Conclusion.....	88
	<i>References</i> .....	89
<b>VI</b>	<b>Conclusion</b> .....	90





## Declaration

I declare that this thesis is my own, independent body of work, conducted in institutions as explicitly stated on this thesis. This work is submitted in fulfilment of Magister Scientiae at the University of the Western Cape and this work was never done before, for this degree.



.....  
Zwelithini Melford Mahlubi

.....Day of.....2013



## Abstract

In the past few decades, the studies of f-electron materials have revealed unusual physical properties such as Fermi-liquid, non-Fermi-liquid behaviour at low temperatures, heavy-Fermion behaviour, valence fluctuation, Kondo effect, superconducting and magnetic ordering. These materials include binary and ternary compounds and alloys with Cerium (Ce) or Ytterbium (Yb) based rare earth elements or Uranium (U) based actinide element. In these systems the localized magnetic moments formed by Ce, Yb or U ions transform the electronic properties of these compounds leading to quasiparticles with masses in excess to 1000 times the bare electron mass. These materials are known as heavy-fermion materials.

Two well known heavy – Fermion compounds with Ce based rare earth elements of interest in this thesis are  $\text{CePt}_2\text{Si}_2$  and  $\text{CeCu}_5\text{In}$ . The effect of substituting Ce with moment bearing Tb or Dy in these two compounds, are reported through measurements of electrical resistivity, magnetic susceptibility and magnetization. The three alloy systems  $(\text{Ce}_{1-x}\text{RE}_x)\text{Pt}_2\text{Si}_2$  (RE = Tb, Dy) and  $(\text{Ce}_{1-x}\text{Tb}_x)\text{Cu}_5\text{In}$  under investigation in the present thesis, was synthesized and characterized by x-ray diffraction. The alloy systems  $(\text{Ce}_{1-x}\text{RE}_x)\text{Pt}_2\text{Si}_2$  (RE = Tb, Dy,  $0 \leq x \leq 1$ ) formed a single phase in the  $P4/nmm$  tetragonal  $\text{CaBe}_2\text{Ge}_2$  – type structure across the whole series while the  $(\text{Ce}_{1-x}\text{Tb}_x)\text{Cu}_5\text{In}$  alloy system formed a single phase in the  $Pnma$  orthorhombic  $\text{CeCu}_6$  – type crystal structure up to 40% Ce substitution. The physical properties of these systems is reported and discussed through the measurements of electrical resistivity, magnetic susceptibility and magnetization. The variables of this study are: the doping concentration of Tb or Dy, the applied magnetic field and the sample temperature. Electrical resistivity studies for all the systems revealed coherence effect at Ce – rich alloys ( $0 \leq x \leq 0.2$ ) and single-ion Kondo scattering with further increased RE concentration ( $x \geq 0.3$ ). The magnetic property studies indicate antiferromagnetic ordering only for the  $(\text{Ce}_{1-x}\text{RE}_x)\text{Pt}_2\text{Si}_2$  alloy system in the concentration range  $0.7 \leq x \leq 1$ .

The present thesis is comprised of six chapters, which are arranged as follows: The first chapter deals with the theoretical background of the physical properties of Ce based intermetallics compounds and alloys. Experimental techniques constitutes chapter II and explains the techniques used in this study. The theoretical overview of the two parent compounds of interest in this thesis ( $\text{CePt}_2\text{Si}_2$  and  $\text{CeCu}_5\text{In}$ ) is presented in chapter III. The fourth and the fifth chapters of this study deals with results and discussion. The thesis is completed with a conclusion in chapter six.

# Dedication

To my family (my mother and sisters), who have been there for me all the way through it all. My wife (i.e., who was my friend then) and to my brother and a friend “late Nyaniso Nduku”, who made Cape Town a home away from home and who inspired me through his tireless efforts and success in his studies.



## Acknowledgements

Most of this work was done at the University of Johannesburg, Physics Department and University of the Western Cape, Physics Department. A few measurements were done at iThemba LABS as well as the Institute of Low Temperature and Structural research, Polish Academy of Sciences. This work was generously supported by the National Research Foundation (NRF) and University of the Western Cape through the Research Division, and also The Physics Department through the Extended Curriculum Programme (ECP-PHY151/152) under the leadership of Professor Delia Marshall. Had it not been for your generous financial support, my work would not have reached this far.

In times as these, it is appropriate to quote the following “There is no such thing as a self-made man. We reach our goals only with the help of others”. Before I continue thanking everyone who have made a significant contribution towards the success of this work, I would like to extend my sincere words of gratitude to my supervisor Professor Moise Bertin Tchoula Tchokonté who has consistently been a pioneer of this work, irrespective of all the challenges faced. A special thanks to Mr J. L. Snyman, Dr C. J. Sheppard and Prof A. M. Strydom from the University of Johannesburg, Physics Department, Prof D. Kaczorowski from the Institute of Low Temperature and Structural Research, Polish Academy of Sciences as well as Prof T. Doyle from iThemba LABS, for their phenomenal technical assistance in the measurements of magnetic properties. I would like to extend my gratitude to Dr R. Burcher from iThemba LABS, Material Research Group, for X-ray diffraction measurements. To the MaNus/MatSCI 2009 class, guys if it had not been for our team work, I would not have reached this far.

To my friends, Phutuma Mpangele (now my wife), Xolani Mbongozi, Phozisa Magxala who is now known as Lilitha Phozisa Fani, Ntombovuyo Booi, Nangamso Nyangiwe and Luyanda Mafumba, thanks very much for your moral support and for inspiring me. To my very special sister from church and a friend “Sibongile Bantwini” who is based in Johannesburg, thank you very much for being there for me when I needed you most and my Pastor Dr H. S. Mawaba. To my mother “Mangwanya Mahlubi”, every time I ever come to you seeking parental advice I always notice two things, you believe in me undoubtedly and you never limit me. Last but not least, my sisters “Nokubonga and Noxolisa Mahlubi” who have been there for me in all aspects. Unless the LORD builds the house, its builders labor in vain. Unless the LORD watches over the city, the watchmen stand guard in vain (Ps 127:1).

## List of figures

<b>Figure I-1:</b>	Atomic volume of the RE elements and their crystal structure at room temperature.....	9
<b>Figure I-2:</b>	The classification of CKS by the relation between two characteristic temperatures $T_K$ and $T_{RKKY}$ , $T_M$ is the magnetic transition temperature.....	15
<b>Figure I-3:</b>	The temperature variation of electrical resistivity in the range $4 \leq T \leq 295$ K for compounds in the pseudo-ternary alloy system $(Ce_{1-x}La_x)Cu_5In$ ( $0 \leq x \leq 1$ ). The inset shows the Fermi-liquid behaviour of the parent compound $CeCu_5In$ , where the line represent the LSQ fit of the measured data to $\rho(T) - \rho_0 = AT^2$ .....	17
<b>Figure I-4:</b>	The standard geometry for the resistivity measurements. ....	21
<b>Figure I-5:</b>	Schematic temperature dependence of the electrical resistivity of magnetic RI compounds with negligible d-electron contribution. ....	23
<b>Figure I-6:</b>	Temperature dependence of the resistivity of a single-impurity Kondo system and a Kondo lattice. $\rho_i(0)$ is the zero temperature resistivity per ion in the dilute limit. ....	29
<b>Figure I-7:</b>	Temperature-dependence magnetic susceptibility $\chi(T)/\chi(0)$ of the Coqblin-Schrieffer model obtained by the Bethe-ansatz solution for different values of $j$ . ....	32
<b>Figure II-1:</b>	Arc-melting furnace chamber at the University of the Western Cape (Physics Department). ....	40
<b>Figure II-2:</b>	Schematic diagram of the arc-furnace melting chamber.....	41
<b>Figure II-3:</b>	Micracut 125 low speed cutter at the University of the Western Cape (Physics Department). ....	42
<b>Figure II-4:</b>	X – ray diffractometer (D8 Advance) at iThemba LABS, Cape Town. ....	43

<b>Figure II-5:</b> Schematic diagram of the dc – sample puck with three samples mounted for four wires resistance measurements. ....	44
<b>Figure II-6:</b> Cross-section of sample puck inside the Physical Property Measurement System (PPMS) sample chamber.....	44
<b>Figure II-7:</b> Overview of the Physical Property Measurement System (PPMS) at the University of Johannesburg Physics Department). ....	45
<b>Figure II-8:</b> The standard geometry of the sample for the resistivity measurements. ....	46
<b>Figure II-9:</b> Schematic view of sample and the Vibrating Sample Magnetometer (VSM) .....	47
<b>Figure II-10:</b> Magnetic Property Measurement System (MPMS), configured with optional Cryo-Cooled Dewar (EverCool™) at the University of Johannesburg (Physics Department). (a) Cabinet for EverCool compressor, (b) Computer and cabinet for gas handling and all control electronics, (c) Cabinet for Dewar, and (d) EverCooled head. ....	47
<b>Figure II-11:</b> Overview of the Cryogen Free Magnet system (CFM) at iThemba LABS, Cape Town. ....	48
<b>Figure IV-1:</b> X – ray diffraction pattern for the CePt <sub>2</sub> Si <sub>2</sub> and REPt <sub>2</sub> Si <sub>2</sub> (RE=Tb or Dy). The open circles are the experimental data. The solid lines through the data points are the results of the Rietveld refinement method and the bottom curves are the difference between the calculated and the experimental data. ....	56
<b>Figure IV-2:</b> The tetragonal crystal structure of REPt <sub>2</sub> Si <sub>2</sub> , (RE = Ce, Tb, Dy). The blue circles represents the RE atoms (Ce for the present picture). The pink and yellow circles represent Pt and Si atoms respectively occupying two different sites, 2c and 2b for Pt and 2c and 2a for Si. ....	57
<b>Figure IV-3:</b> The tetragonal lattice parameters (i) <i>a</i> and (ii) <i>c</i> and the unit cell volume (iii) <i>V</i> as a function of RE concentration <i>x</i> for the (Ce <sub>1-x</sub> RE <sub>x</sub> )Pt <sub>2</sub> Si <sub>2</sub> alloy systems with RE = Tb or Dy.....	58

- Figure IV-4:** The temperature dependence of the electrical resistivity,  $\rho(T)$  of the  $(\text{Ce}_{1-x}\text{Tb}_x)\text{Pt}_2\text{Si}_2$  alloy system. The red solid line through the data points in (a) and (b) are LSQ fits of the measured data to Eq. IV-6 and in (c) to Eq. IV-1.....61
- Figure IV-5:** The temperature dependence of the electrical resistivity,  $\rho(T)$  of the  $\text{DyPt}_2\text{Si}_2$  compound. The red solid line through the data points is the LSQ fits of the measured data to Eq. IV-2.....62
- Figure IV-6:** The temperature dependence of the electrical resistivity,  $\rho(T)$  of the  $(\text{Ce}_{1-x}\text{Dy}_x)\text{Pt}_2\text{Si}_2$  alloy system. The red solid line through the data points in (a) and (b) are LSQ fits of the measured data to Eq. IV-6. ....63
- Figure IV-7:** The temperature dependent resistivity,  $\rho(T)$ , of the non-magnetic counterpart  $\text{LaPt}_2\text{Si}_2$ . The inset illustrates the development of a superconducting transition.....66
- Figure IV-8:** The field variation of the magnetization at 1.7 K for  $(\text{Ce}_{1-x}\text{Tb}_x)\text{Pt}_2\text{Si}_2$  alloys measured with increasing and decreasing field. ....67
- Figure IV-9:** The field variation of the magnetization at 1.7 K for  $(\text{Ce}_{1-x}\text{Dy}_x)\text{Pt}_2\text{Si}_2$  alloys measured with increasing and decreasing field.....67
- Figure IV-10:** Temperature variation of the inverse susceptibility  $\chi^{-1}(T)$  for  $(\text{Ce}_{1-x}\text{Tb}_x)\text{Pt}_2\text{Si}_2$ . The data refer to a mole of rare-earth atoms. The solid lines through the data points represent LSQ fits of the measured data to a Curie-Weiss relationship (Eq. IV-9). ....70
- Figure IV-11:** Temperature variation of the inverse susceptibility  $\chi^{-1}(T)$  for  $(\text{Ce}_{1-x}\text{Dy}_x)\text{Pt}_2\text{Si}_2$ . The data refer to a mole of rare-earth atoms. The solid lines through the data points represent LSQ fits of the measured data to a Curie-Weiss relationship (Eq. IV-9). ....72
- Figure IV-12:** The low temperature ZFC and FC  $\chi(T)$  data for the  $(\text{Ce}_{1-x}\text{Tb}_x)\text{Pt}_2\text{Si}_2$  alloy system with  $x = 1, 0.8$  and  $0.6$ . The top inset display the low temperature FC  $\chi(T)$  data in a field of 0.1 T for compositions showing magnetic order and the bottom inset shows the variation of  $T_N$  as a function of Ce content. The

arrows at the top inset indicate the magnetic phase transition temperature. ....73

**Figure IV-13:** The low temperature variation of magnetic susceptibility  $\chi(T)$  for the  $(\text{Ce}_{1-x}\text{Dy}_x)\text{Pt}_2\text{Si}_2$  alloy system. .... 73

**Figure V-1:** X-ray diffraction pattern for the polycrystalline specimen  $\text{CeCu}_5\text{In}$  (i) and  $(\text{Ce}_{0.1}\text{Tb}_{0.9})\text{Cu}_5\text{In}$  (ii) showing a phase change. The top figure (i) shows the Rietveld refinement method. The open circles are the experimental data. The solid lines through the data points are the results of the Rietveld refinement and the bottom curves are the difference between the calculated and the experimental data. ....77

**Figure V-2:** The orthorhombic crystal structure of  $\text{CeCu}_5\text{In}$ . The blue circles represent the Ce atom. The brown circles represent Cu atoms occupying two different sites, 8d and 4c and the pink circles represent In atoms. ....78

**Figure V-3:** The orthorhombic lattice parameters  $a$  (i),  $b$  (ii) and  $c$  (iii) and the unit cell volume  $V$  (iv) as a function of Tb concentration  $x$  for the  $(\text{Ce}_{1-x}\text{Tb}_x)\text{Cu}_5\text{In}$  ( $0 \leq x \leq 0.4$ ) alloy system. ....79

**Figure V-4:** Electrical resistivity normalized to its room temperature value,  $\rho(T)/\rho_{300\text{K}}$ , versus temperature  $T$  for various value of  $x$  in the range  $0 \leq x \leq 0.4$  for the  $(\text{Ce}_{1-x}\text{Tb}_x)\text{Cu}_5\text{In}$  system. The red solid line through the data points of the  $\text{LaCu}_5\text{In}$  is the LSQ fits of the measured data to Eq. V-1. ....81

**Figure V-5:** The temperature dependence of the magnetic contribution to the total resistivity for the  $(\text{Ce}_{1-x}\text{Tb}_x)\text{Cu}_5\text{In}$  system shown on semi – log plots. The solid red lines through the data points are least – squares fits of the experimental data to Eq. V-2. ....83

**Figure V-6:** Plot of  $T_K$  against Tb concentration  $x$  for the  $(\text{Ce}_{1-x}\text{Tb}_x)\text{Cu}_5\text{In}$  alloy system. The solid represents the exponential decrease of  $T_K$  with increasing Tb concentration  $x$ . ....85

**Figure V-7:** The field variation of the magnetization  $\sigma(\mu_0H)$  measured at 1.7K for the alloy system  $(\text{Ce}_{1-x}\text{Tb}_x)\text{Cu}_5\text{In}$  with  $0 \leq x \leq 0.4$ . ....86



**Figure V-8:** Temperature variation of the inverse susceptibility  $\chi^{-1}(T)$  for  $(\text{Ce}_{1-x}\text{Tb}_x)\text{Cu}_5\text{In}$ . The data refer to a mole of rare-earth atoms. The solid lines through the data points represent LSQ fits of the measured data to a Curie-Weiss relationship (Eq.V-8).....87



## List of Tables

- Table IV-1:** Atomic coordinate and occupation factors for  $\text{REPt}_2\text{Si}_2$  (RE = Ce, Tb or Dy) obtained from the Rietveld refinement using the  $P4/nmm$  space group. The occupation factor of all the atoms was kept fixed. ....57
- Table IV-2:** The LSQ fits parameters of the temperature dependent resistivity for the  $\text{TbPt}_2\text{Si}_2$  and  $\text{DyPt}_2\text{Si}_2$  compounds. ....60
- Table IV-3:** The LSQ fits parameters of the temperature dependent resistivity  $\rho(T)$  for  $(\text{Ce}_{1-x}\text{Tb}_x)\text{Pt}_2\text{Si}_2$  as well as the observed and calculated(Eq. IV-7) values of the temperature minimum of  $\rho(T)$  and the observed values of the temperature maximum of  $\rho(T)$ .....62
- Table IV-4:** The LSQ fits parameters of the temperature dependent resistivity  $\rho(T)$  for  $(\text{Ce}_{1-x}\text{Dy}_x)\text{Pt}_2\text{Si}_2$  as well as the observed and calculated(Eq. IV-7) values of the temperature minimum of  $\rho(T)$  and the observed values of the temperature maximum of  $\rho(T)$ ..... 64
- Table IV-5:** Magnetic susceptibility data for the  $(\text{Ce}_{1-x}\text{Tb}_x)\text{Pt}_2\text{Si}_2$ . The effective magnetic moment  $\mu_{\text{eff}}$  as well as the paramagnetic Curie temperature  $\theta_p$  was obtained from LSQ fits of the experimental data in Fig. IV-10 to the Curie – Weiss relationship (Eq. IV-8). Values of  $T_N$  were inferred from the position of the maxima in the  $\chi(T)$  curves in the inset of Fig. IV-12. Values of  $\mu_{\text{eff}}$  Calculated for the alloys as described in the text are also included for comparison. ....71
- Table IV-6:** Magnetic susceptibility data for the  $(\text{Ce}_{1-x}\text{Dy}_x)\text{Pt}_2\text{Si}_2$ . The effective magnetic moment  $\mu_{\text{eff}}$  as well as the paramagnetic Curie temperature  $\theta_p$  was obtained from LSQ fits of the experimental data in Fig. IV-11 to the Curie – Weiss relationship (Eq. IV-8). Value of  $\mu_{\text{eff}}$  Calculated for the alloys as described in the text are also included for comparison. ....71
- Table V-1:** Atomic coordinate and occupation factors for  $\text{CeCu}_5\text{In}$  obtained from the Rietveld refinement method using the  $Pnma$  space group. The occupation factor of all the atoms was kept fixed. ....78

- Table V-2:** The LSQ fits parameters values of the magnetic contribution to the total resistivity for the  $(\text{Ce}_{1-x}\text{Tb}_x)\text{Cu}_2\text{In}$  alloys system using Eq. V-3 and the observed values of  $\rho_{0\text{TK}}$  at the lowest measured temperature as well as the calculated values of  $T_K$  using Eq. V-5.. .....84
- Table V-3:** Magnetic susceptibility data for the  $(\text{Ce}_{1-x}\text{Tb}_x)\text{Cu}_5\text{In}$ . The effective magnetic moment  $\mu_{\text{eff}}$  as well as the paramagnetic Curie temperature  $\theta_P$  was obtained from LSQ fits of the experimental data in Fig. V-8 to the Curie – Weiss relationship (Eq. V-7). Values of  $\mu_{\text{eff}}$  calculated for the alloys as described in the text are also included for comparison. ....88



# Chapter I:

---

## Theoretical background

### I-1: Introduction

In the past the name “rare” for the fifteen elements from lanthanum (La, atomic number: 57) to Lutetium (Lu, atomic number: 71) was understood to mean of their not too high natural abundance and their commercial scarcity in sufficiently pure conditions [1]. Several research studies undertaken on material systems with rare earth (RE) elements, deal with intermetallic compounds and alloys. Technical application of the materials involves intermetallic compounds in which RE elements are combined with 3d transition elements.

The present chapter will be restricted to an overview of the properties of the rare earth elements and the rare earth intermetallic compounds. This will be followed by an overview of the Heavy-Fermions (HF) and Kondo systems. Finally, a theoretical background on transport and magnetic properties of these materials will be considered.

### I-2: Rare earth elements and rare earth intermetallic compounds

The rare earth (RE) elements also known as the lanthanide elements are a set of fifteen chemical elements in the periodic table starting from La to Lu, plus Scandium (Sc, atomic number: 21) and Yttrium (Y, atomic number: 39). Sc and Y are considered RE elements since they tend to occur in the same ore deposits as the lanthanides and exhibit similar chemical properties [1, 2, 3].

The electronic configuration of the RE elements, with minor exception, are that of the Xenon element plus the 4f, 5d and 6s orbitals and can be written in the form:

$$[\text{Xe}] 4f^n 5d^1 6s^2, \quad n = 0 - 14.$$

A well known property of the RE elements is their incomplete 4f orbital, which becomes progressively more filled on going from La ( $n = 0$ ) to Lu ( $n = 14$ ). The unpaired electrons accommodated in this shell largely determine the physical properties of the RE elements and compounds. The  $5d^1$  and  $6s^2$  valence electrons form the conduction band in the solid and predominantly determined their chemical properties. The 4f orbitals are buried deep inside the atom and are well shielded from the atom's environment by the 4d and 5p electrons. As a

consequence of this, the chemical properties of the RE are almost the same and are largely determined by their ionic size, which decrease gradually from  $\text{La}^{3+}$  to  $\text{Lu}^{3+}$ , the so called lanthanide contraction [4] (Fig. I-1).

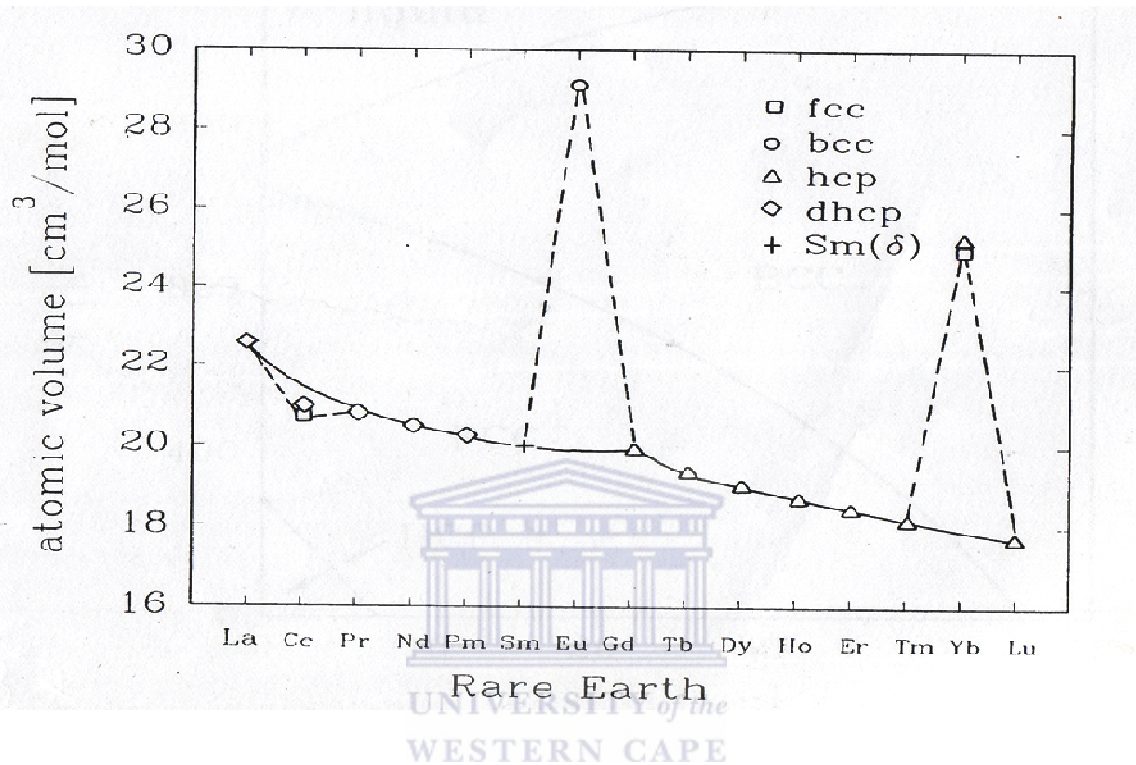


**Figure I-1:** Atomic volume of the RE elements and their crystal structure at room temperature [3].

As a rule, all the RE give rise to the same type of compounds when combined with other metals. Ce, Eu and Yb are well-known exception to this rule. All RE elements are present in the trivalent state in metal systems. However the three elements Ce, Eu and Yb frequently adopt a different valence.  $\text{Ce}^{3+}$  very often tends to be tetravalent  $\text{Ce}^{4+}$  by losing its single 4f electrons. On the other hand  $\text{Eu}^{3+}$  can gain an electron to be in the divalent state  $\text{Eu}^{2+}$  with the  $4f^7$  configuration which has the extra stability of a half-filled shell. This is similar for  $\text{Yb}^{3+}$  which can gain an electron to form  $\text{Yb}^{2+}$  [5, 6].

Pure RE elements generally crystallize in a hexagonal close packed (hcp) structure (Fig. I-1), except for Ce, Eu and Yb, which have a cubic structure and Sm a rhombohedral structure at room temperature and normal pressure. From the temperature –pressure phase diagram of Ce

[7], this element shows fine solid phases: two face-centred cubic (fcc) phases  $\alpha$  and  $\gamma$ ; one hcp phase  $\beta$ ; one high-temperature body-centred cubic (bcc) phase  $\delta$ ; one orthorhombic high-pressure phase  $\alpha$ .

All the trivalent RE-ions, except Lu, have unpaired 4f electrons. These 4f electrons are responsible for their magnetic behaviour in the solid state both as pure metals and as metallic alloys. La and Y with no 4f-electron and Lu with a full 14 f-electron have no magnetic moments. The magnetic moments of the RE-ions deviate largely from spin only values due to the spin-orbit coupling and are given by:

$$\vec{\mu} = -g_J \mu_B \vec{J}, \quad \text{I-1}$$

where  $\vec{J}$  represents the total angular momentum,  $\mu_B = \frac{e\hbar}{2m}$  is the Bohr magneton and  $g_J$  the spectroscopic splitting factor also known as the Landé  $g$ -factor given by:

$$g_J = 1 + \frac{J(J+1) + S(S+1) - L(L+1)}{2J(J+1)}. \quad \text{I-2}$$

$S$  is the spin angular momentum and  $L$  is the orbital angular momentum. The combination of the spin and orbital angular momentum is known as the Russell-Saunders coupling, given the total angular momentum in the form:

$$\vec{J} = \vec{L} + \vec{S}. \quad \text{I-3}$$

For incompletely filled shells, we have  $J = L - S$  for a shell less than half occupied and  $J = L + S$  for a shell more than half occupied. The spin, orbital and total angular momentum of a pure RE-ions are determined by Hund's rule and the effective moment ( $\mu_{\text{eff}}$ ) is given by:

$$\mu_{\text{eff}} = g_J \sqrt{J(J+1)} \mu_B. \quad \text{I-4}$$

The maximum of unpaired 4f-electrons is 7 in  $\text{Gd}^{3+}$ -ion with effective magnetic moment of  $7.94 \mu_B$ , but the largest magnetic moment of 10.4 and  $10.7 \mu_B$  are exhibited by  $\text{Dy}^{3+}$  and  $\text{Ho}^{3+}$  respectively.  $\mu_{\text{eff}}$  and the quantity  $g_J J$  determine the magnetic behaviour in the paramagnetic and magnetically ordered regions respectively [1]. The effect of crystal electric field (CEF) of the RE-ions is rather small and is less important compared to the spin-orbit coupling with regard to energy levels [8]. In practice, there is a good agreement between experimental

values of  $\mu_{\text{eff}}$  with the calculated values using the lowest occupied multiplet  $J$ . The exception occurs for compound containing Sm and Eu-ions due to the fact that the first higher energy level of the multiplet  $J$  is near to the ground state and consequently the first excited state is already appreciably thermally populated at room temperature. In the case of RE compounds and alloys, a reduction of the effective magnetic moment for the expectations of the ionic model often occurs due to the CEF effect. Magnetic RE elements, exhibit a variety of magnetic behaviour in solid state both as pure metals and metallic alloys. For instance, Gd is ferromagnetic with a Curie temperature  $T_C = 293$  K, whereas Eu is an antiferromagnetism (AF) with a Néel temperature  $T_N = 90$  K [9]. The other pure RE elements show a variety of magnetic behaviour such as ferromagnetism at low temperatures followed by AF at higher temperatures and canted magnetic structures. The varieties of magnetic behaviour of RE elements are completely different, when these elements form intermediate compounds.

RE elements form Intermetallic compounds with non-transition metals or 3d-transition metals and exhibit a variety of crystalline structures [1, 10]. In the past few decades, RE Intermetallic compounds have been the subject of many experimental investigations because of the nature and variety of their physical properties [1, 10]. The 4f wave function of the RE element are highly localized due to their small radial extension. As a result of this, direct interaction between the 4f moments of the RE elements cannot take place in the solid state. However the interaction between 4f moments can be indirectly via a spatially uniform polarization of the conduction electrons called the Rudermann, Kittel, Kasuya, Yosida (RKKY) interaction. This interaction takes an account of the linear response in the exchange interaction between local moments and the conduction electrons. The mechanism involves in this interaction process is that, the conduction electron gas is magnetized in the vicinity of the magnetic ion. This magnetization causes an indirect exchange interaction between two magnetic ions, as a result of a second ion perceives the magnetization induced by the first ion [10]. The direct magnetic ion- conduction electron interaction is known as Kondo effect. This interaction may be written in the form as suggested by de Gennes:

$$H = -\Gamma(g_J - 1)\vec{s} \cdot \vec{J}, \quad \text{I-5}$$

where  $\Gamma$  is the exchange coupling constant between the conduction electron spin  $\vec{s}$  and the localized 4f electron total angular momentum  $\vec{J}$ . The RKKY interaction couples the total angular momentum vectors  $\vec{J}_i$  and  $\vec{J}_j$  of nearby RE-ions. The localized 4f moment will

orientate its spin according to the spin of the conduction electron polarization and this determines the ultimate type of magnetic ordering e.g. helical and sinusoidal ordered structures of the heavy RE elements (Gd – Lu). As a consequence of magnetic interaction, the Curie law relation:

$$\chi(T) = \frac{g_J^2 \mu_B^2 J(J+1) N_A}{3k_B T}, \quad \text{I-6}$$

for the magnetic susceptibility of a non-interacting system of magnetic dipoles is in general changed to the Curie – Weiss relation:

$$\chi(T) = \frac{g_J^2 \mu_B^2 J(J+1) N_A}{3k_B T(T - \theta_p)}, \quad \text{I-7}$$

where  $\theta_p$  is the paramagnetic Curie temperature given in the RKKY model by [1]:

$$\theta_p = -\frac{3\pi n^2 |\Gamma|^2}{k_B E_F} (g_J - 1)^2 J(J+1) \sum_i F(2k_F R_i), \quad \text{I-8}$$

where  $n$  is the average conduction electron density,  $E_F$  is the Fermi energy,  $k_F$  is the Fermi wave number,  $k_B$  is the Boltzmann constant and  $F$  is a function of the position of the local moment  $R_i$ . The summation is over all local moment distances with origin at the local moment site itself.

### **I-3: Overview of heavy-fermions and Kondo systems.**

The discovery of Kondo effect began in the 1930s with the study of magnetic impurities in non-magnetic metals, where a resistivity ( $\rho(T)$ ) minimum was found for normal metals at a temperature  $T = T_{\min}$ . The appearance of the resistivity minimum at  $T_{\min}$  where normal  $\rho(T) \sim T^5$  metallic behaviour was expected, was proved to be caused by magnetic impurities diluted in the metal. The resistivity increase below  $T_{\min}$  is described by  $\rho(T) \sim -\ln T$  [12]. The first theoretical model explaining the logarithmic increase in  $\rho(T)$  in dilute magnetic alloys was put forward in 1964 by Kondo [8, 11].

The expression “heavy-fermions” comes into use for those compounds, where localized magnetic moments formed by RE or actinides ions transform the metal in which they are immersed, generating quasi-particles with masses in excess of 1000 bare electron mass [14].



In many respects, heavy-Fermions compounds are equivalent to Kondo lattice compounds. The physical properties of these two systems may be understood, when taking into account a characteristic temperature  $T^*$ , which can be very close to the Kondo temperature  $T_K$  for a corresponding dilute Kondo system. The similarities in these two systems can be seen for instance in the temperature dependent resistivity. At higher temperatures, well above  $T^*$  or  $T_K$  both system exhibit  $\rho(T) \sim -\ln T$ . However at temperatures below  $T^*$ , marked deviations occur for both systems. At low temperatures, Kondo lattices and heavy-fermions are characterized by a steep drop in  $\rho(T)$ . A signature of HF compounds is the low temperature electronic contribution to the total specific heat:

$$C_{el}(T) = \gamma T, \quad \text{I-9}$$

where  $\gamma$  the electronic coefficient is given by:

$$\gamma = \frac{2}{3} \pi^2 k_B^2 N(E_F). \quad \text{I-10}$$

$N(E_F)$  is the density of states at the Fermi level, related to the electron effective mass  $m^*$  as follows:

$$N(E_F) = \frac{m^* k_F}{2\pi^2 \hbar^3}, \quad \text{I-11}$$

Where  $\hbar$  is the Plank's constant. The enhanced  $\gamma$  value give an extremely large value of the electron effective mass of  $10^2$  to  $10^3$  times greater than that of a free electron mass. Typical HF compounds are  $\text{CeAl}_3$  and  $\text{CeCu}_6$  with  $\gamma = 1600 \text{ mJ/mole.K}^2$  [14] and  $1670 \text{ mJ/mole.K}^2$  [15] respectively compared to that of a normal metal, such as copper with  $\gamma = 0.7 \text{ mJ/mole.K}^2$  [16]. Another characteristic feature of the HF materials is an enhanced Pauli susceptibility which has a form for non-interacting band electrons [17]:

$$\chi(0) = 2N(E_F)\mu_B^2. \quad \text{I-12}$$

The value of  $\chi(0)$  for a typical HF compound such as  $\text{CeAl}_3$  amounts to  $4.52 \times 10^{-7} \text{ m}^3/\text{mole}$  [18], which is roughly  $10^3$  times that of an ordinary metal like Cu with a value of  $12.6 \times 10^{-11} \text{ m}^3/\text{mole}$  [16].

The physics around the HF and Kondo lattice systems are predominantly determined by two main interactions, these are:

- The RKKY interaction, characterized by the intersite interaction temperature,  $T_{RKKY}$ , leads to a magnetically ordering ground state.
- The Kondo effect, characterized by the Kondo temperature  $T_K$ , leads to the effective suppression of the  $Ce^{3+}$ -ion moments.

Both characteristic temperatures depend on the magnetic exchange integral,  $\mathfrak{S}_{sf}$ , between the  $Ce^{3+}$ - $4f$  local moments and the conduction electrons and the density of state at the Fermi level  $N(E_F)$ , such that:

$$T_{RKKY} \sim \mathfrak{S}_{sf}^2 N(E_F), \quad \text{I-13}$$

$$T_K \sim \exp\left[-\frac{1}{|\mathfrak{S}_{sf} N(E_F)|}\right]. \quad \text{I-14}$$

The magnetic exchange integral is defined according to Schrieffer-Wolff [19] transformation in the form:

$$\mathfrak{S}_{sf} = \frac{|V_{sf}|^2}{E_F - E_{4f}}, \quad \text{I-15}$$


where  $E_F$  and  $E_{4f}$  are the energy at the Fermi level and the  $4f$  levels respectively.  $V_{sf}$  is the hybridization matrix element which determines the degree of mixing of the localized  $4f$  electrons and the conduction bands. Depending on the strength of  $\mathfrak{S}_{sf}$ , a competition between RKKY interaction and Kondo effect is observed leading to different ground state varying from HF, AF to intermediate valence states [20].

### I-3-1: Competition between RKKY interaction and Kondo effect.

As mentioned earlier, the RKKY interaction and Kondo effect, both depend on the strength of  $\mathfrak{S}_{sf}$ . In most cases RE intermetallic compounds, the  $4f$  levels are below the Fermi level, as a result of this  $(E_F - E_{4f})$  becomes very large and the Kondo coupling constant  $\mathfrak{S}_{sf}$  is small. From the exponential and quadratic dependence of  $T_K$  and  $T_{RKKY}$  respectively with respect to  $\mathfrak{S}_{sf}$  (Eqs. I-13 and I-14), it is evident that  $T_K$  becomes negligible with respect to  $T_{RKKY}$  ( $T_{RKKY} \gg T_K$ ). As a result of this a magnetic phase transition occurring at  $T_M \approx \mu_{eff}^2 T_{RKKY} \gg T_K$  [21] and the localized magnetic moment does not contribute in the Kondo spin-flip scattering process. In the case of anomalous RE intermetallic compounds, the

anomalous proximity of the  $4f$  and the Fermi levels results in a strong  $\mathfrak{S}_{sf}$  enhancement (Eq.I-15), and owing to the different dependence of  $T_K$  and  $T_{RKKY}$  (Eqs. I-13 and I-14) with respect to  $\mathfrak{S}_{sf}$ , we may have non-magnetic concentrated Kondo systems (CKS) or intermetallic valence (IV) RE intermetallic compounds in the case  $T_K \gg T_{RKKY}$ , or a magnetic CKS in the case  $T_K > T_{RKKY}$ . Studies of this particular feature of Kondo lattice were initiated by Doniach (Fig. I-2) [17]. Fig. I-2 shows a schematic of the classification of the CKS based on the relation between  $T_K$  and  $T_{RKKY}$  as a function of  $\Gamma/D$  which is related to  $|\mathfrak{S}_{sf}N(E_F)|$  with  $D$  being the width of the  $s-d$  band, as well as the magnetic phase transition temperature  $T_M$ . This figure illustrates the classical qualitative description of the competition between RKKY interaction and the Kondo effect. For systems exhibiting a non-magnetic ground state such as  $CeAl_3$  [18] or  $CeCu_2Si_2$  [22], physical properties such as specific heat, susceptibility and resistivity have been interpreted as verifying such a non-magnetic ground state in which the  $4f$  level was put exactly at  $E = E_F$ . On the other hand “high energy spectroscopic data” for the compounds unambiguously show that the  $4f$  level lies much deeper ( $E_F - E_{4f} \sim (1-2) \text{ eV}$ ) and the Ce valence in  $CeAl_3$  and  $CeCu_2Si_2$  is almost trivalent [12].

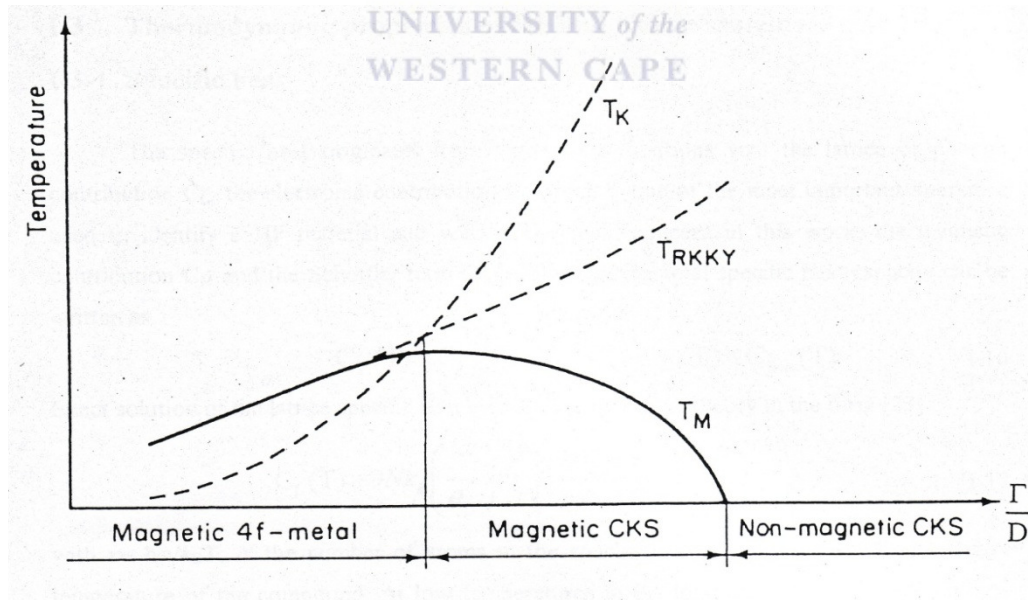


**Figure I-2:** The classification of CKS by the relation between two characteristic temperatures  $T_K$  and  $T_{RKKY}$ ,  $T_M$  is the magnetic transition temperature [20].

Experimentally, the variation of the product  $|\mathfrak{S}_{sf}N(E_F)|$ , changes the relative strength of Kondo and RKKY interaction which are in competition. This can be achieved by applying

chemical substitution e.g.  $\text{CePt}_2(\text{Si}_{1-x}\text{Ge}_x)_2$  [23] or hydrostatic pressure e.g.  $\text{CeAg}$  [24] since  $|\mathfrak{S}_{sf}N(E_F)|$  depends on the unit cell volume [25, 26]. The former method which is experimentally easier to achieve, will be used in this research project.

### I-3-2 Kondo effect

Kondo effect is an unconventional phenomenon, which results from magnetic impurity ion “screened” by the spins of the Fermi – sea at low temperatures [27]. As the impurity ion is screened, a portion of conduction electrons are bonded to it leading to a minimum in temperature dependence of the electrical resistivity curves ( $\rho(T)$ ) of dilute magnetic alloys at low temperatures. This is followed by logarithmic increase with decreasing temperature. The appearance of the resistivity minimum at temperatures where normal  $\rho(T) \sim T^5$  metallic behaviour was expected, results from the interplay between the monotonically decreasing phonon contribution and the logarithmic increasing magnetic contribution with lowering in temperature caused by magnetic impurities diluted in the metal. Kondo showed that the anomaly high scattering probability of magnetic ions at low temperatures is a consequence of the dynamic nature of the scattering by the exchange coupling  $J_{sf}$  and the sharpness of the Fermi surface at low temperatures [16].

Two scattering processes are characteristic of Kondo effect. These are, the incoherent single-ion Kondo scattering and the coherent Kondo lattice scattering. The evolution from coherent Kondo lattice scattering to incoherent single-ion Kondo scattering has been observed in many resistivity studies of Kondo alloy systems. This evolution can be achieved experimentally by continuously substituting the magnetic RE element (Ce, Eu, Sm, Yb) in CKS with a non-magnetic element (La, Y, Lu), e.g.:  $(\text{Ce}_{1-x}\text{La}_x)\text{Cu}_5\text{In}$  (Fig. I-3) [28],  $(\text{Ce}_{1-x}\text{La}_x)\text{Cu}_6$  [29] or with heavy RE elements (Gd to Tm), e.g.:  $(\text{Ce}_{1-x}\text{Gd}_x)\text{Pt}_2\text{Si}_2$  [30], or a substitution of the ligand, for instance in  $\text{CePt}_2(\text{Si}_{1-x}\text{Ge}_x)_2$  [23].

The incoherent single – ion Kondo scattering observed at high temperatures ( $T > T_K$ ) is characterized by a minus logarithmic ( $-\ln T$ ) increase in  $\rho(T)$  with decreasing temperature, culminating in saturation as the temperature tends to zero. The model used by Kondo to explain the  $-\ln T$  increase in  $\rho(T)$  with decrease in temperature is divergent and could not be applied to find  $\rho(T)$  dependence at  $T \rightarrow T_K$ . This divergence is due to the formation of the narrow ( $\sim k_B T_K$ ) many-body resonance near  $E_F$  at low temperatures  $T \leq T_K$ , and it connected to the crossover from perturbative conduction-electron interaction with localized magnetic

moments ( $T \gg T_K$ ) to the strong hybridization and the formation of the quasi-bound state ( $T \ll T_K$ ) [11]. At temperatures well below  $T_K$ , a Kondo system can be studied within the framework of the Fermi Liquid model [31]. The failure of the Kondo model is connected with the absence of a single parameter for the whole wide temperature range which is the crossover from local moment behaviour, where the spin is free at high temperature ( $T \gg T_K$ ) and the low temperature limit ( $T \ll T_K$ ), where the spin becomes highly correlated with the surrounding electrons.

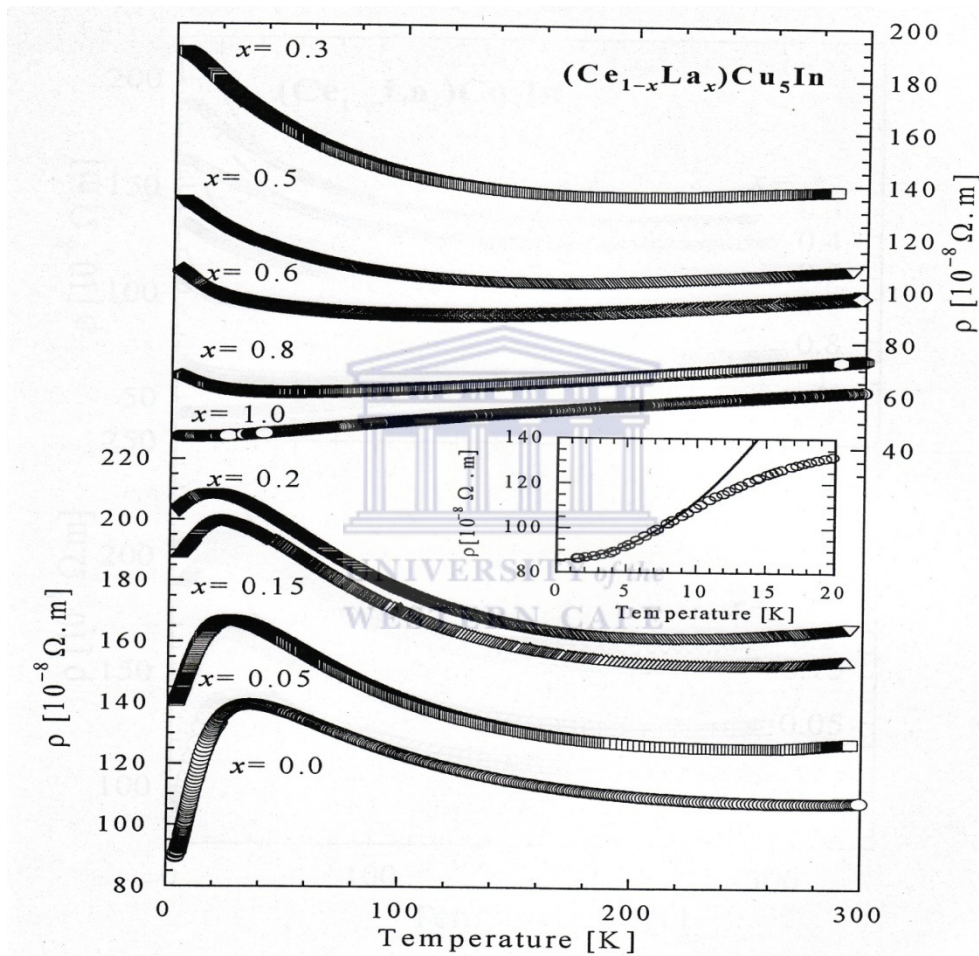


**Figure I-3:** The temperature variation of electrical resistivity in the range  $4 \leq T \leq 295\text{K}$  for compounds in the pseudo-ternary alloy system  $(\text{Ce}_{1-x}\text{La}_x)\text{Cu}_5\text{In}$  ( $0 \leq x \leq 1$ ). The inset shows the Fermi-liquid behaviour of the parent compound  $\text{CeCu}_5\text{In}$ , where the line represent the LSQ fit of the measured data to  $\rho(T) - \rho_0 = AT^2$  [28].

To overcome the Kondo problems, several theoretical models were put forward to solve the magnetic single – impurity problems, such as the Anderson model [32], the Coqblin Schrieffer model [33], using different methods. Successful methods have been suggested for



the whole temperature range from  $T \gg T_K$  to  $T \ll T_K$ , such as Wilson's numerical renormalization group [34] and Nozières Fermi-liquid theory [31]. Physical properties such as magnetic susceptibility  $\chi(T)$ , specific heat  $C_p(T)$  and electrical resistivity  $\rho(T)$  have been calculated for the whole temperature range [35, 36, 37, 38].

The coherent Kondo lattice scattering observed at low temperatures ( $T < T_K$ ) is characterized by a resistivity maximum at temperature  $T_{\max}$ , followed by a drop towards the lowest temperatures. In the low temperature region, the  $4f$  magnetic ions form a regular sublattice in the Kondo systems. The drop observed in  $\rho(T)$  as  $T$  tends to zero, results from the scattering of the conduction electrons as coherence develops between the Kondo centres. The resistivity curve well below  $T_{\max}$  at a characteristic temperature called the coherent temperature  $T_{\text{coh}}$  ( $T_{\text{coh}} \ll T_{\max}$ ) follows a  $T^2$  power-law behaviour characteristic of Fermi-liquid behaviour. This resistivity behaviour will be discussed in more detail in section I-3. The theoretical treatments of the Kondo lattice in the local moment regime have been done using different approaches [35], such as: the decoupling approximation [40, 41, 42], perturbative method [43], a variational method [44], the functional integral method [45, 46, 47] and the slave boson by Coleman [48]. The perturbative method suggested by Grewe, shows that for temperatures well below  $T_K$  and owing to the lattice correlations, the Kondo resonance is split and a pseudo – gap is formed near the Fermi level  $E_F$ . The decoupling approximation suggested by Kaga and Kubo shows two ways of describing the Kondo lattice state. These are:

- The “single – site treatment” [49], where the  $f$  electrons self-energy is treated on each site as independent local effect and coherence between site sets in more phonologically below  $T_K$ .
- The “coherent – lattice” treatment [41], where coherence as a consequence of correlation between sites sets in well above  $T_K$ .

#### **I-4: Electrical resistivity and magnetic properties of heavy-Fermions and Kondo systems**

The transport and thermodynamic properties of heavy-Fermions and Kondo systems include electrical and thermal transport such as electrical resistivity, magnetoresistivity, Hall Effect,

thermoelectric power, thermal conductivity and the thermodynamic properties such as magnetic susceptibility, magnetization and specific heat. This section will only discuss the standard theoretical results of selected physical properties investigated in this research project such as electrical resistivity, magnetic susceptibility and magnetization. A brief theoretical result on specific heat will be discussed at the end of this section.

#### **I-4-1 Electrical resistivity**

The electrical transport properties of solids are governed by the flow of electrons. The first attempt to explain electrical conduction in solids was provided by Drude in 1900 [51], who accepted the notion of metals as a set of ions permeated by a “sea” of electrons or an “electron gas” [52]. The free electrons, which are called valence electrons in a free atom, are the conduction electrons in solid. Consequently, knowledge on the density of conduction electrons, the energy associated with the conduction electrons and the paths followed in their motions in a given material are of great importance for the study of electronic conduction in materials [34, 50].

In the free – electron model, the conduction electrons are assumed to be completely free except for a potential at the surface, which has the effect of confining the electrons to the interior of the specimen and consequently do not contribute a scattering potential. However, conduction in metals is due to other scattering processes of the free electrons along the paths they follow in their motions in the interior of the specimen. These scattering processes can be due to:

- All static imperfections, such as the presence of foreign impurities either intentional, accidental and crystal defects such as grain boundaries, dislocations and stacking faults. The resistivity and thermal conductivity associated to this scattering process are dominant at low temperature.
- The lattice vibrations (phonons) of ions around their equilibrium positions due to thermal excitation of ions. The intensity associated to this scattering process increase extremely as the temperature increases.
- The localized magnetic moments of the  $4f$  RE atom in the dilute or concentrate Kondo, HF, spin fluctuation and IV systems.
- The conduction electrons themselves. The electron-electron collision is very small for a typical metal. At room temperature (300 K), the contribution due to electron-phonon

scattering is likely to be dominant in comparison to electron-electron contribution. At liquid helium temperature (4.2 K) a contribution proportional to  $T^2$  has been found in a resistivity of a number of metals, consistent with the form of the electron-electron scattering [16].

All the scattering processes mentioned above, except for the electron-electron scattering, can be described in terms of a unique parameter: the relaxation time. Therefore the transport properties such as electrical resistivity  $\rho(T)$ , thermoelectric power  $S(T)$  and thermal conductivity  $\lambda(T)$  can be described using the linearized Boltzmann's equation. This leads to the general formulation [34, 50]:

$$\rho(T) = \frac{1}{e^2 K_0}; \quad S(T) = -\frac{K_1}{|e|K_0}; \quad \lambda(T) = \frac{1}{T} \left( K_2 - \frac{K_1^2}{K_0} \right). \quad \text{I-16}$$

Expressions of  $K_n$  are defined by the following integral:

$$K_n = \frac{k_F^3}{3\hbar^2 m} \int \epsilon_k^n \tau(\epsilon_k) \left( -\frac{\partial f_k}{\partial \epsilon} \right) d\epsilon_k, \quad \text{I-17}$$

where  $f_k$  is the Fermi-Dirac distribution function,  $\epsilon_k$  is the energy of the free electron in a quantum state  $k$ , and  $\tau(\epsilon_k)$  is the relaxation time. Once  $\tau(\epsilon_k)$  is determined, the different transport coefficients can be calculated. The probabilities of electrons being scattered by impurities, phonon and localized magnetic moments, neglecting the scattering from electrons are additive, since these three mechanisms are assumed to act independently. It follows from Matthiessen's rule, the total resistivity is given in the form:

$$\rho(T) = \rho_0 + \rho_{ph}(T) + \rho_{4f}(T), \quad \text{I-18}$$

where  $\rho_0$  represents the scattering of conduction electrons from the defects and impurities,  $\rho_{ph}(T)$  and  $\rho_{4f}(T)$  represent the scattering of conduction electrons due to phonons and the 4f-magnetic impurities respectively. Experimentally, the resistivity at a given set of conditions such as temperature ( $T$ ), pressure ( $P$ ) and magnetic field ( $B$ ), measures the three combined scattering processes in which the conduction electrons are involved. Fig.I-4 shows the simple geometry for the resistivity measurement.



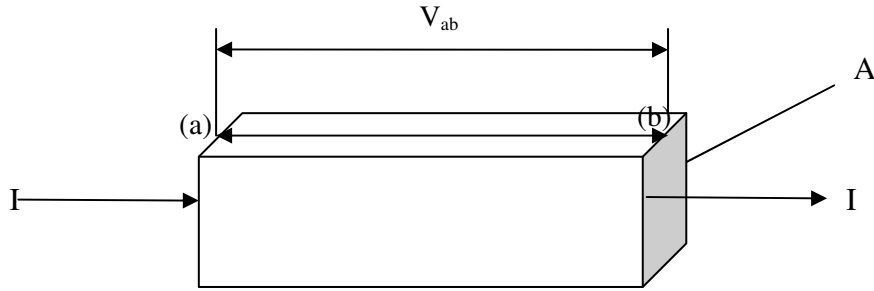


**Figure I-4:** The simple geometry for the resistivity measurements.

An elementary charge  $dQ$  passes in a time  $dt$  through a cross-sectional area  $A$  of a bar sample of length  $L$ . The measurement of the voltage difference  $V_{ab} = V_a - V_b$  across the ends (a) and (b) of the sample gives the resistivity through the relations:

$$\rho = \frac{V A}{I L} \quad \text{with} \quad I = \frac{dQ}{dt} . \quad \text{I-19}$$

For a uniform current density throughout the length  $L$  of the sample one can obtain comprehensive values of  $\rho$ , and this can be achieved only if  $\frac{A}{L} \ll 1$ .

Considering the total resistivity given by Eq. I-18,  $\rho_0$  is the temperature-independent contribution which originates from the scattering of electrons from imperfections in the crystal and defects. This constant value of  $\rho_0$  gives an indication of the perfection of the crystal. In current practice, to specify the overall purity and perfection of a normal metal

crystal, we quote the residual resistivity ratio:  $RRR = \frac{\rho_{(300K)}}{\rho_{(4.2K)}}$ . Improvement of this ratio can

be achieved by annealing the sample at a sufficiently high temperature for a period of time.

$\rho_{ph}(T)$  represent the temperature-dependent phonon contribution originating from the scattering of electrons from the thermal vibration of ions around their equilibrium position.

This contribution is given by the Bloch-Grüneisen Law [53]:

$$\rho_{ph}(T) = \frac{4\kappa}{\theta_R} \left( \frac{T}{\theta_R} \right)^5 \int_0^{\theta_R/T} \frac{x^5 dx}{(e^x - 1)(1 - e^{-x})} , \quad \text{I-20}$$

where  $\kappa$  is the electron-phonon coupling constant.  $\theta_R$  is the characteristic temperature for the phonon resistivity which differ slightly from the Debye temperature  $\theta_D$  obtained from specific heat (see section I-3-3). At high temperature  $\left(T \geq \frac{\theta_R}{2}\right)$ , the integral in Eq. I-20 gives an expression proportional to  $\left(\frac{\theta_R}{T}\right)^4$ , and leading to  $\rho_{ph}(T) \sim T$ . At low temperatures  $T \leq \frac{\theta_R}{10}$ , this integral gives a constant value of 124.4 [2] and  $\rho_{ph}(T) \sim T^5$ . Experimentally the phonon contribution to the total resistivity of RE intermetallic compounds is obtained from the total resistivity of the non-magnetic La or Y or Lu counterpart.

The magnetic contribution  $\rho_{4f}(T)$  of interest in this research project, originates from the scattering of conduction electrons from the localized  $4f$  RE-ions. In the following subsection, we will primarily focus on the magnetic contribution  $\rho_{4f}(T)$  of RE systems exhibiting long-range magnetic order and followed with  $\rho_{4f}(T)$  of the HF and Kondo systems.

#### **I-4-1-a: Magnetic resistivity of RE intermetallic compounds**

The magnetic contribution  $\rho_{4f}(T)$  to the total resistivity of RE-intermetallic compounds describes scattering processes of the conduction electrons due to disorder in the arrangement of the magnetic moments. A schematic temperature dependence of the electrical resistivity of magnetic RE intermetallic compounds with negligible  $d$ -electron contribution is shown in Fig. I-5.  $T_{ord}$  represents the magnetic phase transition temperature which separates the high temperature paramagnetic region (disorder) to the ordering region at low temperature.  $\rho_T$  and  $\rho_{spd}$  are the total and the spin disorder resistivity.  $\rho_{mag} \equiv \rho_{4f}$  shown in Fig.I-5 is described by the following features:

- A temperature-independent behaviour, known as a spin disorder resistivity  $\rho_{spd}$  for  $T > T_{ord}$ .

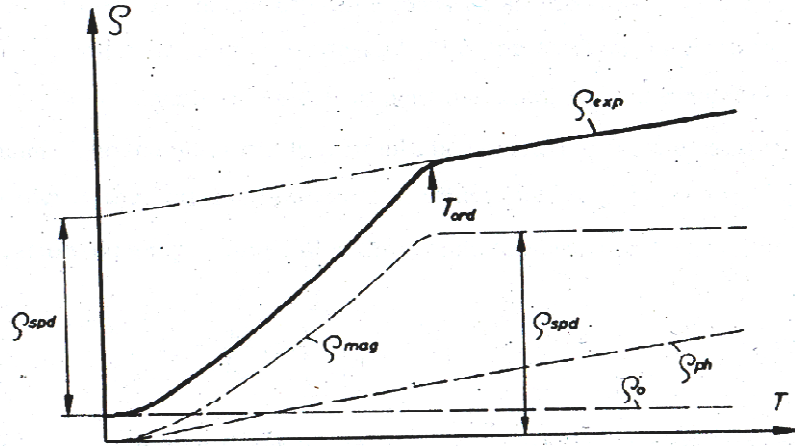


**Figure I-5:** Schematic temperature dependence of the electrical resistivity of magnetic RE compounds with negligible  $d$ -electron contribution [2].

- A pronounced kink at  $T = T_{ord}$ .
- A strong decrease for  $T < T_{ord}$  with decrease temperature.

In the paramagnetic region, several authors were able to obtain an expression of the magnitude of  $\rho_{spd}$  by solving the Boltzmann equation in the relaxation time approximation [54, 55, 56]:

$$\rho_{spd} = \frac{3\pi N m^*}{2\hbar e^2 \varepsilon_F} |\mathfrak{S}_{sf}|^2 (g_J - 1)^2 J(J+1), \quad \text{I-21}$$

where  $m^*$  is the effective mass of the electron,  $\varepsilon_F$  is the Fermi energy,  $N$  is the number of atoms per unit volume and  $e$  is the electron charge.  $\rho_{spd}$  is proportional to the de Gennes factor  $(g_J - 1)^2 J(J+1)$  and contribute largely to the total resistivity. The linear increase above  $T_{ord}$  in the total resistivity curve originates from electron-phonon scattering. For a system consisting of two different RE elements A and B for instance ( $A_x B_{1-x}$ ),  $\rho_{spd}$  is given in the form:

$$\rho_{spd} = \frac{3\pi N m^*}{2\hbar e^2 \epsilon_F} \left[ \begin{array}{l} x |\mathfrak{S}_{sfA}|^2 (g_{JA} - 1)^2 J_A (J_A + 1) + (1-x) |\mathfrak{S}_{sfB}|^2 (g_{JB} - 1)^2 J_B (J_B + 1) \\ - x(1-x) [\mathfrak{S}_{sfA} (g_{JA} - 1) J_A - \mathfrak{S}_{sfB} (g_{JB} - 1) J_B] \end{array} \right], \quad \text{I-22}$$

where  $\mathfrak{S}_{sfA}$  and  $\mathfrak{S}_{sfB}$  are the direct exchange integrals of the alloy components and  $g_{JA}$  and  $g_{JB}$  are the respective Landé g-factors of RE A and B respectively. For a system containing only one magnetic RE element and a non-magnetic RE element such as La, Y, or Lu as in (Tb<sub>x</sub>La<sub>1-x</sub>) Eq. I-22 is reduced to:

$$\rho_{spd} = \frac{3\pi N m^*}{2\hbar e^2 \epsilon_F} |\mathfrak{S}_{sf}|^2 (g_J - 1)^2 Jx(Jx + 1). \quad \text{I-23}$$

In the presence of a crystal field, the resistivity in the paramagnetic state ( $\rho_{spd}$ ), becomes temperature dependent and shows a broad curvature at high temperatures. It is also shown in Fig. I-5, that the resistivity curve for the RE intermetallic compounds exhibit a pronounced kink at  $T_{ord}$ , which is due to the influence of magnetism such as ferromagnetism with a Curie point  $T_C = T_{ord}$  or an antiferromagnetism with a Néel point  $T_N = T_{ord}$ . Physical properties such as electrical resistivity, magnetic susceptibility and specific heat are influenced by critical fluctuations at  $T_C$  or  $T_N$ .

In the vicinity of the ordering region, just below  $T_{ord}$ , the ordering of the localized spins sharply reduce the conduction electrons scattering, causing a pronounced kink at  $T_{ord}$ . The resistivity in this region is described by the molecular field approximation [57], neglecting correlations between the spins and taking an account only of the interaction of a spin with the average exchange field produced by neighbouring spins.

In the region well below the ordering temperature  $T_C$  or  $T_N$ , perfect magnetic order results in reduced scattering of the conduction electrons. Magnetic properties of the RE intermetallic compounds are described in terms of spin wave model. Therefore, the scattering of conduction electrons at low temperature may originate from both phonons and spin waves. However, in most magnetic materials, the scattering of conduction electrons by the spin waves contributes largely to the total resistivity. For ferromagnetic materials, several authors were able to derive a  $T^2$  dependence by assuming a spin wave spectrum  $\omega(q) \sim q^2$  [57, 58, 59]. In the presence of magnetic anisotropy, the  $T^2$  dependence resistivity of ferromagnetic material is modified when a gap  $\Delta$  in the spin wave spectrum occurs and takes the form [60]:

$$\rho_{4f}(T) = AT^2 \exp\left[-\frac{\Delta}{k_B T}\right], \quad \text{I-24}$$

where  $A$  is a constant and  $\Delta$  is the anisotropy gap in the spin wave dispersion, which represents the minimum energy required to excite a spin wave in the anisotropy field. For antiferromagnetic materials, the resistivity was derived to be proportional to  $T^4$  with the assumption that  $\omega(q) \sim q$ .

#### I-4-1-b: Magnetic resistivity of Kondo and HF systems

The appearance of the resistance minimum at temperatures where normal  $\rho(T) \sim T^5$  phonon contribution has been shown to be caused by magnetic moments diluted in the metal. This minimum in  $\rho(T)$  curve follows from the combined effect of the increased spin-disorder resistivity and the decreasing phonon scattering resistivity on cooling the sample. The theoretical explanation of this effect is due to Kondo [27]. The model suggested by Kondo showed that the spin-disorder resistivity is not a constant (Eq. I-23), but increases logarithmically with decreasing temperature, which is a result of conduction electron spin-flip scattering by the localized magnetic moment of the 3d or 4f ions. The scattering of the conduction electrons by the localized magnetic moments were treated perturbatively in the Born approximation including second-order corrections in  $\mathfrak{J}_{sf}$ . The resulting temperature dependence of the magnetic resistivity can be written as [8]:

$$\rho_{4f}(T) = \rho_{spd} \left[ 1 + \alpha N(E_F) \mathfrak{J}_{sf} \ln\left(\frac{T}{T_F}\right) \right], \quad \text{I-25}$$

where  $\alpha$  is a constant which depends on the nature of the local moment,  $T_F$  is the Fermi temperature corresponding to the Fermi energy,  $\mathfrak{J}_{sf}$  is the direct exchange integral and  $N(E_F)$  the density of states at the Fermi level. Eq. I-25 describes the logarithmic increase towards low temperatures only if, the sign of  $\mathfrak{J}_{sf}$  is negative due to the  $sp$  ( $d$ ) –  $f$  admixture interaction and consistent with the antiferromagnetic coupling. Furthermore, the validity of this equation is restricted to temperatures of the order of the Fermi temperature  $T_F$  below a characteristic temperature called the Kondo temperature  $T_K$  [61]:

$$T_K = \frac{D}{k_B} \exp\left[-\frac{1}{|\mathfrak{J}_{sf} N(E_F)|}\right], \quad \text{I-26}$$

where  $D$  is the half-wide of the conduction band. The perturbation theory used by Kondo is divergent and could not be applied to find  $\rho_{4f}(T)$  as  $T \rightarrow T_K$ . This divergence is due to the strong coupling between the conduction electrons and the localized magnetic moments and the formation of the narrow ( $\sim k_B T_K$ ) many-body resonance near the Fermi level at  $T \leq T_K$ . The Kondo temperature sets the dividing line between local moment behaviour, where the spin is free at high temperature ( $T \gg T_K$ ), and the low temperature limit, where the spin becomes highly corrected with the surrounding conduction electrons. Experimentally,  $T_K$  marks the low temperature limit of a Curie susceptibility [27]. Well below  $T_K$ , a Kondo system can be considered within the framework of the Fermi liquid model [31].

Following the Kondo problem, several authors were able to calculate the magnetic resistivity and the Kondo temperature of HF and Kondo systems using various models. Abrikosov [62] suggested an improvement of the Kondo's calculation by including further terms of the perturbation series (i.e., all order of  $\mathfrak{S}_{sf}$ ). The resulting  $4f$  resistivity is given by:

$$\rho_{4f}(T) = \frac{\rho_B}{\left[1 + \mathfrak{S}_{sf} N(E_F) \ln\left(\frac{1.13D}{k_B T}\right)\right]^2}, \quad \text{I-27a}$$

with:

$$\rho_B = \frac{3\pi n^* \mathfrak{S}_{sf}^2 J(J+1)n_f}{2NE_F e^2 \hbar}, \quad \text{I-27b}$$

where  $N$  is the total number of atoms in the crystal and  $n_f$  is the concentration of magnetic impurities ions. The corresponding Kondo temperature resulting from this calculation is given by [61]:

$$T_K = 1.13 \frac{D}{k_B} \exp\left[-\frac{1}{|\mathfrak{S}_{sf}| N(E_F)}\right]. \quad \text{I-28}$$

This approximation leads to a divergence in the scattering amplitude, which diverge for  $\mathfrak{S}_{sf} < 0$  at  $T_K$ .

In a perturbation approximation in  $\mathfrak{S}_{sf}N(E_F)$ , Cornut and Coqblin [59] calculated the magnetic contribution to the resistivity ( $\rho_{4f}$ ) of the  $4f$  impurities in a non-magnetic matrix in the presence of crystal field. The resistivity within this approximation is given by:

$$\rho_{4f}(T) = R_s + \Re \left[ 2N(E_F) \mathfrak{S}_{sf}^3 \frac{\lambda_n^2 - 1}{2J + 1} \ln \left( \frac{k_B T}{D^n} \right) \right], \quad \text{I-29}$$

where  $R_s$  is the contribution due to direct scattering processes or spin disorder resistivity given by:

$$R_s = \Re \left[ V^2 + \frac{\lambda_n^2 - 1}{(2J + 1)\lambda_n} \mathfrak{S}_{sf}^2 \right]. \quad \text{I-30}$$

$V$  is the direct scattering constant,  $\lambda_n$  is the effective degeneracy of the occupied  $4f$ -level given by  $\lambda_n = \sum_{i=0}^n \alpha_i$  with  $\alpha_i$  the degeneracies of the energy level  $E_i$ .  $\Re$  is a constant which incorporates quantities such as  $k_F$  or the mass of the conduction electrons. In the case

$\Delta_n \ll k_B T \ll \Delta_{n+1}$  ( $\Delta_n$  being the measure of the energy of the crystal-field levels with respect to the ground state), the resistivity behaves as  $-\ln T$  with an effective cut-off  $D^{(n)}$  and a slope proportional to  $(\lambda_n^2 - 1)$ . The corresponding Kondo temperature  $T_K^n$  for each occupied level is given by:

$$T_K^{(n)} = \frac{D^{(n)}}{k_B} \exp \left[ - \frac{\left( 1 + \frac{V^2 (2J + 1) \lambda_n}{\mathfrak{S}_{sf}^2 (\lambda_n^2 - 1)} \right)}{N(E_F) \lambda_n |\mathfrak{S}_{sf}|} \right]. \quad \text{I-31}$$

When the ground state is thermally populated, the corresponding Kondo temperature  $T_K^{(1)}$  is similar to  $T_K$  defined by Eq. I-28.  $\rho_{4f}(T)$  defined by Eq. I-29, is characterized by two features:

- A  $-\ln T$  dependence far away from  $\Delta_n$  at  $T \sim \Delta_n/k_B$ .
- For  $k_B T \ll \Delta_2$  and  $k_B T \gg \Delta_n$ , the ratio of  $-\ln T$ -dependent resistivity is given by:

$$Q = \frac{(\alpha_1^2 - 1)}{4J(J+1)}. \quad \text{I-32}$$

For Kondo lattice systems, several authors were able to calculate  $\rho(T)$  of the  $4f$  magnetic impurities by solving the periodic Anderson Hamiltonian using different approaches

[49, 64, 65]. They obtained different expressions of  $\rho_{4f}(T)$  for the whole temperature range ( $T \geq T_K$ ) and ( $T \leq T_K$ ). For example  $\rho_{4f}(T)$  obtained by Yoshimori and Kasai [49] is given by:

$$\rho_{4f}(T) = \alpha \left[ \left( \sqrt{\log^2\left(\frac{T}{T_K}\right) + \frac{3\pi^2}{4}} + \ln\left(\frac{T}{T_K}\right) \right)^2 + \beta \left( \sqrt{\log^2\left(\frac{T}{T_K}\right) + \frac{3\pi^2}{4}} - \log\left(\frac{T}{T_K}\right) \right)^2 \right]^{-1}, \quad \text{I-34}$$

with  $\alpha$  a constant and  $\beta = 2 \frac{(\pi N(E_F)V)^2}{\lambda}$  a material constant. At temperatures well below the Kondo temperature ( $T \leq T_K$ ), Fermi liquid behaviour is obtained where:

$$\rho_{4f}(T) = \alpha \left( \frac{8\beta}{3} \right) \left( \frac{T}{T_K} \right)^2. \quad \text{I-35}$$

The overall resistivity results obtained for a Kondo lattice system account well for the observed experimental data. At very low temperatures a  $T^2$  Fermi liquid behaviour of  $\rho(T)$  is achieved. With increase in temperature roughly at  $T = 2T_K$ ,  $\rho(T)$  goes through a maximum which is followed with a logarithmic dependence on temperature. Fig. I-6 shows the results derived by Cox and Grewe [66];  $\rho(T)$  shows a peak at temperature slightly below  $T_0$ . This is followed by a decrease with decreasing temperature and a  $T^2$  behaviour as  $T \rightarrow 0$  K. The observed resistivity maximum separates the incoherent single-ion Kondo scattering for  $T > T_0$  from the low temperature regime, where residual interactions occur between these scattering sites [8]. Well below the Kondo temperatures  $T \leq T_K$ , several theoretical investigations were reported for the  $4f$  resistivity using different methods and theories such as, the renormalization group method [35], the phonological Fermi-liquid theory [31]. The following expressions of the resistivity were obtained:



$$\rho_{4f}(T) = \rho_0 [1 + (aT)^2]^{-1}, \quad \text{I-36}$$

$$\rho_{4f}(T) = \rho_0 \left[ 1 - b \left( \frac{T}{T_K} \right)^2 \right], \quad \text{I-37}$$

where  $a$  is a constant determined intrinsically by the density of states at the Fermi level,

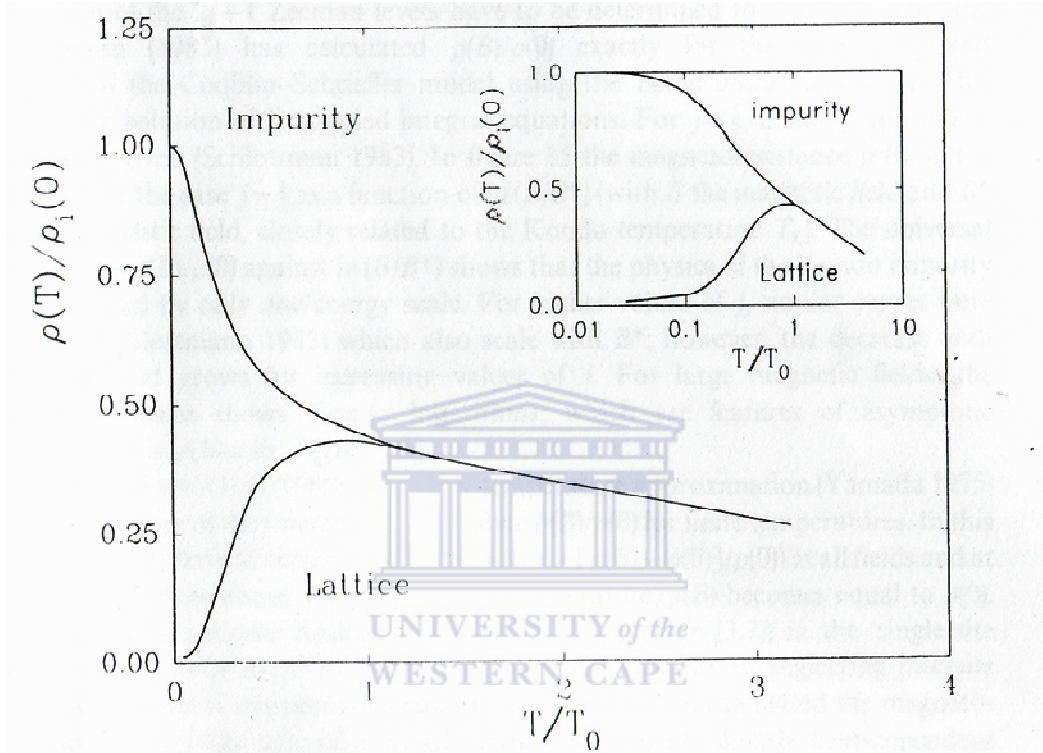


**Figure 1-6:** Temperature dependence of the resistivity of a single-impurity Kondo system and a Kondo lattice.  $\rho_i(0)$  is the zero temperature resistivity per ion in the dilute limit [66].

$\rho_0$  is the resistivity at  $T = 0$ , in the absence of magnetic ordering or superconducting behaviour [31] and  $b$  is a constant taking a value of  $\frac{\pi}{16}$  [67, 68, 69] or  $\frac{5\pi^2}{12}$  [70].

Recent experimental investigations on strongly correlated  $f$ -electron systems have revealed new phenomena well below  $T_K$ , where the normal Fermi-liquid behaviour is expected. These are:

- the non-Fermi-liquid behaviour, where the physical properties of the systems exhibit a weak power law or logarithm divergence in temperature, leading to the occurrence of

quantum critical point at  $T = 0$  K. The temperature dependence of the  $4f$  resistivity characteristic of non-Fermi-liquid behaviour is given in the form:

$$\rho_{4f}(T) \sim 1 - a \left( \frac{T}{T_0} \right)^n, \quad \text{I-38}$$

where  $T_0$  is a characteristic temperature for non-Fermi-liquid,  $a$  is a positive or negative constant and the values  $1 \leq n < 2$ . Non-Fermi liquid behaviour was observed in several doped and undoped HF systems. Examples of these are:  $\text{Ce}(\text{Cu}_{6-x}\text{Au}_x)$  [71];  $(\text{U}_{1-x}\text{Th}_x)\text{Ru}_2\text{Si}_2$  [72];  $(\text{Ce}_x\text{La}_{1-x})\text{Cu}_{2.2}\text{Si}_2$  ( $x = 0.1$ ),  $\text{CeCu}_2\text{Si}_2$ ,  $\text{CeNi}_2\text{Ge}_2$  [73] and  $\text{U}_2\text{Pt}_2\text{In}$  [74].

- The Semiconducting behaviour with an activation type of increase of the resistivity with decreasing temperature. Two distinct behaviours are observed for the resistivity. The first type of behaviour is an activation type of increase in  $\rho(T)$  with decreasing temperature taking the form [75]:

$$\rho_{4f}(T) = C \exp\left(-\frac{\Delta}{k_B T}\right), \quad \text{I-39}$$

where  $C$  is a variable coefficient and  $\Delta$  is the energy gap open in the Fermi surface due to the hybridization of the conduction electron with the nearly localized  $f$ -electron. An example of typical HF system exhibiting this type of behaviour is  $\text{Ce}_3\text{Bi}_4\text{Pt}_3$  [76]. The second type of behaviour for  $\rho(T)$  is the observed maximum followed by a minimum with decreasing temperature and then a final increase as  $T \rightarrow 0$  K due to the formation of a gap. Examples showing this behaviour are:  $\text{U}_2\text{Ru}_2\text{Sn}$  [77],  $\text{CeNiSn}$  and  $\text{CeRhSn}$  [78, 79].

### I-3-2: Magnetic susceptibility and magnetization

The magnetic susceptibility and magnetization to be described in this section is that of the  $4f$  systems. These properties may be calculated from the free energy of the  $4f$  impurities. In the static homogeneous magnetic field, the magnetization  $M$  and the magnetic susceptibility  $\chi$  of the  $4f$  impurities are expressed as follows:

$$M(T) = \frac{\partial F_{4f}(T)}{\partial H}, \quad \text{I-39}$$

$$\chi(T) = \frac{M(T)}{H}, \quad \text{I-40}$$

where the free energy  $F_{4f}$  is obtained from the  $4f$  partition function  $Z_{4f}$  defined in reference [80] by:

$$F_{4f}(T) = -k_B T \ln(Z_{4f}(T)). \quad \text{I-41}$$

$Z_{4f}$  is related to the distribution functions for the empty and occupied  $4f$ -orbital configuration [81] and depend on the temperature in the presence of hybridization. Indeed  $\chi$  measures the ease with which a material acquires magnetization in the presence of an applied magnetic field  $H$ . Thus a description of the magnetic susceptibility of the  $4f$  impurities gives a substantial description of the magnetization of the  $4f$  impurities.

Magnetic susceptibility was first calculated for a single impurity Kondo effect. The result obtained by Wilson [35], shows that, the Kondo effect leads to the crossover from “asymptotic freedom” at high temperatures ( $T \gg T_K$ ) which correspond to a quasi-free behaviour of the Ce  $-$ ions to “infrared slavery” at low temperatures corresponding to a bound state, where the spin becomes highly correlated with the surrounding conduction electrons. In the high temperature regime, the  $\chi(T)$  is well described by the Currie-Weiss relationship (Eq. I-7) given the full effective magnetic moment  $\mu_{\text{eff}}$  of the  $4f$ -impurities ions. In the low temperature regime  $T \ll T_K$ , the effective magnetic moment is fully quenched. The calculated magnetic susceptibility for  $T = 0$  K in the case  $s = j = 1/2$  is given by [35]:

$$\chi(0) = \frac{0.103(g_J \mu_B)^2}{T_K}. \quad \text{I-42}$$

Subsequent to Wilson’s calculation, Rajan [82] was able to solve the exact thermodynamic equation of the Coqblin-Schrieffer model [83] in the scaling regime. The impurity susceptibility in zero-temperature and zero-field limits in the case  $j = 1/2, \dots, 7/2$  is given in the form:

$$\chi(0) = \frac{v(v^2 - 1)g_J \mu_B^2}{24k_B T_0}, \quad \text{I-43}$$

where  $\nu = 2j + 1$  is the degeneracy and  $T_0$  is a strong-coupling scale which is related to the scaling temperature  $T_K$  through the Wilson number  $W_j$  for the  $\nu = 2$  case,  $j = 1/2$  and  $\frac{T_K}{T_0} = 1.2902$  [84]. The results obtained by Rajan are shown in Fig.1-7. The plot of

$\chi(T)/\chi(0)$  for  $j = \frac{1}{2}, \dots, \frac{7}{2}$  as function of temperature indicate a strong-coupling at low temperature where the effective moment goes to zero, showing the complete screening of the impurity spin by the conduction electrons. As the temperature increases, there is a crossover to the asymptotic freedom regime. For  $j > 1$ , a peak is observed in  $\chi(T)$  curve and becomes more pronounced as  $j$  increases. Such susceptibility behaviour was observed in Ce ( $j = 5/2$ ) and Yb ( $j = 7/2$ ) based HF compounds [85, 86].

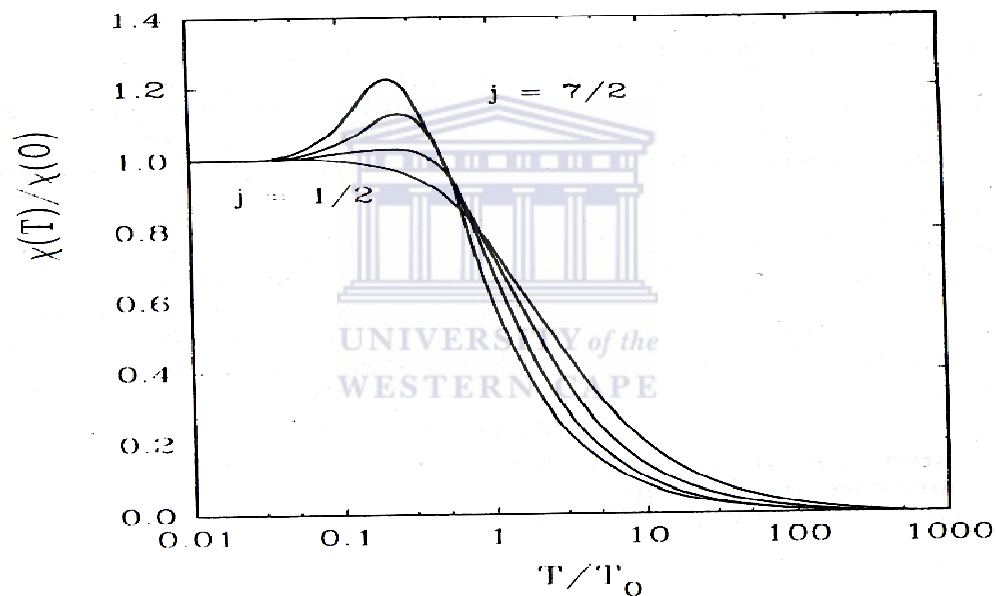


**Figure 1-7:** Temperature-dependence magnetic susceptibility  $\chi(T)/\chi(0)$  of the Coqblin-Schrieffer model obtained by the Bethe ansatz solution for different values of  $j$  [82].

The magnetic susceptibility of RE compounds which exhibit interconfiguration fluctuation has been reported by several workers [87, 88, 89, 90, 91, 92]. The susceptibility curve exhibits a broad maximum at high temperature. Sales and Wohleben [87] reported the magnetic susceptibility of these compounds in a model which assumes an energy separation  $E_{ex}$  between the two configurations and an intrinsic lifetime  $\tau$  due to the  $4f$  impurities-

conduction electrons interaction. The resulting magnetic susceptibility can be expressed in the form:

$$\chi(T) = N \frac{\mu_n^2 v(T) + \mu_{n-1}^2 (1 - v(T))}{3k_B (T + T_{sf})}, \quad \text{I-44}$$

where  $v(T)$  is the fractional occupation of the state  $E_n$  (fractional valence) given by:

$$v(T) = \frac{2J_n + 1}{(2J_n + 1) + (2J_{n-1} + 1) \exp\left[-\frac{E_{ex}}{k_B (T + T_{sf})}\right]}. \quad \text{I-45}$$

$\mu_n$  and  $\mu_{n-1}$  are the effective Hund's rule magnetic moments in the two configurations,  $(2J_n + 1)$  and  $(2J_{n-1} + 1)$  are the degeneracies of the two levels  $E_n$  and  $E_{n-1}$  and  $T_{sf}$  is the spin fluctuation temperature. The energy separation  $E_{ex}$  can be either negative or positive corresponding to the magnetic configuration (e.g.  $4f^{13}$  on Yb or  $4f^1$  on Ce) lying higher and lower in energy respectively. Eq. I-44 and I-45 agree with the Curie-Weiss law down to  $T = 0$  K if  $E_{ex} > 0$ . The susceptibility derived from this model (Eq. I-44 and I-45) was found to be in good agreement with the experimental data of the interconfiguration fluctuation compounds  $\text{YbB}_4$ ,  $\text{YbAl}_3$ ,  $\text{YbC}_2$  and  $\text{YbCu}_2\text{Si}_2$  [87]. On the other hand Béal-Monod and Lawrence [88] derived the low temperature susceptibility in a model, which assumes that the  $4f$  level is very close to the Fermi level and its position is fixed relative to the conduction band. The resulting magnetic susceptibility is given in the form:

$$\chi(T) = \chi(0) \left[ 1 + a \left( \frac{T}{T_{sf}} \right)^2 \right], \quad \text{I-46}$$

for  $T = T_{sf}$  with  $\chi(0) \propto 1/T_{sf}$ . The factor  $a$  is a number of order of unity which can be positive or negative depending on the density of states at the Fermi level. The calculated  $\chi(T)$  given by Eq. I-46 are in good agreement with the experimental data of the weak interconfiguration fluctuation system  $\text{Ce}(\text{In}, \text{Sn})_3$  [88].

## I-5 Specific heat capacity

The low temperature specific heat represents a distinguishing feature of HF materials, and originates from various contributions. These include:

a) The lattice or phonon contribution ( $C_L$ ) given by the Debye theory in the form:

$$C_L = 9Nk_B \left( \frac{T^3}{\theta_D} \right)^{\theta_D/T} \int_0^{\theta_D/T} \frac{x^3 e^x}{(e^x - 1)^2} dx, \quad \text{I-47}$$

with  $x = \frac{\hbar\omega}{k_B T}$ .  $\theta_D$  is the characteristic Debye temperature of the compounds which indicate the lattice vibrational spectra of the compounds.  $N$  is the number of atoms in the samples. In the low temperature regime  $C_L$  can be approximated as:

$$C_L = \frac{12\pi^4}{5} Nk_B \left( \frac{T^3}{\theta_D} \right). \quad \text{I-48}$$

Experimentally the phonon contribution of HF compound with Ce or Yb based RE elements is obtained from their non-magnetic La, Y, or Lu counterparts.

b) The electronic heat capacity  $C_e$  which is the most important term used to identify a HF materials is given by:

$$C_e = \gamma T. \quad \text{I-49}$$

The electronic coefficient  $\gamma$  also known as the Sommerfeld coefficient is proportional to the density of states at the Fermi level  $N(E_F)$ , which in turn is proportional to the effective mass of the conduction electrons  $m^*$  via the relation [93]:

$$\gamma = \frac{2}{3} \pi^2 k_B^2 N(E_F) = \frac{k_B^2 k_F}{3\hbar^3} m^*. \quad \text{I-50}$$

Similar to the susceptibility, several theoretical investigations were reported for an expression of  $\gamma$  in the case of HF and Kondo systems using different methods and approaches [36, 42, 82, 84, 94]. Oliveira and Wilkins [36] within the renormalization group calculation obtained the zero temperature limit of the specific heat in the form:

$$\lim_{T \rightarrow 0} \frac{C(T)}{T} = \gamma(0) = \frac{2\pi^2}{3} = \frac{0.103R}{T_K} \quad \text{I-}$$

51

where,  $R$  is the gas constant. On the other hand, Desgrange and Schotte [95] obtained the exact low temperature limit using the Bethe-ansatz method given by:

$$\lim_{T \rightarrow 0} \frac{C(T)}{T} = \gamma(0) = \frac{\pi R}{3T_K} \quad \text{I-52}$$

for  $\frac{T}{T_K} < 0.05$ . Rajan [82] suggested the zero-temperature limit for  $j > \frac{1}{2}$  which scale with the

degeneracy  $N = 2j + 1$  in the form:

$$\lim_{T \rightarrow 0} \frac{C(T)}{T} = \gamma(0) = \frac{(N-1)\pi R}{6T_0} \quad \text{I- 53}$$

where  $T_0$  is related to  $T_K$  via the Wilson number (see section I-3-2).

c) The magnetic contribution  $C_M$  in the case of the magnetic materials. For Ferromagnet  $C_M$  is obtained in the spin wave model [96] and given as:

$$C_M(T) = \alpha T^{3/2} \quad \text{I- 54}$$

with  $\alpha$  a parameter which depends on the structure of the materials and the quantum mechanical exchange constant. For Antiferromagnet  $C_M \sim T^3$ .

d) The Schottky term,  $C_{sch}$  which originates whenever an ion can occupy different energy levels. In the case of two energy levels  $\epsilon_0$  and  $\epsilon_1$ , the Schottky term can be written as [96]:

$$C_{sch}(T) = R \left( \frac{\Delta}{k_B T} \right)^2 \frac{\left( \frac{g_0}{g_1} \right) \exp\left( \frac{\Delta}{k_B T} \right)}{\left[ 1 + \left( \frac{g_0}{g_1} \right) \exp\left( \frac{\Delta}{k_B T} \right) \right]^2}, \quad \text{I-55}$$

where  $\Delta$  is the energy separation,  $g_0$  and  $g_1$  are the degeneracies of the two energy levels  $\epsilon_0$  and  $\epsilon_1$ .



## References

---

- 1) K. H. J. Buschow, “*Intermetallics compounds of rare earth and 3d transition metals*”, *Rep. Prog. Phys.* **40**, 1179-1256 (1977).
- 2) E. Gratz and M. J. Zuckermann, “*Handbook on Physics and Chemistry of the Rare Earths*”, eds Gschneider K. A. Jr., and Eyring L., (Northern–Holland: Amsterdam), **Vol.5**, chap.42, 117 (1982).
- 3) K. A. Gschneidner Jr and A. H. Daane “*Handbook on Physics and Chemistry of the Rare Earths*”, eds. Gschneidner K.A .Jr. and Eyring L., ( Northern–Holland: Amsterdam) **Vol.11**, 409 (1988).
- 4) N. N. Greenwood, and A. Earnshaw, *Chemistry of elements* (1<sup>st</sup> ed., pp. 1423-1449) Oxford, UK (1984).
- 5) K. A. Gschneidner Jr., *J. Less Common Metals* **29**, 293 (1969).
- 6) E. F. Havinya, K. H. J. Buschow and H. J. van Daal, *Solid Stat. Comm.* **13**, 621 (1973).
- 7) B. Coqblin, “*Magnetism of metals and alloys*” ed. M. Cyrot (North – Holland: Amsterdam, Chap. 3 (1982).
- 8) E. Bauer, *Adv. Phys.* Vol. **40**, 417 (1991).
- 9) K. A. McEwen, “*Handbook on the Physics and Chemistry of the Rare Earths*”, eds. Gschneidner K.A .Jr. and L.Eyring, (Northern–Holland: Amsterdam) **Vol.1**, 411 (1978).
- 10) K. N. R. Taylor, *Adv.Phys.***20**, 551 (1971).
- 11) N. B. Brandt and V. V. Moshchalkov, *Adv. Phys.* **33**, 373 (1984).
- 12) N. E. Alekseevskii and P. Gaidukov Yu, *Zh. Eksp. Teor. Fiz.* **31**, 947 (1956).
- 13) A. C. Hewson, “*The Kondo problem to Heavy-fermions*” Cambridge: University press” (1993).
- 14) G. R. Stewart, *Rev. Mod. Phys.* **56**, 755 (1984).
- 15) A. Amato, D. Jaccard, J. Flouquet, F. Lapierre, J. L. Tholence, R. A. Fisher, S. E. Lacy, J. A. Olsen and N. E. Phillips, *J. Low Temp. Phys.* **68**, 371 (1987).
- 16) C. Kittel, “*Introduction to solid state physics*”, 7<sup>th</sup> edition (Wily J. and Sons) (1996).
- 17) F. J. Blatt, “*Physics of electronic conduction in solids*”, (McGraw – Hill: New York) (1968).
- 18) K Andres., J. E Graebner and H.R Ott., *Phys. Rev. Lett.* **35**, 1779 (1975).



- 19) J. R. Schrieffer and P. A. Wolff, *Phys. Rev.* **149**, 491 (1966).
- 20) S. Doniach, *Physica B* **91**, 231 (1977).
- 21) G. Sereni and J. P. Kappler, *J. Phys.: Condensed Matter* **6**, 4772 (1994).
- 22) F. Steglich, U. Rauchschwalbe, U. Gottwick, H. M. Mayer, G. Spam, N. Grewe, U. Poppe and J. J. M. Franse, *J. Appl. Phys.* **57** (1985) 3054.
- 23) M. B. Tchoula Tchokonté, P. de V. Du Plessis, A. M. Strydom and D. Kaczorowski, *J. Magn. Magn. Mater.* **226**, 173 (2001).
- 24) A. Eiling and J.S. Schilling, *Phys. Rev. Lett.* **46**, 364 (1981).
- 25) M. Lavagna, C. Lacroix, M. Cyrot, *J. Phys. F: Met. Phys.* **13**, 1007 (1983).
- 26) C.S. Garde, J. Ray and J. Chandra, *J. Phys.: Condens. Matter* **1**, 2737 (1989).
- 27) J. Kondo, *Prog. Theor. Phys.* **32**, 37 (1964).
- 28) M. B. Tchoula Tchokonté, P. de V. Du Plessis, A. M. Strydom, D. Kaczorowski, A. Czopnik and Z. Kletowski, *J. Phys.: Condens. Matter* **16**, 1981 (2004).
- 29) A. Sumiyama, Y. Oda, H. Nagano, Y. Onuki, K. Shibusaki and T. Komatsubara, *J. Phys. Soc. Jpn.* **55**, 1294 (1986).
- 30) M. B. Tchoula Tchokonté, P. de V. Du Plessis and D. Kaczorowski, *J. Phys.: Condens. Matter* **15**, 3767 (2003).
- 31) P. Nozieres, *J. Low Temp. Phys.* **17**, 31 (1974).
- 32) P.W. Anderson, *Phys. Rev.* **124**, 41(1961).
- 33) B. Coqblin and J. R. Schrieffer, *Phys. Rev.* **185**, 847 (1969).
- 34) A. H. Wilson, “*The theory of metals*”, (London: Cambridge University Press) (1953).
- 35) K. G. Wilson, *Rev.Mod.Phys.***47**, 773 (1975).
- 36) L. N. Oliveira and J. W. Wilkins, *Phys. Rev. Lett.* **47**, 1553 (1981).
- 37) H. R. Krishna-Murthy, K. G. Wilson and J. W. Wilkins, *Phys. Rev. Lett.* **35**, 1101 (1975); *Phys. Rev.* **B21**, 1003 (1980); *Phys. Rev.* **B21**, 1044 (1980).
- 38) D. N. Newns and A. C. Hewson, *J. Phys. F: Met. Phys.* **10**, 2429 (1980).
- 39) H. J. Leder and B. Z. Muhlzhlegel, *Physik B: Cond. Matter* **29**, 341 (1978).
- 40) T. Costi, *J. Magn. Magn. Mater.* **47-48**, 384 (1985).
- 41) H. Kaga and H. Kubo, *Physica B* **147**, 205 (1987).
- 42) H. Kaga and H. Kubo, *Solid State Commun.* **65**, 257 (1988).
- 43) N. Grewe, *Solid State Commun.* **50**, 19(1984).
- 44) T. M. Rice and K. Ueda, *Phys. Rev.* **B 34**, 6420 (1986).
- 45) C. Lacroix and M. Cyrot, *Phys. Rev.* **B 20**, 1969 (1979).
- 46) N. Read, D. M. Newns and S. Doniach, *Phys. Rev.* **B 30**, 3841 (1984).

- 47) C. Lacroix, *J. Magn. Magn. Mater.* **60**, 145 (1986); *J. Magn. Magn. Mater.* **63 – 64**, 239 (1987).
- 48) P. Coleman, *Phys. Rev.* **B 29**, 3035 (1984).
- 49) A. Yoshimori and H. Kasai, *J. Magn. Magn. Matter.* **31-34**, 475 (1983).
- 50) F. J. Blatt, P. A. Schroeder, C. A. Foiles and D. Greig., “*Thermoelectric power of metals*”, (Plenum: New York) (1976) 170.
- 51) R. G. Chambers., “*Electrons in metals and semiconductors*”, (Chapman and Hall: London) (1990).
- 52) M. N. Rudden and J. Wilson, “*Elements of Solid State Physics*” 2<sup>nd</sup> edition, John Wiley and Sons (1993) p.81.
- 53) J. M. Ziman, “*Electrons and Phonons*”, (Oxford University Press, London) (1965).
- 54) T. Kasuya, *Prog. Theor. Phys.* **16**, 45 (1956).
- 55) P. G. de Gennes and J. Friedel, *J. Phys. Chem. Solids* **4**, 71 (1958).
- 56) A. J. Dekker, *J. Appl. Phys.* **36**, 906 (1965).
- 57) T. Kasuya, *Prog. Theor. Phys.* **22**, 227 (1959).
- 58) I. Mannari, *Prog. Theor. Phys.* **22**, 335 (1959).
- 59) N.V. Volkenshlein, V. P. Dyakina, V. E. Startsev, *Phys. Stat. Sol.* **B 57**, K9 (1973).
- 60) A. R. Mackintosh, *Phys. Lett.* **4**, 140 (1963).
- 61) K. Fisher, *Phys. Stat. Sol.* **B46**, 11 (1971).
- 62) A. A. Abrikosov, *Physics* **2**, 5 (1965).
- 63) B. Cornut and B. Coqblin, *Phys. Rev.* **B5**, 454 (1972).
- 64) C. S. Garde and J. Ray, *Phys. Rev.* **B51**, 2960 (1995).
- 65) M. Lavagna, C. Lacroix and M. Cyrot, *J. Phys. F: Met. Phys.* **12**, 745 (1982).
- 66) D. L. Cox and N. Grewe, *Z. Physik B: Condens.Matter* **71**, 321 (1988).
- 67) K. Yamada, *Prog. Theor. Phys.* **53**, 970 (1975).
- 68) K. Yamada, *Prog. Theor. Phys.* **54**, 316 (1975).
- 69) K. Yosida and K. Yamada, *Prog.Theor. Phys.* **53**, 1286(1975).
- 70) A. Yoshimori, *Prog Theor. Phys.* **55**, 67 (1976).
- 71) H. v Löhneysen, *J. Phys.:Condens.Matter* **8**, 9689 (1996).
- 72) H. Amitsuka, T. Hidano, T. Honma, H. Mitamura and T. Sakakibara, *Physica* **B 186-188**, 337 (1993).
- 73) B. Andraka, *Phys. Rev.* **B 49**, 3589 (1994); F. Steglich, P. Hellmann, S. Thomas, P. Gegenwart, A. Link, R. Helfrich, G. Span, M. Lang, C. Geibel and W. Assmus, *Physica* **B 237 & 238**, 192 (1997).

- 74) A. M. Strydom and du P. de V. du Plessis, *Physica B* **223 & 224**, 250 (1996); P. Estrela, L. C. J. Pereira, A. de Visser, F. R. de Boer, M. Almeida, M. Godinho, J. Rebizant and J. C. Spirlet, *J.Phys.:Condens.Matter* **10**, 9465 (1998).
- 75) G. Aeppli and Z. Fisk, *Comment Condens. Matter Phys.***16**, 155 (1992).
- 76) M. F. Hundley, P. C. Canfield, J. D. Thompson, Z. Fisk and J.M. Lawrence., *Phys. Rev. B* **42**, 6842 (1990).
- 77) L. Menon, P. de V. du Plessis and A.M. Strydom, *Solid State Commun.* **106**, 519 (1998); P. de V. du Plessis, A. M. Strydom, R. Troć and L Menon, *J.Phys.:Condens.Matter* **13**, 8375 (2001).
- 78) T. Takabatake, G. Nakamoto, T. Yoshimo, H. Fujii, K. Izawa, S. Nishigori, H. Goshima, T. Suzuki, T. Fujita, K. Maezawa, T. Hiraoka, Y. Okayama, I. Oguro, A. A. Menovsky, K. Neumairer, A. Brückl and K. Andres, *Physica B* **223&224**, 413 (1996).
- 79) S. K. Malik, L. Menon, K. Ghosh and B. Ramakrishnan, *Phys. Rev* **51**, 399 (1995).
- 80) G. Zwircknagl, E. Runge, N. E. Christensen, *Physica B***163**, 97 (1990).
- 81) N. E. Bickers, D. L. Cox and J. M. Wilkins, *Phys. Rev. B* **36**, 2036 (1987).
- 82) V. T. Rajan, *Phys. Rev. Lett.* **51**, 308 (1983).
- 83) B. Coqblin and J. R. Schrieffer, *Phys. Rev.* **185**, 847 (1969).
- 84) N. Andrei and J. H. Lowenstein, *Phys. Rev. Lett.* **46**, 356 (1981).
- 85) J. M. Lawrence, P. S. Riseborough and R. D. Parks, *Rep. Prog. Phys.* **44**, 1 (1983).
- 86) D. N. Newns, A. C. Hewson, J. W. Rasul and N. Read, *J. Appl. Phys.* **53**, 7877 (1982).
- 87) B. C. Sales and D. K. Wohlleben, *Phys. Rev. Lett.* **35**, 1240 (1975).
- 88) M. T. Béal-Monod and J. M. Lawrence, *Phys. Rev. B* **21**, 5400 (1980).
- 89) C. M. Varma and Y. Yafet, *Phys. Rev. B* **13**, 2950 (1976).
- 90) A. Bringer and H. Lustfeld, *Z. Physik B: Condens.Matter* **28**, 213 (1977).
- 91) H. Lustfeld and A. Bringer, *Solid State Commun.* **28**, 119 (1977).
- 92) S. K. Sinha and A. J. Fedro, *J de Physique* **40** C4, 214 (1979).
- 93) F.J. Blatt, “*Physics of electronic contribution in Solids*”, (McGraw-Hill: New York) (1968).
- 94) H. –U. Desgranges and K. D. Schotte, *Phys. Rev. Lett.* **91A**, 240 (1982).
- 95) S. H. Lui, *Phys. Rev.* **121**, 451 (1961).
- 96) E. S. R. Gopal, “*Specific Heat at Low Temperature*”, (Plenum Press: New York) (1966).

# Chapter II:

---

## Experimental techniques

This chapter presents a description of the experimental techniques used for: sample preparation and characterization, the study of electrical resistivity, magnetic susceptibility and magnetization.

### II-1: Sample preparation

The polycrystalline samples involved in this study are:  $(\text{Ce}_{1-x}\text{RE}_x)\text{Pt}_2\text{Si}_2$  (RE=Dy,Tb) and  $(\text{Ce}_{1-x}\text{Tb}_x)\text{Cu}_5\text{In}$ . All the compositions of these alloys systems, together with their non-magnetic counterparts  $\text{LaPt}_2\text{Si}_2$  and  $\text{LaCu}_5\text{In}$  were prepared from their constituent elements weighted to a relative error of  $\pm 0.5 \mu\text{g}$  using a microbalance (Nettler H18). All the constituent elements were obtained from Alfa Aesar company with the following purity in wt%: Ce: 99.98; La: 99.99; Cu: 99.99; Dy: 99.99; Tb: 99.99; Pt: 99.99 and In: 99.999. The polycrystalline samples of these systems were prepared by arc-melting the constituent elements on a water-cooled copper hearth in a titanium gathered Argon atmosphere (50 kPa below atmospheric pressure) at the School of Physics, University of the Witwatersrand using an arc-furnace melting chamber (Figs II-1 and II-2).



**Figure II-1:** Arc-melting furnace chamber at the University of the Western Cape (Physics Department), similar to that utilized at Wits University.

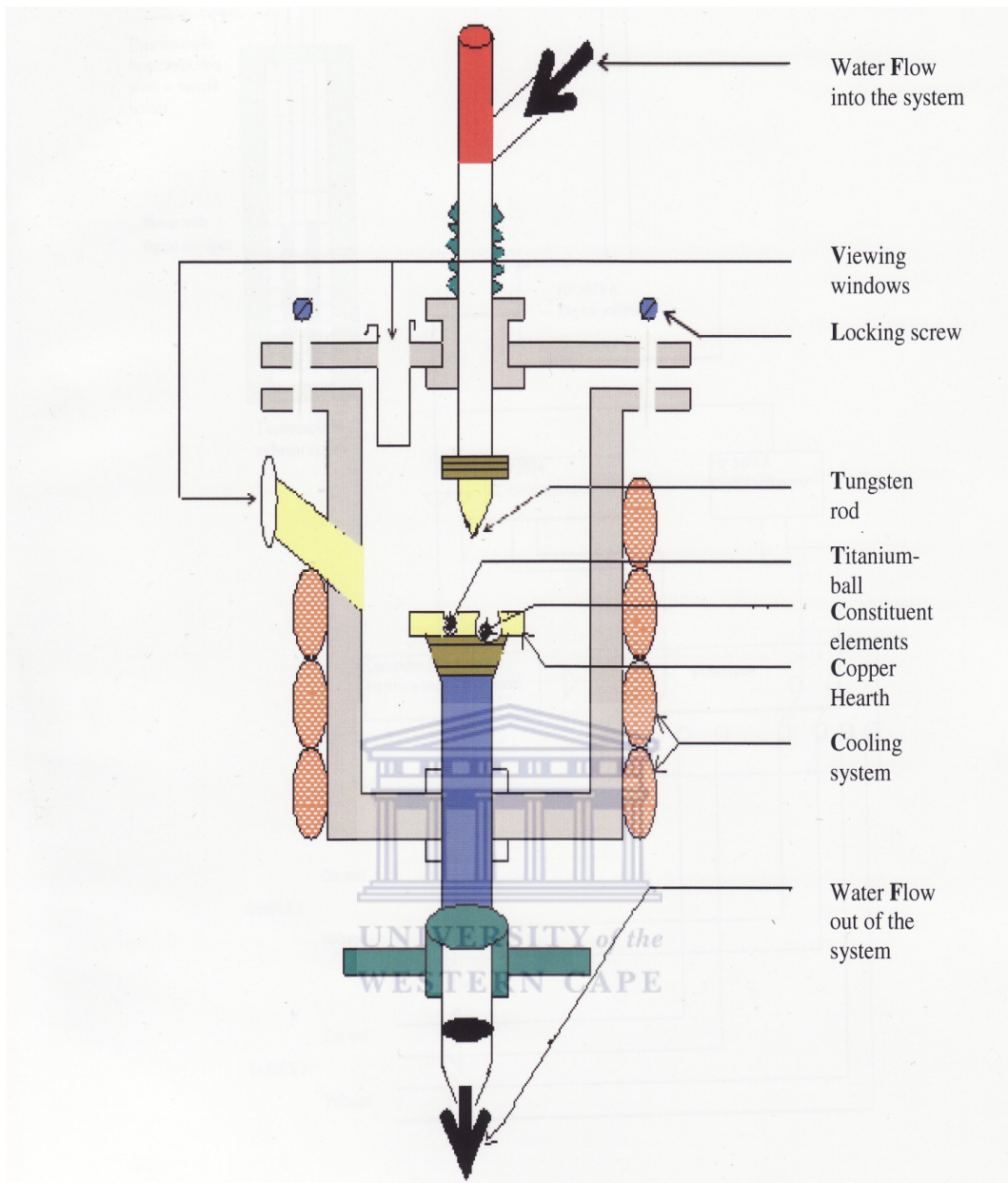


**Figure II-2:** Schematic diagram of the arc-furnace melting chamber.

The sample was melted three to four times to ensure good homogeneity. Due to high volatilization of In element, an excess of this element was added for each composition of the  $(\text{Ce}_{1-x}\text{Tb}_x)\text{Cu}_5\text{In}$  system. The weight losses after final melting were always smaller than 1% for all the systems without In, and did not exceed 1% relative to the In excess for the  $(\text{Ce}_{1-x}\text{Tb}_x)\text{Cu}_5\text{In}$  system. The typical mass of all the oblate shape ingots after final melting was 4 g. Electrical resistivity, magnetic susceptibility and magnetization measurements were performed on as-cast sample. The samples for resistivity, susceptibility and magnetization measurements were cut from the as-cast ingot using a Micracut 125 low speed precision



cutter with a diamond coated blade of thickness 0.381 mm (Fig II-3). Sample for resistivity measurements were cut in the form of a parallelepiped rectangle with typical dimensions  $1 \times 1 \times 6 \text{ mm}^3$ . These dimensions were measured using a travelling microscope to an accuracy of  $\pm 5\mu\text{m}$  with a geometrical uncertainty of  $\frac{A}{\ell} \pm 2\%$ , where  $A$  is the cross-sectional area of the sample and  $\ell$  is the length.



**Figure II-3:** Micracut 125 low speed cutter at the University of the Western Cape (Physics Department).

Samples for magnetic susceptibility and magnetization were cut in the form of a cube with a typical dimensions of  $1 \times 1 \times 1 \text{ mm}^3$ . Both resistivity and magnetic susceptibility samples were cut out of the centre part of the ingot, in order to avoid the bottom surface and the top layer where the stress in the material as evidenced by hairline cracks was sometimes found. Part of the as-cast ingot was used for x-ray diffraction (XRD) measurement for structural characterization as discussed in the next section.

## II-2: Sample characterization

The structural analyses of all compositions of the families of systems prepared viz:  $(\text{Ce}_{1-x}\text{RE}_x)\text{Pt}_2\text{Si}_2$  and  $(\text{Ce}_{1-x}\text{Tb}_x)\text{Cu}_5\text{In}$  were performed using a Bruker D8 Advance X-ray diffractometer with  $\text{Cu K}\alpha$  radiation ( $\lambda = 1.540598 \text{ \AA}$ ) at iThemba LABS (Fig II-4).



**Figure II-4:** X-ray diffractometer (D8 Advance) at iThemba LABS, Cape Town.

Part of the as-cast ingot prepared was finely ground in an agate mortar and subsequently spread out on a hollow rectangular sample holder. The diffraction patterns were measured in the range  $20^{\circ} \leq 2\theta \leq 90^{\circ}$ . The room-temperature X-ray powder diffraction spectra of all compositions prepared in the  $(\text{Ce}_{1-x}\text{RE}_x)\text{Pt}_2\text{Si}_2$  series could be indexed according to the tetragonal  $\text{CaBe}_2\text{Ge}_2$ -type structure with space group  $P4/nmm$ , while for compositions in the  $(\text{Ce}_{1-x}\text{Tb}_x)\text{Cu}_5\text{In}$  series, the room-temperature powder diffraction pattern could be indexed according to the orthorhombic  $Pnma$  up to 40% Ce substitution. No evidence of parasitic phases or unreacted elements was found in the X-ray patterns. Individual peak positions, lattice parameters, unit-cell volume and crystal structure were determined using Pawley Cell and Intensity Least (CAIL) square fit and Rietveld refinement from TOPAS ACADEMIC program.

### II-3: Electrical resistivity measurements

The sample holder for resistivity measurements is shown in Fig II-5 and Fig II-6 and has been designated to accommodate three samples at a time.

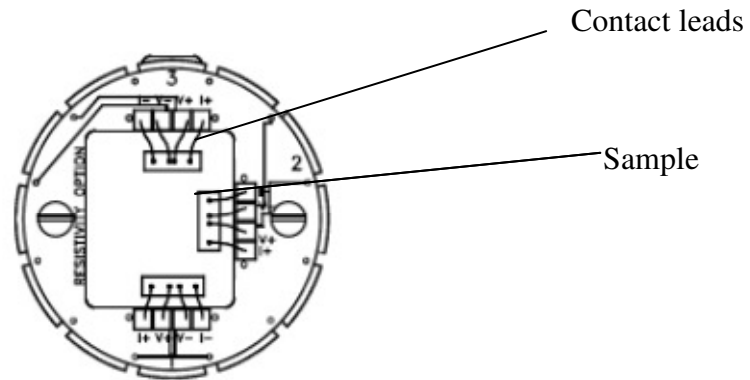


**Figure II-5:** Schematic diagram of the dc sample puck with three samples mounted for four wire resistance measurements (PPMS user manual, Quantum design, San Diego).

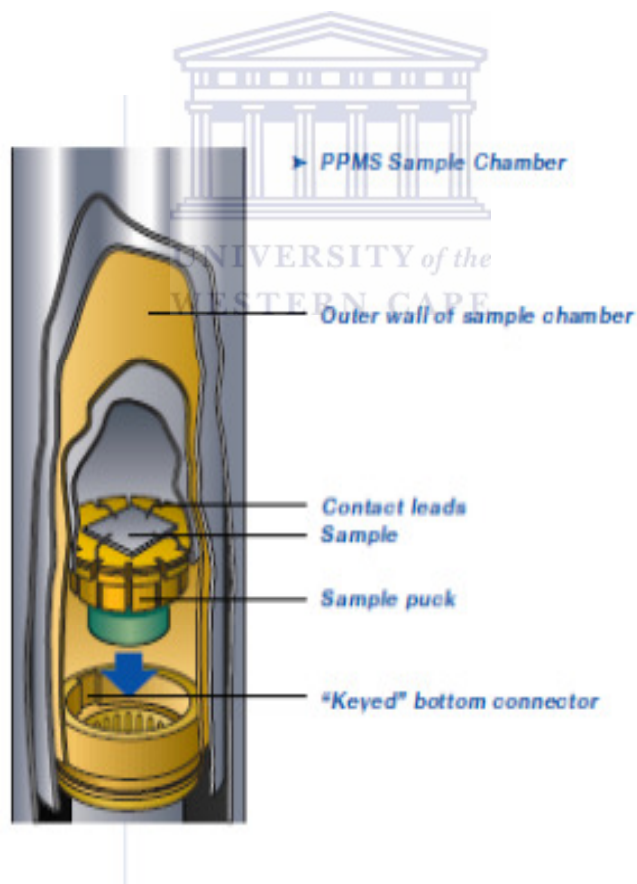


**Figure II-6:** Cross-section of sample puck inside the Physical Property Measurement System (PPMS) sample chamber (PPMS user manual, Quantum design, San Diego).



Resistivity measurements were performed on a bar shaped specimen of a typical dimension  $1 \times 1 \times 6 \text{ mm}^3$  as mentioned in section II-1, using the Physical Properties measurement System (PPMS) at the University of Johannesburg, Department of Physics (FigII-7). Capton tape was



**Figure II-7:** Overview of Physical Property Measurement System (PPMS) at the University of Johannesburg (Physics Department).

placed on the sample puck surface to electrically insulate the sample from the puck and the bar samples were attached to it by G. E varnish (C5 – 101 from Oxford instrument). The G.E. varnish glue was used because of its excellent adhesive properties to well below helium temperature and its good thermal conductivity and electrical insulating properties. A four probe dc method was used for resistivity measurement in the temperature range 1.9 – 300 K. The four contact leads (Fig. II-5) were made from  $50 \mu\text{m}$  gold wire and were attached to the samples with electrically conductive silver paste from Dupont (4922N single

component epoxy which is 70% elemental silver) for brittle samples or spot welded. Current reversal method was used to correct possible thermal voltage in the circuitry. The value of the input current was kept constant throughout the sample due to the high impedance of the voltmeters which eliminate current flow through the voltage leads ( $V^+$  and  $V^-$ ). The measurement of the voltage drop ( $\Delta V$ ) across the specimen is composed of two contributions: the contact potential due to circuitry ( $\Delta V_C$ ) and the sample voltage due to resistivity ( $\Delta V_S$ ).  $\Delta V_S$  is obtained from current reversal method, since  $\Delta V_C$  is independent of the direction of the current. The current reversal method is described as follows: when the current flows from  $\Gamma^+$  to  $\Gamma^-$ , the voltage is taken as  $\Delta V_1$ , then when the current is reversed and flows from  $\Gamma^-$  to  $\Gamma^+$ , the voltage is taken as  $\Delta V_2$ . These leads to:

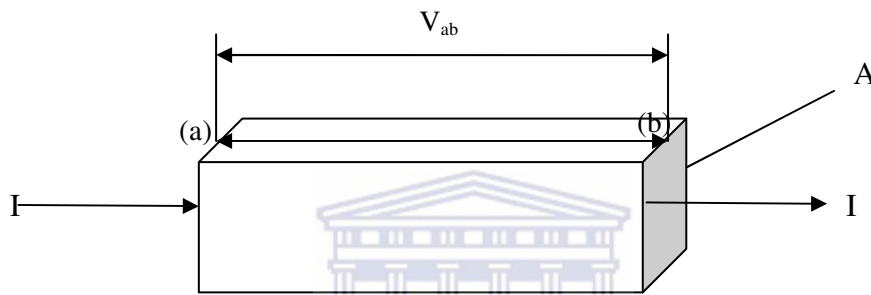


**Figure II-8:** The simple geometry of the sample for the resistivity measurements.

$$\Delta V_1 = \Delta V_C + \Delta V_S$$

$$-\Delta V_2 = \Delta V_C - \Delta V_S$$

$$\Delta V = \left( \frac{\Delta V_2 + \Delta V_1}{2} \right)$$

The value of the input current and the sample geometry during measurement were set to  $I = 4500 \mu\text{A}$ , cross-sectional area,  $A = 1 \text{ mm}^2$  and the length between  $V^+$  and  $V^-$ ,  $L = 1 \text{ mm}$ . The PPMS software uses:  $\Delta V_s = \frac{ILP}{A}$  and  $\Delta V_S = RI$  to calculate the resistivity ( $\rho(T)$ ) and the resistance ( $R(T)$ ). Three independent resistivity and resistance values are taken at each temperature and manually averaged to calculate  $\rho(T)$  and the resistance  $R(T)$ . The actual resistivity of the sample was obtained manually using the average resistance and the measured values of the sample cross-sectional area and length between  $V^+$  and  $V^-$  ( Fig. II-8).

## II-4: Magnetic susceptibility and magnetization measurements

Magnetic susceptibility and magnetization measurement were performed on a single piece of sample with dimensions  $1 \times 1 \times 1 \text{ mm}^3$  (~15 mg mass) of each polycrystalline sample in the temperature range 2–300 K and in fields up to 7 T using a Quantum Design Magnetic Properties Measurement System (MPMS) (Fig. II-10) with Superconducting Quantum Interference Device (SQUID) magnetometer as well as a Cryogen Free Measurement system (CFM) (Fig. II-11). The dimensions of the sample were chosen to be much smaller than the dimensions of the pick-up coils, so that the measured moment is a magnetic dipole (Fig. II-9).

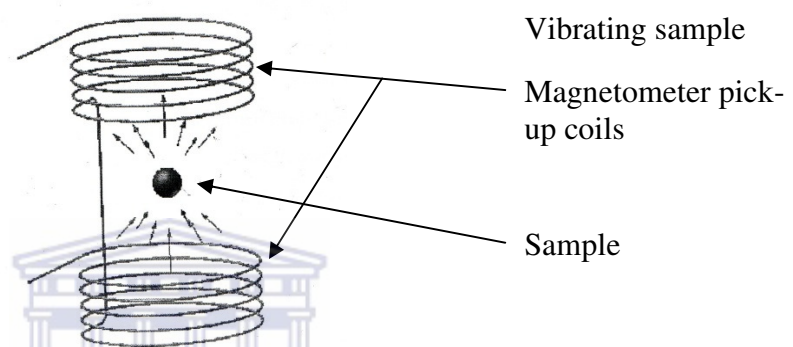


**Figure II-9:** Schematic view of sample and Vibrating Sample Magnetometer (VSM).



**Figure II-10:** Magnetic measurement system (MPMS) XL, configured with optional cryocooled dewar (EverCool™) at the University of Johannesburg, Physics Department (a) Cabinet for EverCool compressor, (b) Computer and cabinet for gas handling and all control electronics, (c) Cabinet for dewar, and (d) EverCooled cold-head.



UNIVERSITY of the  
WESTERN CAPE

**Figure II-11:** Overview of the Cryogen Free Magnet system (CFM) at iThemba LABS, Cape Town.

## Chapter III:

---

### Theoretical overview of CePt<sub>2</sub>Si<sub>2</sub> and CeCu<sub>5</sub>In

The ternary compounds CePt<sub>2</sub>Si<sub>2</sub> and CeCu<sub>5</sub>In are both non-magnetic Kondo lattice compounds, exhibiting similar physical properties with different crystal structures. These compounds have been characterized as heavy-fermion compounds with an enhanced electronic heat capacity coefficient  $\gamma = 70 - 86 \text{ mJ/mol.K}^2$  and  $\gamma = 200 \text{ mJ/mol.K}^2$  for the CePt<sub>2</sub>Si<sub>2</sub> [1, 2, 3] and CeCu<sub>5</sub>In [4] respectively. These compounds have attracted much interest because of the great variety of their ground state properties. Many experimental investigations have been devoted to the thermodynamic and transport properties of these ternary compounds. Doping experiments of these compounds have also received considerable attention. This chapter presents an overview of the studies on CePt<sub>2</sub>Si<sub>2</sub> and CeCu<sub>5</sub>In.

#### III-1 CePt<sub>2</sub>Si<sub>2</sub> compound

The ternary silicides REPt<sub>2</sub>Si<sub>2</sub> where RE are the complete rare earth elements from Y to Lu, were found to be isotropic and crystallize in the tetragonal CaBe<sub>2</sub>Ge<sub>2</sub>-type structure with the space group *P4/nmm* [1, 5, 6, 7]. Transport and thermodynamics properties measurements establish CePt<sub>2</sub>Si<sub>2</sub> as a Kondo lattice compound with the absence of long range magnetic order down to 60 mK [3]. Magnetic properties measurements on GdPt<sub>2</sub>Si<sub>2</sub> and TbPt<sub>2</sub>Si<sub>2</sub> indicate antiferromagnetic ordering at temperatures below 40 K [5], whereas in the case of DyPt<sub>2</sub>Si<sub>2</sub> the onset of ferromagnetism is observed below 4 K [5]. The resistivity studies on polycrystalline CePt<sub>2</sub>Si<sub>2</sub> sample [1] indicate a Kondo-like increase in  $\rho(T)$  upon cooling from room temperature down to a temperature  $T_{\text{max}} = 76 \text{ K}$  corresponding to a resistivity maximum, and followed by a marked decrease towards low temperature. This behaviour of  $\rho(T)$  indicate strong anisotropy which was also observed on  $\rho(T)$  data of the single-crystal CePt<sub>2</sub>Si<sub>2</sub> [8, 9,10]. The low temperature  $\rho(T)$  data of the polycrystalline CePt<sub>2</sub>Si<sub>2</sub> indicate Fermi-liquid behaviour between 4 and 10 K and below 4 K,  $\rho(T)$  tends to a linear temperature dependence [2] characteristic of non-Fermi liquid behaviour. Superconducting transition was not observed down to 1.8 K [5]. Magnetic susceptibility ( $\chi(T)$ ) measurements on polycrystalline [1] and single-crystal CePt<sub>2</sub>Si<sub>2</sub> [3,11] follow the Curie-Weiss relationship at high temperature ( $T \geq 150 \text{ K}$ ) leading to a paramagnetic Curie temperature,  $-\theta_p = 86 \text{ K}$  and with an effective magnetic moment  $\mu_{\text{eff}} = 2.57 \mu_B$  which is close to that expected for the

free  $\text{Ce}^{3+}$ -ion of  $2.54 \mu_B$ .  $\chi(T)$  curve exhibits a broad maximum around 60 K followed by a minimum at 20 K and an increase towards lower temperatures. Inelastic neutron scattering experiment on  $\text{CePt}_2\text{Si}_2$  as interpreted in terms of quasi-elastic scattering suggest that the behaviour of  $\text{CePt}_2\text{Si}_2$  is intermediate between that of valence fluctuation and heavy – Fermion compound [12]. Specific heat,  $C_p(T)$ , studies have been interpreted in the single – impurity model of Rajan [13] with  $J = 1/2$  given a Kondo temperature  $T_K = 70$  K. Studies of  $C_p(T)$  [2, 3] at low temperatures indicate coherence effects, and this behaviour seems to correspond to the non-Fermi liquid behaviour observed in a similar temperature region in the  $\rho(T)$  data. Studies of  $C_p(T)$  also confirm the occurrence of Fermi-liquid behaviour above 15 K. Muon spin resonance ( $\mu\text{SR}$ ) measurements indicate the absence of long-range magnetic order down to 60 mK [3].

The influence of substituting Ce with non-magnetic  $M = \text{La}$  or  $\text{Y}$ , and moment bearing Gd in  $\text{CePt}_2\text{Si}_2$  were reported through  $\rho(T)$ , magnetoresistivity (MR),  $\chi(T)$  and magnetization ( $\sigma(\mu_0H)$ ) measurements on polycrystalline samples of  $(\text{Ce}_{1-x}\text{M}_x)\text{Pt}_2\text{Si}_2$  [14, 15] and  $(\text{Ce}_{1-x}\text{Gd}_x)\text{Pt}_2\text{Si}_2$  [16]. These studies indicate evolution from Coherent Kondo behaviour to incoherent single-ion Kondo behaviour with increased La, Y or Gd concentration.  $\chi(T)$  data indicate antiferromagnetic ordering up to 60% Ce substitution with Gd. The effect of substituting the ligand Si with Ge were also reported through  $\rho(T)$ , MR,  $\chi(T)$  and  $\sigma(\mu_0H)$  measurements on polycrystalline samples  $\text{CePt}_2(\text{Si}_{1-x}\text{Ge}_x)_2$  [17]. It was observed that the Kondo temperature ( $T_K$ ) derived from the magnetoresistivity results decrease with increase Ge substitution and this behaviour was described in terms of the compressible Kondo lattice model [18].

### III-2 CeCu<sub>5</sub>In compound

$\text{CeCu}_6$  is a typical heavy-Fermion compound with a large electronic heat capacity value of  $1530 \text{ mJ/mol.K}^2$  [19, 20, 21]. This compound has attracted many experimental investigations as well as doping experiments. Many studies have been carried out to the transport and thermodynamic properties of this heavy – Fermion compound. One of these investigations was the substitution of Ce with non-magnetic  $M = \text{La}$ ,  $\text{Y}$  or  $\text{Th}$  through measurements on polycrystalline  $(\text{Ce}_{1-x}\text{M}_x)\text{Cu}_6$  alloys [22]. Another group of studies have been reported on the effect of substituting Ce with moment-bearing rare – earth ions  $R = \text{Gd}$  [23, 24],  $\text{Tb}$  [25],  $\text{Nd}$  [23] or  $\text{Pr}$  [22, 26]. Another experimental investigation was the replacement of Cu with the transition element  $M = \text{Au}$ ,  $\text{Ag}$  or  $\text{Pd}$ , which leads to AF ordering for the  $\text{Ce}(\text{Cu}_{6-x}\text{M}_x)$  alloys

above a critical concentration  $x_c$ , where the Rudermann-Kittel-Kasuya-Yosida interaction dominates the Kondo effect [27, 28, 29, 30, 31, 32].

The replacement of one Cu with In to form CeCu<sub>5</sub>In was first reported by Kasaya *et al.* [4]. This compound has the same orthorhombic *Pnma* crystal structure as CeCu<sub>6</sub>. CeCu<sub>5</sub>In is a Kondo lattice compound with a well-defined resistivity peak at 35 K [4]. The resistivity study indicates a  $T^2$  dependence between 0.1 and 4.5 K, characteristic of Fermi-liquid behaviour. The specific heat studies of CeCu<sub>5</sub>In<sub>*x*</sub> is less enhanced at low temperature than that of CeCu<sub>6</sub> as evidenced by a  $\gamma$  value of 200 mJ/mol.K<sup>2</sup> for CeCu<sub>5</sub>In [4] compared to 1530mJ/mol.K<sup>2</sup> for CeCu<sub>6</sub> [19]. No magnetic ordering has been observed for this compound down to 0.1 K [4]. The influence of substituting Cu with In to form CeCu<sub>6-x</sub>In alloy ( $0.5 \leq x \leq 1.6$ ) [4, 33] and have In with M atom (M = Al or Ga) to form CeCu<sub>5</sub>(In<sub>1-x</sub>M<sub>*x*</sub>) [34] has been studied and illustrated Kondo behaviour for these alloy systems.

The effect of replacing Ce with non-magnetic La in the dense Kondo compound CeCu<sub>5</sub>In [35, 36] has been studied through  $\rho(T)$ ,  $\chi(T)$ , MR,  $C_p(T)$  and thermoelectric power (TEP) measurements. A compressible Kondo lattice model [18] has been used to describe the decrease in  $T_K$  and in  $T_{max}$  (temperature at which a maximum in  $\rho(T)$  occurs for the Coherent dense Kondo alloys) with decrease in Ce concentration for these alloys systems. The TEP measurements is positive and exhibits a maximum at approximately 45 K for several investigated compositions in the (Ce<sub>1-x</sub>La<sub>*x*</sub>)Cu<sub>5</sub>In system.

The following two chapters present the effects of substituting Ce with moment-bearing Tb and Dy in CePt<sub>2</sub>Si<sub>2</sub> and moment – bearing Tb in CeCu<sub>5</sub>In.



## References:

---

- 1) D. Gignoux , D. Schmitt, M. Zerguine, C. Ayache and E. Bonjour, *Phys. Lett. A* **117**, 145 (1986).
- 2) C. Ayache, J. Beille, E. Bonjour, R. Calemczuk, G. Creuzet, D. Gignoux, A. Najib, D. Schmitt, J. Voiron and M. Zerguine, *J. Magn. Magn. Mater.* **63/64**, 329 (1987).
- 3) P. Dalmas de Reotier, A. Yaouanc, R. Calemczuk, A. D. Huscley, C. Marcenat, P. Bonville, P. Lejay, P. C. M. Gubbens and A. M. Mulders, *Phys. Rev. B* **55**, 2737 (1997).
- 4) M. Kasaya, N. Satoh, T. Miyazaki and H. Kumazaki, *Physica B* **206 – 207**, 314 (1995).
- 5) K. Hiebl and P. Rogl, *J. Magn. Magn. Mater.* **50**, 39 (1985).
- 6) T. T. M. Palstra, A. A. Menovsky, G. J. Nieuwenhuys and J. A. Mydosh, *J. Magn. Magn. Mater.* **54 – 57**, 435 (1986).
- 7) A. Dommann, F. Hulliger, H. R. Ott and V. Gramlich, *J. Less Common Met.* **110**, 331 (1985).
- 8) R. M. Marsolais, C. Ayache, D. Schmitt, A. K. Bhattacharjee and B. Coqblin, *J. Magn. Magn. Mater.* **76/77**, 269 (1988).
- 9) A. K. Bhattacharjee, B. Coqblin, M. Raki, L. Forro, C. Ayache and D. Schmitt, *J. Physique* **50**, 2781 (1989).
- 10) R. A. Steeman, A. J. Dirkmaat, A. A. Menovsky, E. Frikkee, G. J. Nieuwenhuys and J. A. Mydosh, *Physica B* **163**, 385 (1990).
- 11) D. Gignoux, D. Schmitt and M. Zerguine, *Phys. Rev. B* **37**, 9882 (1988).
- 12) D. Gignoux, D. Schmitt, M. Zerguine and A. P. Murani, *J. Magn. Magn. Mater.* **76/77**, 401 (1988).
- 13) V. T. Rajan, *Phys. Rev. Lett.* **51**, 308 (1983).
- 14) K. Bouziane and P. de V. du Plessis, *J. Phys.: Condens. Matter* **11**, 3161 (1999).



- 15) M. B. Tchoula Tchokonté, P. de V. du Plessis, D. Kaczorowski and A. M. Strydom, *Physica B* **403**, 1350 (2008).
- 16) M. B. Tchoula Tchokonté, P. de V. du Plessis and D. Kaczorowski, *J. Phys.: Condens. Mater.* **15**, 3767 (2003).
- 17) M. B. Tchoula Tchokonté, P. de V. du Plessis, A. M. Strydom and D. Kaczorowski, *J. Magn. Magn. Mater.* **226-230**, 173 (2001).
- 18) M. Lavagna, C. Lacroix and M. Cyrot. *J. Phys. F: Met. Phys.* **12**, 745 (1982).
- 19) H. R. Ott, H. Rudigier, Z. Fisk, J. O. Willis and G. R. Stewart, *Solid State Commun.* **55**, 235 (1985).
- 20) A. Amato, D. Jaccard, E. Walker and J. Flouquet, *Solid State Commun.* **55**, 1131 (1985).
- 21) A. Sumiyama, Y. Oda, H. Nagano, Y. Ōnuki, K. Shibusaki and T. Komatsubara, *J. Phys. Soc. Jpn.* **55**, 1294 (1986).
- 22) J. Kim and G. R. Stewart, *Phys. Rev. B* **49**, 327 (1994).
- 23) A. M. Strydom and P. de V. du Plessis, *J. Phys.: Condens. Matter* **11**, 2285 (1999).
- 24) S. B. Roy, M. R. Lees, G. R. Stewart and B. R. Coles, *Phys. Rev. B* **43**, 8264 (1991).
- 25) E. Bauer, E. Gratz, M. Maikis, H. Kirchmayr S. B. Roy and B. R. Coles, *Physica B* **186-188**, 586 (1993).
- 26) S. Radha, S. B. Roy, A. K. Nigam, S. Ramakrishnan and G. Chandra, *Physica B* **215**, 222 (1995).
- 27) S. B. Roy, G. R. Stewart and B. R. Coles, *J. Magn. Magn. Mater.* **97**, 291 (1991).
- 28) A. Germann, A. K. Nigam, J. Dutzi, A. Schröder and H. v A. Löhneysen, *J. Physique Coll.* **49 C8**, 755 (1988).
- 29) H. G. Schlager, A. Schröder, M. Welsh and H. v A. Löhneysen, *J. Low Temp. Phys.* **90**, 181 (1993).
- 30) T. Pietrus, B. Bogenberger, S. Mock M. Sieck and H. v A. Löhneysen, *Physica B* **206/207**, 317 (1995).

- 31) A. K. Gangopadhyay, J. S. Schilling, E. Schuberth, P. Gutsmedl, F. Gross and K. Andres, *Phys. Rev. B* **38**, 2603 (1988).
- 32) G. Fraunberger, B. Andraka, J. S. Kim, U. Ahlheim and G. R. Stewart, *Phys. Rev. B* **40**, 4735 (1989).
- 33) M. Sieck, C. Speck, M. Waffenschmidt, S. Mock and H. v A. Löhneysen, *Physica B* **223/224**, 325 (1996).
- 34) D. Kaczorowski, M. Kalychaki Ya and V. Zaremba, *Acta Phys. Pol. A* **97**, 189 (2000).
- 35) M. B. Tchoula Tchokonté, D. Kaczorowski, P. de V. du Plessis and A. M. Strydom, *Physica B* **259 – 261**, 22 (1999).
- 36) M. B. Tchoula Tchokonté, P. de V. du Plessis, A. M. Strydom, D. Kaczorowski, A. Czopnik and Z. Kletowski, *J. Phys.: Condens. Matter* **16**, 1981 (2004).



# Chapter IV

---

## Competition between RKKY interaction and the Kondo effect in $(\text{Ce}_{1-x}\text{RE}_x)\text{Pt}_2\text{Si}_2$ , RE = Tb, Dy

The present chapter investigates the competition between the RKKY interaction and the Kondo effect by substituting the Ce-ions with large moment bearing Tb and Dy. These investigations are done through measurements of XRD, electrical resistivity,  $\rho(T)$ , magnetic susceptibility,  $\chi(T)$ , and magnetization,  $\sigma(\mu_0H)$ .

### IV-1 X – ray diffraction

#### IV-1-1 Structural characterisation

The Rietveld analysed diffraction patterns for the  $\text{CePt}_2\text{Si}_2$  and  $\text{REPt}_2\text{Si}_2$  (RE = Tb or Dy) are depicted in Fig. IV-1. The XRD scans analysed through the Rietveld and the Cell and Intensity Least Square (CAILS) – Pawley method using the  $P4/nmm$  space group show that all alloys of the pseudo – ternary systems  $(\text{Ce}_{1-x}\text{RE}_x)\text{Pt}_2\text{Si}_2$  crystallize in the tetragonal  $\text{CaBe}_2\text{Ge}_2$  – type structure. In this space group, RE atoms occupy the crystallographic 2c sites, Pt atoms occupy two different types of sites, Pt1 at the 2c sites and Pt2 at the 2b site, and Si atoms occupy two different sites, Si1 at the 2c site and Si2 at the 2a site. The results obtained from these refinements with observed, calculated and difference plots for the XRD patterns at room temperature of  $\text{CePt}_2\text{Si}_2$  and  $\text{REPt}_2\text{Si}_2$  (RE = Tb or Dy) are shown in Fig. IV-2. The resulting tetragonal crystal structures are depicted in Fig. IV-3 and the atomic coordinates are listed in Table IV-1.

#### IV-1-2 Lattice parameters

Values of the tetragonal lattice parameters  $a$  and  $c$ , and the unit cell volume  $V$  for the two systems are depicted in Fig. IV-3. A linear decrease (solid line) in unit cell volume with increase in RE content  $x$  is observed for the two systems with no appreciable deviation from Vegard's rule [1]. This behaviour suggests that there are no changes in the Ce and Tb or Dy valence as one moves from  $\text{CePt}_2\text{Si}_2$  to  $\text{TbPt}_2\text{Si}_2$  or  $\text{DyPt}_2\text{Si}_2$  as well as no changes in the number of conduction electrons, which insured the metallic bonding of the two systems. The decrease in the tetragonal unit cell volume amounts to a relative change of 4.2 % between

CePt<sub>2</sub>Si<sub>2</sub> and TbPt<sub>2</sub>Si<sub>2</sub> and 4.6 % between CePt<sub>2</sub>Si<sub>2</sub> and DyPt<sub>2</sub>Si<sub>2</sub>. This fast decrease in unit cell volume for the (Ce<sub>1-x</sub>Dy<sub>x</sub>)Pt<sub>2</sub>Si<sub>2</sub> alloy system corroborate with the lanthanide contraction. We also observed a decrease in *a* – and *c* – axes for both systems which amounts to a relative change of 2 % and 0.4 % respectively for the (Ce<sub>1-x</sub>Tb<sub>x</sub>)Pt<sub>2</sub>Si<sub>2</sub> system and 2.3 % and 0.3% respectively for the (Ce<sub>1-x</sub>Dy<sub>x</sub>)Pt<sub>2</sub>Si<sub>2</sub> system. Our results for the CePt<sub>2</sub>Si<sub>2</sub>, TbPt<sub>2</sub>Si<sub>2</sub> and DyPt<sub>2</sub>Si<sub>2</sub> compounds are in good agreement with the lattice parameters reported in references [2, 3, 4].

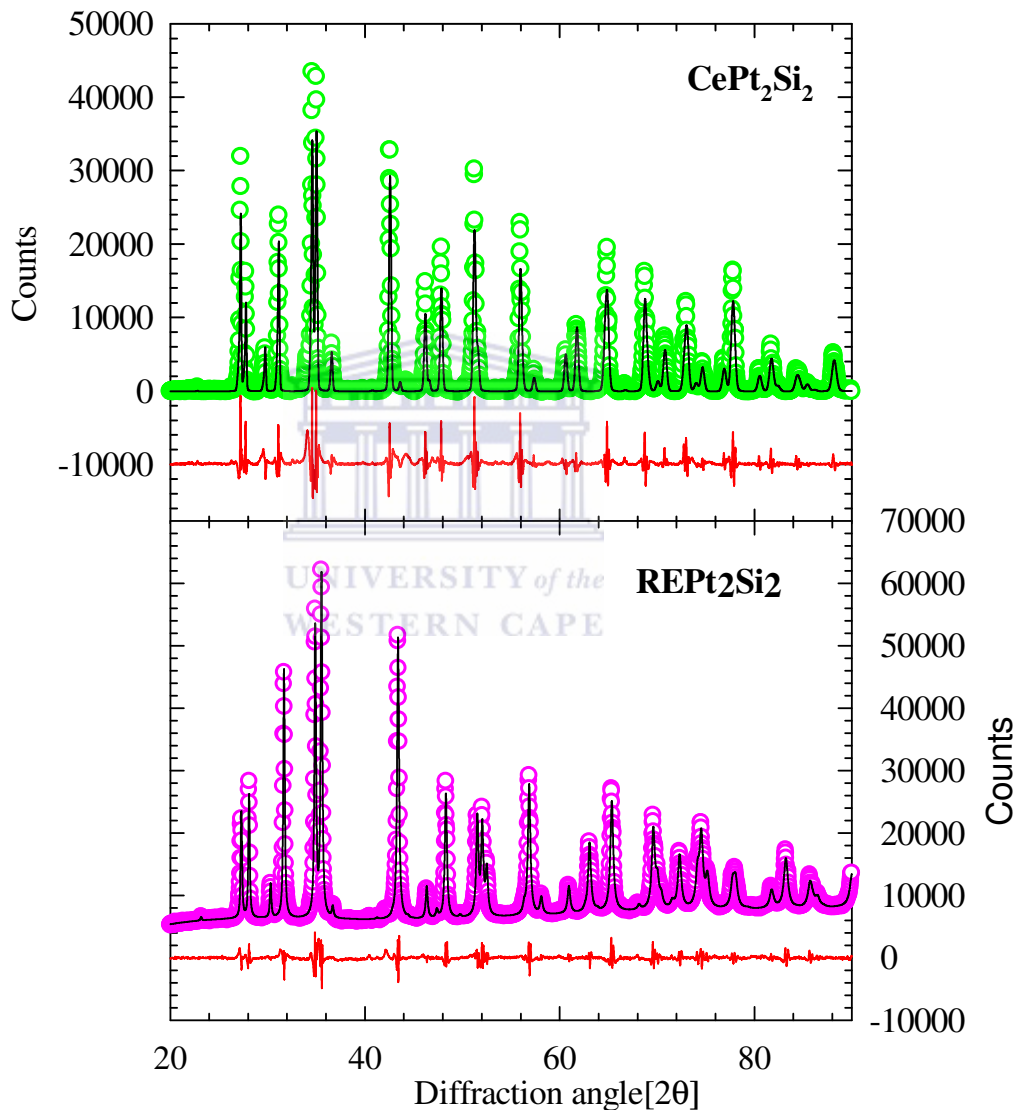


**Figure IV-1:** X – ray diffraction patterns for the CePt<sub>2</sub>Si<sub>2</sub> and REPt<sub>2</sub>Si<sub>2</sub> (RE=Tb or Dy). The open circles are the experimental data. The solid lines through the data points are the results of the Rietveld refinement method and the bottom curves are the difference between the calculated and the experimental data.

**Table IV-1:** Atomic coordinate and occupation factors for  $\text{REPt}_2\text{Si}_2$  (RE = Ce, Tb or Dy) obtained from the Rietveld refinement using the  $P4/nmm$  space group. The occupation factor of all the atoms was kept fixed.

Atom	Wyckoff position	$x$	$y$	$z$	Occupation Factor 100%
RE	2c	0	0.5	0.7511(4)	100
Pt1	2c	0	0.5	0.1256(3)	100
Pt2	2b	0	0	0.5000(1)	100
Si1	2c	0	0.5	0.390(2)	100
Si2	2a	0	0	0	100

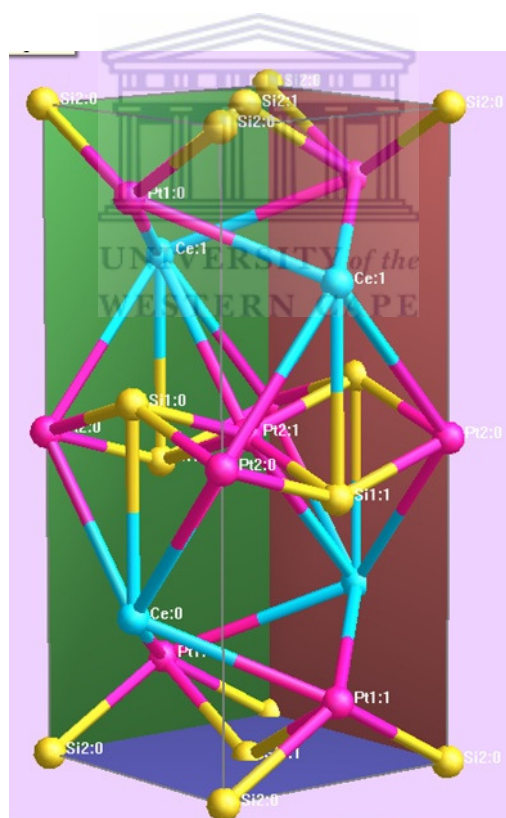


**Figure IV-2:** The tetragonal crystal structure of  $\text{REPt}_2\text{Si}_2$ , (RE = Ce, Tb, Dy). The blue circles represents the RE atoms (Ce for the present picture). The pink and yellow circles represent Pt and Si atoms respectively occupying two different sites, 2c and 2b for Pt and 2c and 2a for Si.

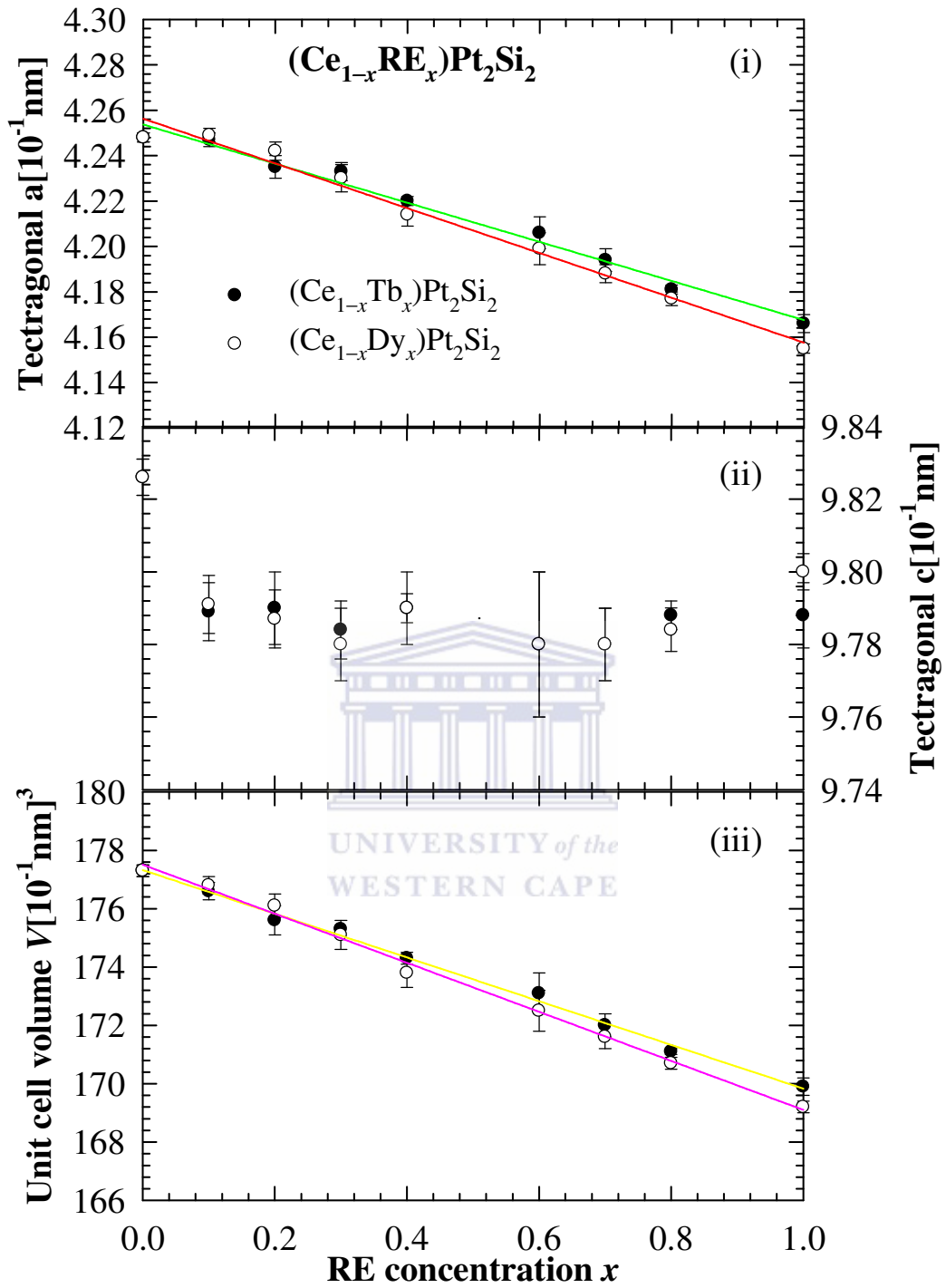


**Figure IV-3:** The tetragonal lattice parameters (i)  $a$  and (ii)  $c$  and the unit cell volume (iii)  $V$  as a function of RE concentration  $x$  for the  $(\text{Ce}_{1-x}\text{RE}_x)\text{Pt}_2\text{Si}_2$  alloy systems with RE = Tb or Dy.

## IV-2 Electrical resistivity

Results of the temperature dependence of the electrical resistivity,  $\rho(T)$  of the two alloy systems  $(\text{Ce}_{1-x}\text{Tb}_x)\text{Pt}_2\text{Si}_2$  and  $(\text{Ce}_{1-x}\text{Dy}_x)\text{Pt}_2\text{Si}_2$  are depicted in Figs. IV-4, IV-5 and IV-6. For the two alloy systems,  $\rho(T)$  shows evolution from coherent Kondo scattering at low temperature for Ce concentrated alloys ( $0 \leq x \leq 0.2$ ) with well-defined Kondo peaks ranging from 62.7 K to 25 K for the  $(\text{Ce}_{1-x}\text{Tb}_x)\text{Pt}_2\text{Si}_2$  system (Figs. IV-4a and IV-6a) to incoherent single-ion Kondo scattering for alloys with  $x \geq 0.3$  (Figs. IV-4b and IV-6b). In the coherent regime  $\rho(T)$  curves show a well-defined Kondo peak ranging from 62.2 to 25 K (Fig. IV-4a) for the  $(\text{Ce}_{1-x}\text{Tb}_x)\text{Pt}_2\text{Si}_2$  system and 62.7 to 37 K (Fig. IV-6a) for the  $(\text{Ce}_{1-x}\text{Dy}_x)\text{Pt}_2\text{Si}_2$  system. The incoherent Kondo scattering is observed at a high temperature for all compositions in the range  $0.3 \leq x \leq 0.9$  as characterized by a  $-\ln(T)$  dependence (see fit of  $\rho(T)$  data to Eq. IV-3 below). The observed resistivity maximum reflects a coherence effect that set in at low temperatures. The decrease in  $T_{\text{max}}$  (temperature of the resistivity maximum) with a decrease in unit cell volume for both alloys systems do not agree with the compressible Kondo lattice model [5]. This suggests that the resistivity maximum is not related to the volume effect. In fact the substitution of Ce with rare earth Gd or Dy increase the number of 4f – electrons in the alloy, which is expected to increase the RKKY interaction, while the reduction in Ce concentration should decrease the strength of the Kondo scattering. Thus  $T_{\text{max}}$  will decrease with decreasing Ce content. Similar behaviour was observed in the resistivity of  $(\text{Ce}_{1-x}\text{Gd}_x)\text{Pt}_2\text{Si}_2$  [6] and  $(\text{Ce}_{1-x}\text{Gd}_x)\text{Cu}_6$  [7, 8].  $\rho(T)$  curve for the  $\text{TbPt}_2\text{Si}_2$  (Fig. IV-4c) and  $\text{DyPt}_2\text{Si}_2$  (Fig. IV-5) show a metallic behaviour with a faint negative  $d\rho/dT$  (downward bending) at intermediate temperatures probably associated with the s – d interband scattering of the conduction electrons which is described by the Mott term  $cT^3$  or crystal – electric field (CEF). The inset of Fig. IV-4c shows the low temperatures  $\rho(T)$  data of the  $\text{TbPt}_2\text{Si}_2$  compound. A drop in  $\rho(T)$  is observed below 8 K as indicated by the arrow, suggesting the occurrence of antiferromagnetic (AF) ordering in this compound at  $T_N = 8$  K. Our measurements of  $\chi(T)$  for the  $(\text{Ce}_{1-x}\text{Tb}_x)\text{Pt}_2\text{Si}_2$  system reported in section IV-3, confirm AF ordering for alloys in the concentration range  $0.7 \leq x \leq 1$ . For the AF ordered alloys with  $x = 0.9$  and  $0.8$  it is observed that the ordering has a small effect on the resistivity and that the magnetic behaviour is dominated by the incoherent Kondo scattering due to the Ce-ions. For the  $\text{DyPt}_2\text{Si}_2$ , no evidence of magnetic ordering was observed from the resistivity results in

our measured temperature range of  $2 \leq T \leq 300$  K.  $\rho(T)$  data for  $\text{TbPt}_2\text{Si}_2$  and  $\text{DyPt}_2\text{Si}_2$  were fitted to Eqs. IV-1 and IV-2 respectively (solid line Figs. IV-4c and IV-5):

$$\rho_{\text{Tb}}(T) = \rho_0 + bT - cT^3 \quad \text{IV-1}$$

$$\rho_{\text{Dy}}(T) = \rho_0 + dT^2 + aT^5 + bT - cT^3 . \quad \text{IV-2}$$

For the Tb compound the least square (LSQ) fits were taken above  $T_N$  and consequently the low temperature phonon contribution ( $bT^5$ ) was omitted in Eq. IV-1. For the Dy compound LSQ fits were taken over the whole temperature range. In Eqs. IV-1 and IV-2,  $\rho_0$  account for lattice imperfections, dislocations and impurities, but may also include the spin-disorder resistivity at high temperatures.  $bT$  and  $aT^5$  are the approximate phonon contribution at high and low temperatures respectively,  $dT^2$  account for ferromagnetic magnons and  $cT^3$  is the Mott term describing the s–d interband scattering of the conduction electrons. LSQ fits give the resistivity parameters listed in Tables IV–2 for the  $\text{TbPt}_2\text{Si}_2$  and  $\text{DyPt}_2\text{Si}_2$  compounds.

**Table IV-2:** The LSQ fits parameters of the temperature dependent resistivity for the  $\text{TbPt}_2\text{Si}_2$  and  $\text{DyPt}_2\text{Si}_2$  compounds.

Compound	$\rho_0$ [ $10^{-8}\Omega\cdot\text{m}$ ]	$a$ [ $10^{-8}\Omega\cdot\text{m}/\text{K}^5$ ]	$b$ [ $10^{-8}\Omega\cdot\text{m}/\text{K}$ ]	$c$ [ $10^{-8}\Omega\cdot\text{m}/\text{K}^3$ ]	$d$ [ $10^{-8}\Omega\cdot\text{m}/\text{K}^2$ ]
$\text{TbPt}_2\text{Si}_2$	194(2)	.....	1.126(1)	$1.47(1)\times 10^{-6}$	.....
$\text{DyPt}_2\text{Si}_2$	12.92(1)	$7.7(8)\times 10^{-5}$	0.0330(7)	$3.2(3)\times 10^{-7}$	$10(1)\times 10^{-13}$

It is observed that for both compounds the Mott term is relatively negligible compared to the high temperature phonon term as well as the low temperature phonon contribution and the ferromagnetic magnon term in the case of the  $\text{DyPt}_2\text{Si}_2$  compound. These negligible contributions will be neglected in the LSQ fits of the other compositions (see Figs. IV–4a, IV-4b, IV-6a and IV-6b).  $\rho(T)$  results for these other compositions at intermediate and higher temperatures are described by Matthiessen’s rule (equation I-18).



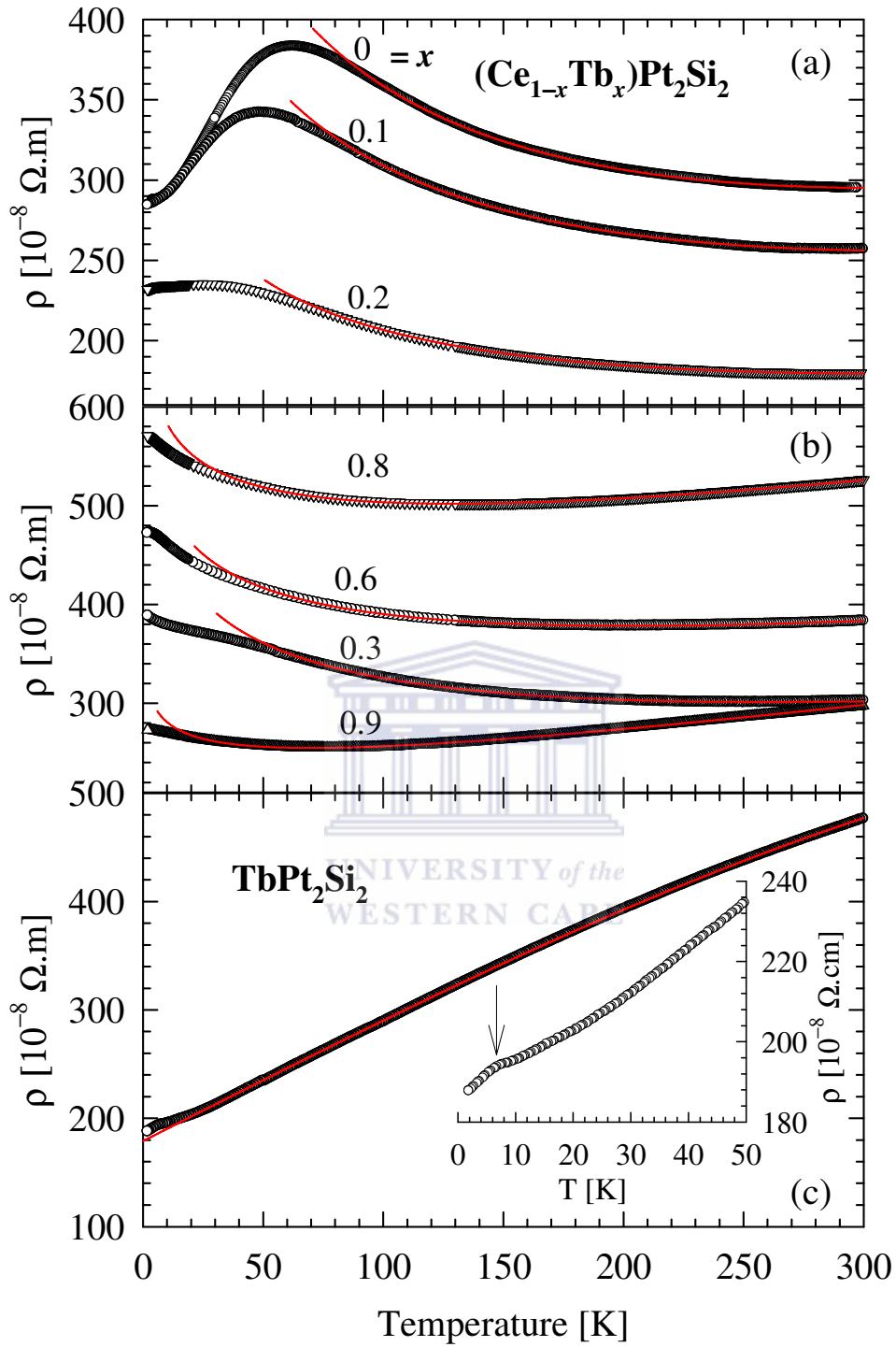


**Figure IV-4:** The temperature dependence of the electrical resistivity,  $\rho(T)$  of the  $(\text{Ce}_{1-x}\text{Tb}_x)\text{Pt}_2\text{Si}_2$  alloy system. The red solid lines through the data points in (a) and (b) are LSQ fits of the measured data to Eq. IV-6 and in (c) to Eq. IV-1.

**Table IV-3:** The LSQ fit parameters of the temperature dependent resistivity  $\rho(T)$  for  $(\text{Ce}_{1-x}\text{Tb}_x)\text{Pt}_2\text{Si}_2$  as well as the observed and calculated (Eq. IV-7) values of the temperature minimum of  $\rho(T)$  and the observed values of the temperature maximum of  $\rho(T)$ .

$x$	0	0.1	0.2	0.3	0.6	0.8	0.9
$\rho'_0 [10^{-8}\Omega.m]$	967	779	460.6	626.7	635	692.9	332.7
$b [10^{-8}\Omega.m/K]$	0.46	0.34	0.19	0.27	0.29	0.34	0.34
$c_k [10^{-8}\Omega.m]$	142.5	109.5	59.2	71.4	59.5	49.5	33.9
$T_{\min}^{calc.} [K]$				264.4	205.2	145.6	99.7
$T_{\min}^{abs} [K]$				256.8	202.0	134.0	78.4
$T_{\max} [K]$	62.2	48.8	25				

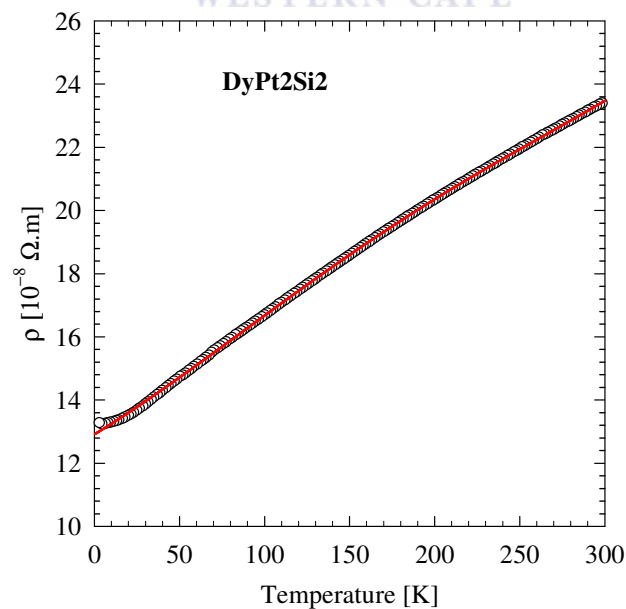


**Figure IV-5:** The temperature dependence of the electrical resistivity,  $\rho(T)$  of the  $\text{DyPt}_2\text{Si}_2$  compound. The red solid line through the data points is the LSQ fits of the measured data to Eq. IV-2.

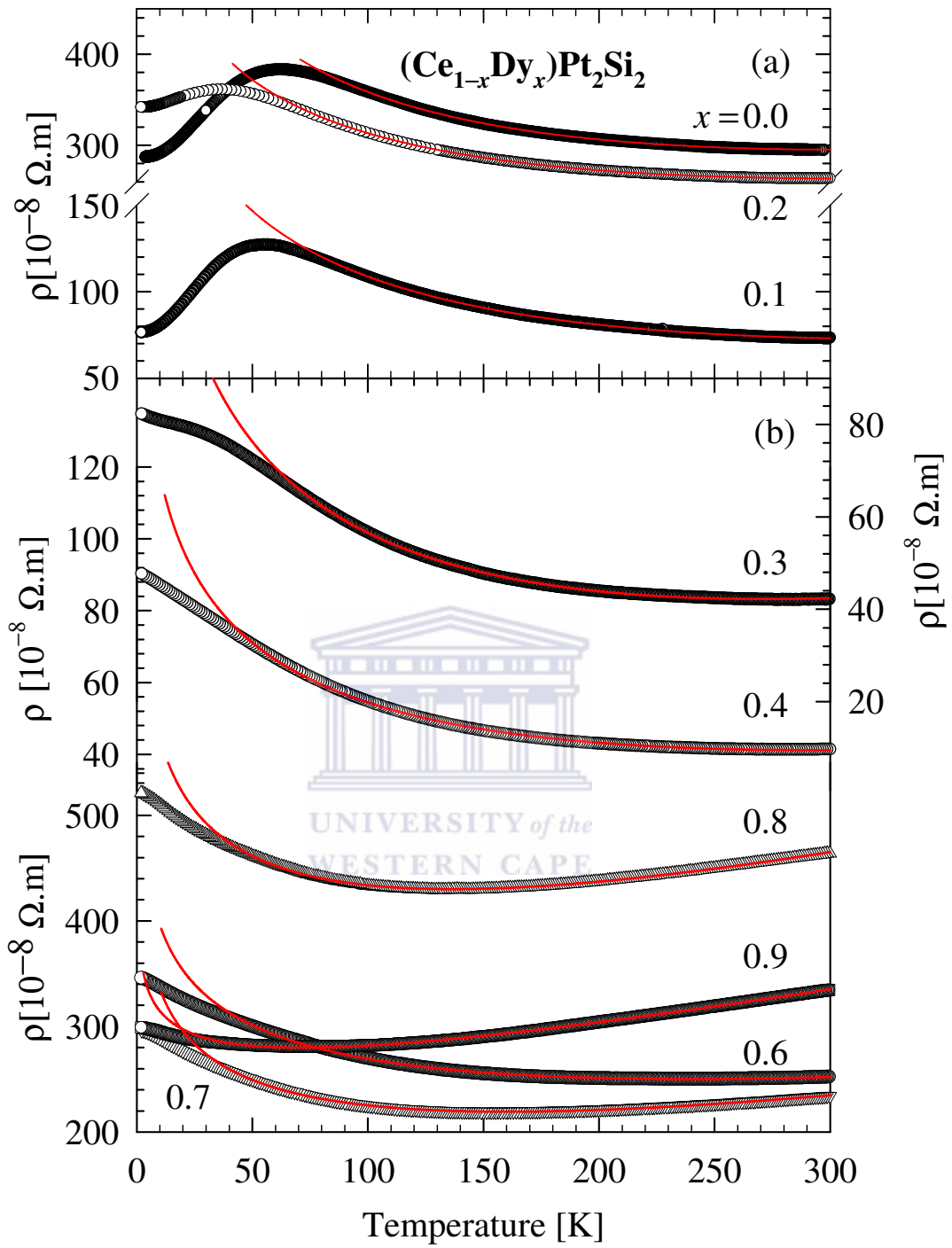


**Figure IV-6:** The temperature dependence of the electrical resistivity,  $\rho(T)$  of the  $(\text{Ce}_{1-x}\text{Dy}_x)\text{Pt}_2\text{Si}_2$  alloy system. The red solid line through the data points in (a) and (b) are LSQ fits of the measured data to Eq. IV-6.

**Table IV-4:** The LSQ fits parameters of the temperature dependent resistivity  $\rho(T)$  for  $(\text{Ce}_{1-x}\text{Dy}_x)\text{Pt}_2\text{Si}_2$  as well as the observed and calculated (Eq. IV-7) values of the temperature minimum of  $\rho(T)$  and the observed values of the temperature maximum of  $\rho(T)$ .

$x$	0	0.1	0.2	0.3	0.4	0.6	0.7	0.8	0.9
$\rho_0[10^{-8}\Omega.\text{m}]$	967	408.6	785	220.7	190.3	545	477.3	764	382.3
$b[10^{-8}\Omega.\text{m}/\text{K}]$	0.46	0.2032	0.3562	0.1419	0.109	0.275	0.396	0.625	0.439
$c_k [10^{-8}\Omega.\text{m}]$	142.5	69.5	110	38.7	31.8	65.7	63.3	85.2	31.3
$T_{\min}^{Cal} [\text{K}]$						238.9	159.8	136.3	71.3
$T_{\min}^{Obs} [\text{K}]$						238.5	153.3	135.6	74.4
$T_{\max} [\text{K}]$	62.7	56.6	37						

The phonon contribution is taken as  $\rho_{ph}(T) \approx bT$ , which is approximately valid in the temperature region in which we fitted our data as is evident from the small values of the Mott term in  $\rho(T)$  curves of  $\text{TbPt}_2\text{Si}_2$  and  $\text{DyPt}_2\text{Si}_2$  compounds.  $\rho_{4f}(T)$  accounts for the Kondo effect given in the form (Eq. I-25):

$$\rho_{4f}(T) = \rho_{spd} \left[ 1 + \alpha N(E_F) J_{sf} \ln\left(\frac{T}{T_K}\right) \right], \quad \text{IV-3}$$

where  $\rho_{spd}$  is the spin-disorder resistivity (Eq. I-23) and the other parameters are defined in chapter I. Using a simplified expression of  $\rho_{4f}(T)$  in the form  $\rho_{4f}(T) = -c_k \ln(T)$ , with  $c_k$  describing the strength of the Kondo scattering, it turns out that the temperature independent  $\rho_0$  account not only for the scattering of conduction electrons by lattice imperfections, dislocations and impurities ( $\rho_0$ ), but may also include a Nordheim-like contribution ( $\rho_N(x)$ ) [9] due to the presence of two kinds of rare – earth ions (Ce and Tb or Ce and Dy), the spin-disorder resistivity ( $\rho_{spd}$ ) as well as the strength of the Kondo interaction ( $-c_k \ln(T_K)$ ):

$$\rho'_0 = \rho_0 + \rho_N(x) + \rho_{\text{spd}} - c_K \ln T_K. \quad \text{IV-4}$$

Hence Eq. I-18 is reduced to:

$$\rho(T) = \rho'_0 + bT - c_K \ln(T). \quad \text{IV-5}$$

The solid lines through the data points in Figs. IV-4a, IV-4b, IV-6a and IV-6b are LSQ fits of the data points to Eq. IV-5 and give the resistivity parameters listed in Table IV-3 and IV-4. It is observed that for the two alloy systems, the phonon contribution is almost constant across the series, while the strength of Kondo interaction  $c_K$  and  $\rho'_0$  decrease almost gradually with decreasing Tb or Dy content  $x$ , indicating the decrease of the Kondo interaction which is expected since the RKKY interaction becomes more important. It is noted that the observed temperature of the resistivity minimum in the incoherent regime and the calculated one resulting Eq. IV-5 (see Tables IV-3 and IV-4):

$$T_{\text{min}}^{\text{cal}} = \frac{b}{c_K}, \quad \text{IV-6}$$

is shifted to lower temperatures with increasing Tb or Dy content  $x$ . It is noted that  $T_{\text{min}}$  may also be expressed as:

$$T_{\text{min}} \propto |\mathfrak{S}_{\text{sf}}|^{3/5}. \quad \text{IV-7}$$

From Eq. V-7 it is evident that the decrease in the value of  $T_{\text{min}}$  corresponds to a decrease of  $\mathfrak{S}_{\text{sf}}$  which indicates the suppression of the Kondo effect in favour of the RKKY interaction.

The resistivity results of the non-magnetic counterpart  $\text{LaPt}_2\text{Si}_2$  are depicted in Fig. IV-7. The  $\rho(T)$  curve shows a distinct kink around 110 K which was also observed in previous studies of this compound [10]. The results reported for this compound in reference [10] shows a marked hysteresis associated with the kink during the cooling and the heating run. Our results do not show such a hysteresis, since our measurements was done in one direction (cooling run). Such a hysteresis associated with the kink was also observed in the resistivity results of ternary  $\text{REInAu}_2$  compounds with  $\text{RE} = \text{La}, \text{Ce}, \text{Pr}$  and  $\text{Nd}$  [11]. These anomalies were ascribed to a phase transition from the high temperature cubic to the low temperature tetragonal structure occurring at a transformation temperature  $T_M$ . The same anomalies were also observed in a number of cubic CsCl-type compounds such as  $\text{LaAg}_{1-x}\text{In}_x$  [12] and

$\text{CeAg}_{1-x}\text{In}_x$  [13]. These two alloy systems crystallize in the cubic CsCl-type structure at room temperature and undergo a martensitic transition to a tetragonal phase at low temperature, which is ascribed to the Jahn–Teller effect [13]. Recent XRD measurements at room and low temperatures on a polycrystalline sample of  $\text{LaPt}_2\text{Si}_2$  reveal the tetragonal  $\text{CaBe}_2\text{Ge}_2$ -type structure at room temperature and undergo a martensitic transformation to the orthorhombic structure at low temperature [14]. The low temperature  $\rho(T)$  curve (inset Fig. IV-7) of  $\text{LaPt}_2\text{Si}_2$  shows a development of superconducting phase transition at  $T_C = 1.9$  K also reported in reference [15] for the same compound.

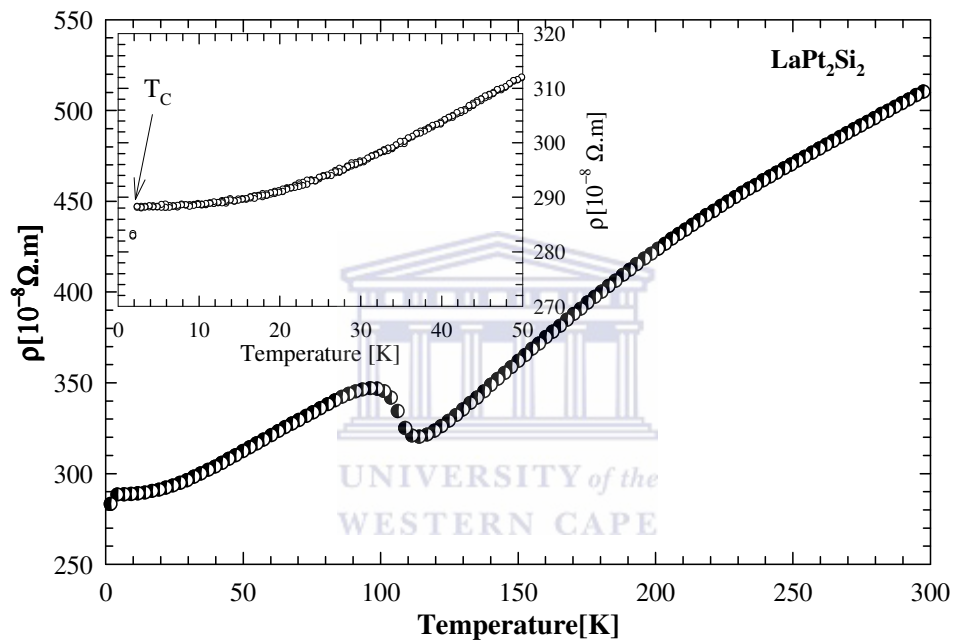


**Figure IV-7:** The temperature dependent resistivity,  $\rho(T)$ , of the non-magnetic counterpart  $\text{LaPt}_2\text{Si}_2$ . The inset illustrates the development of a superconducting transition.

### IV-3 Magnetization and magnetic susceptibility

#### IV-3-1 Magnetization

The fields dependence of the magnetization,  $\sigma(\mu_0H)$ , measured at 1.7 K in field up to 5 T are depicted in Figs. IV–8 and IV-9 for selected compositions of  $(\text{Ce}_{1-x}\text{Tb}_x)\text{Pt}_2\text{Si}_2$  and  $(\text{Ce}_{1-x}\text{Dy}_x)\text{Pt}_2\text{Si}_2$  respectively.  $\sigma(\mu_0H)$  curves for the  $\text{CePt}_2\text{Si}_2$  compound is linear with field up to 5 T. Deviation from linearity and a downward curvature above 1 T is observed with increases in Tb or Dy content  $x$  and more pronounced for the  $(\text{Ce}_{1-x}\text{Dy}_x)\text{Pt}_2\text{Si}_2$  system with a

tendency towards saturation for the maximum applied field of 5 T. Furthermore, the magnitude of  $\sigma(\mu_0H)$  at 5 T increases with increasing Tb or Dy content  $x$ .  $\sigma(\mu_0H)$  curves shows a small hysteresis effect during the process of increasing and decreasing field for some compositions in both systems. No evidence of metamagnetic behaviour is observed for all investigated compositions in both systems.

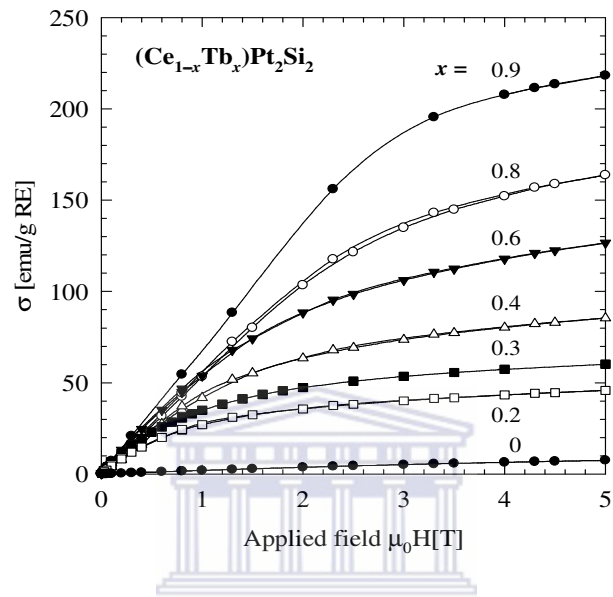


**Figure IV-8:** The field variation of the magnetization at 1.7 K for  $(\text{Ce}_{1-x}\text{Tb}_x)\text{Pt}_2\text{Si}_2$  alloys measured with increasing and decreasing field.

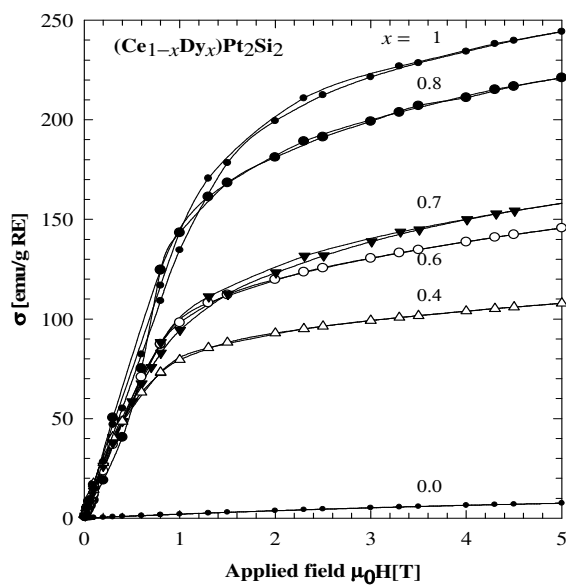


**Figure IV-9:** The field variation of the magnetization at 1.7 K for  $(\text{Ce}_{1-x}\text{Dy}_x)\text{Pt}_2\text{Si}_2$  alloys measured with increasing and decreasing field.

### IV-3-2 Magnetic susceptibility

The temperature dependence of the inverse magnetic susceptibility,  $\chi^{-1}(T)$ , of the alloy systems  $(\text{Ce}_{1-x}\text{Tb}_x)\text{Pt}_2\text{Si}_2$  and  $(\text{Ce}_{1-x}\text{Dy}_x)\text{Pt}_2\text{Si}_2$  with  $0 \leq x \leq 1$ , measured in a field of 0.1 T in the temperature range 1.7 – 400 K are depicted in Figs. IV-10 and IV-11 respectively. The applied field of 0.1 T was chosen since for all the compositions in the two systems, the  $\sigma(\mu_0H)$  curves are linear in this field (see Figs. IV-8 and IV-9). Above 150 K as shown by the solid line fits, the reciprocal susceptibility follows a Curie–Weiss (CW) relationship:

$$\chi^{-1}(T) = \frac{3k_B(T - \theta_p)}{N_A\mu_{\text{eff}}^2} \quad \text{IV-8}$$

where  $k_B$  is the Boltzmann's constant,  $N_A$  is the Avogadro number,  $\theta_p$  is the asymptotic paramagnetic Curie temperature and  $\mu_{\text{eff}}$  is the effective magnetic moment. Deviation from the CW relationship at low temperatures is due to the onset of magnetic ordering or crystal electric field effect. Values of  $\mu_{\text{eff}}$  and  $\theta_p$  obtained from LSQ fits of the measured data to Eq. V-8 are listed in Table IV-5 and IV-6.  $\mu_{\text{eff}}$  values obtained from the  $\text{CePt}_2\text{Si}_2$ ,  $\text{TbPt}_2\text{Si}_2$  and  $\text{DyPt}_2\text{Si}_2$  are in good agreement with the expected free – ion values of  $2.54 \mu_B$  for the  $\text{Ce}^{3+}$  -ion,  $9.72 \mu_B$  for the  $\text{Tb}^{3+}$  -ion and  $10.70 \mu_B$  for the  $\text{Dy}^{3+}$  -ion. A gradual increase in the observed  $\mu_{\text{eff}}$  values is evident between  $\text{CePt}_2\text{Si}_2$  and  $\text{REPt}_2\text{Si}_2$  (RE = Tb or Dy) suggesting that at high temperature the Ce and Tb or Dy atoms contribute independently to the total moment. We calculated the moment (chapter I, Eq. I-4) expected for each composition based on the assumption of independent contribution of the Ce and Tb or Dy atoms to the total moment. It is seen in Tables IV–5 and IV-6 that the calculated and the observed  $\mu_{\text{eff}}$  values are in reasonable agreement for both systems. A similar behaviour was found in  $(\text{Ce}_{1-x}\text{Gd}_x)\text{Pt}_2\text{Si}_2$  [6],  $(\text{Ce}_{1-x}\text{Gd}_x)\text{Cu}_6$  [7] and  $(\text{Ce}_{1-x}\text{RE}_x)\text{In}_3$  (RE = Gd, Tb and Dy) [16] alloys systems. The low temperature zero – field cooled (ZFC) and field cooled (FC)  $\chi(T)$  data are depicted in Fig. IV-12 for the  $(\text{Ce}_{1-x}\text{Tb}_x)\text{Pt}_2\text{Si}_2$  system with  $x = 1, 0.8$  and  $0.6$ . It is observed that the ZFC and FC  $\chi(T)$  results taken in a field of 0.1 T bifurcate below  $T_b = 15.9$  K, 11 K and 4.5 K for the  $x = 1, 0.8$  and  $0.6$  alloy respectively. These bifurcation temperatures  $T_b$  appear well above their respective Néel temperature  $T_N$  (see below, Fig. IV-12). We also observed that this bifurcation disappears for alloy compositions in the range  $0 \leq x \leq 0.4$ . Furthermore, the ZFC and FC  $\chi(T)$  data taken in a field of 1 T show no bifurcation for alloys with  $x = 1, 0.8$  and  $0.6$ . It should be noted that the splitting between the ZFC and FC  $\chi(T)$



curves suggest a complex magnetic behaviour such as canted antiferromagnetic (AF) behaviour. The top inset of Fig. IV-12 displays the low temperature FC  $\chi(T)$  data in a field of 0.1 T for compositions showing magnetic order. The arrows at the kink are associated with AF phase transition temperature  $T_N$ . These  $T_N$  values are listed in Table IV-4 and plotted as a function of Ce content  $(1-x)$  (bottom inset Fig.IV-12). Our result of  $T_N$  for the  $\text{TbPt}_2\text{Si}_2$  is slightly higher compared to 6.5 K reported in reference [4]. The low temperature  $\chi(T)$  data for the  $(\text{Ce}_{1-x}\text{Dy}_x)\text{Pt}_2\text{Si}_2$  alloy system are depicted in Fig.IV-13.  $\chi(T)$  data for all compositions shows no magnetic phase transition in our measured temperature range.



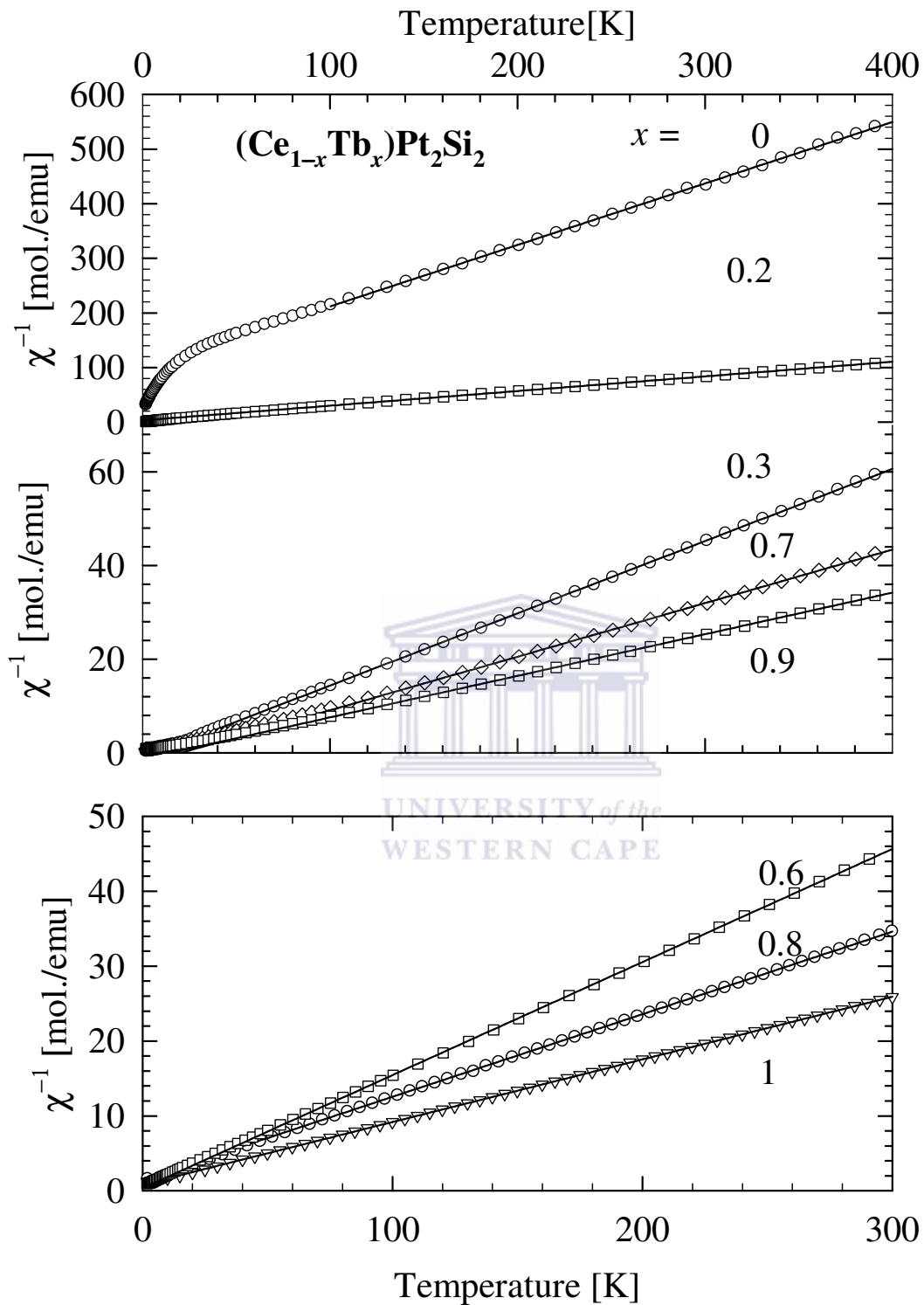


**Figure IV-10:** Temperature variation of the inverse susceptibility  $\chi^{-1}(T)$  for  $(\text{Ce}_{1-x}\text{Tb}_x)\text{Pt}_2\text{Si}_2$ .

The data refer to a mole of rare-earth atoms. The solid lines through the data points represent LSQ fits of the measured data to a Curie-Weiss relationship (Eq. IV-8).

**Table IV–5:** Magnetic susceptibility data for the  $(\text{Ce}_{1-x}\text{Tb}_x)\text{Pt}_2\text{Si}_2$ . The effective magnetic moment  $\mu_{\text{eff}}$  as well as the paramagnetic Curie temperature  $\theta_P$  was obtained from LSQ fits of the experimental data in Fig. IV-10 to the Curie – Weiss relationship (Eq. IV-8). Values of  $T_N$  were inferred from the position of the maxima in the  $\chi(T)$  curves in the inset of Fig. IV-12. Values of  $\mu_{\text{eff}}$  Calculated for the alloys as described in the text are also included for comparison.

$x$	0	0.2	0.3	0.4	0.6	0.7	0.8	0.9	1
$\theta_P$ [K]	–85(2)	–14.9(2)	9.4(2)	–3.5(6)	0.7(4)	22.3(6)	8.9(5)	17.1(7)	–9.5(5)
$\mu_{\text{eff}}(\text{Exp})[\mu_B]$	2.66	4.92	6.00	6.27	7.23	8.34	8.79	9.45	9.77
$\mu_{\text{eff}}(\text{cal})[\mu_B]$	2.54	3.98	4.69	5.41	6.85	7.57	8.28	9.00	9.72
$T_N$ [K]						3.4	5.0	6.0	8.0

**Table IV–6:** Magnetic susceptibility data for the  $(\text{Ce}_{1-x}\text{Dy}_x)\text{Pt}_2\text{Si}_2$ . The effective magnetic moment  $\mu_{\text{eff}}$  as well as the paramagnetic Curie temperature  $\theta_P$  was obtained from LSQ fits of the experimental data in Fig. IV-11 to the Curie – Weiss relationship (Eq. IV-8). Value of  $\mu_{\text{eff}}$  Calculated for the alloys as described in the text are also included for comparison.

$x$	0	0.2	0.4	0.6	0.8	1
$\theta_P$ [K]	–85(2)	6.8(2)	14.3(5)	–18.0(2)	–6.9(4)	9(1)
$\mu_{\text{eff}}(\text{Exp.})[\mu_B]$	2.66	4.79	6.94	7.88	7.92	10.70
$\mu_{\text{eff}}(\text{Cal.})[\mu_B]$	2.54	4.16	5.78	7.39	9.01	10.63

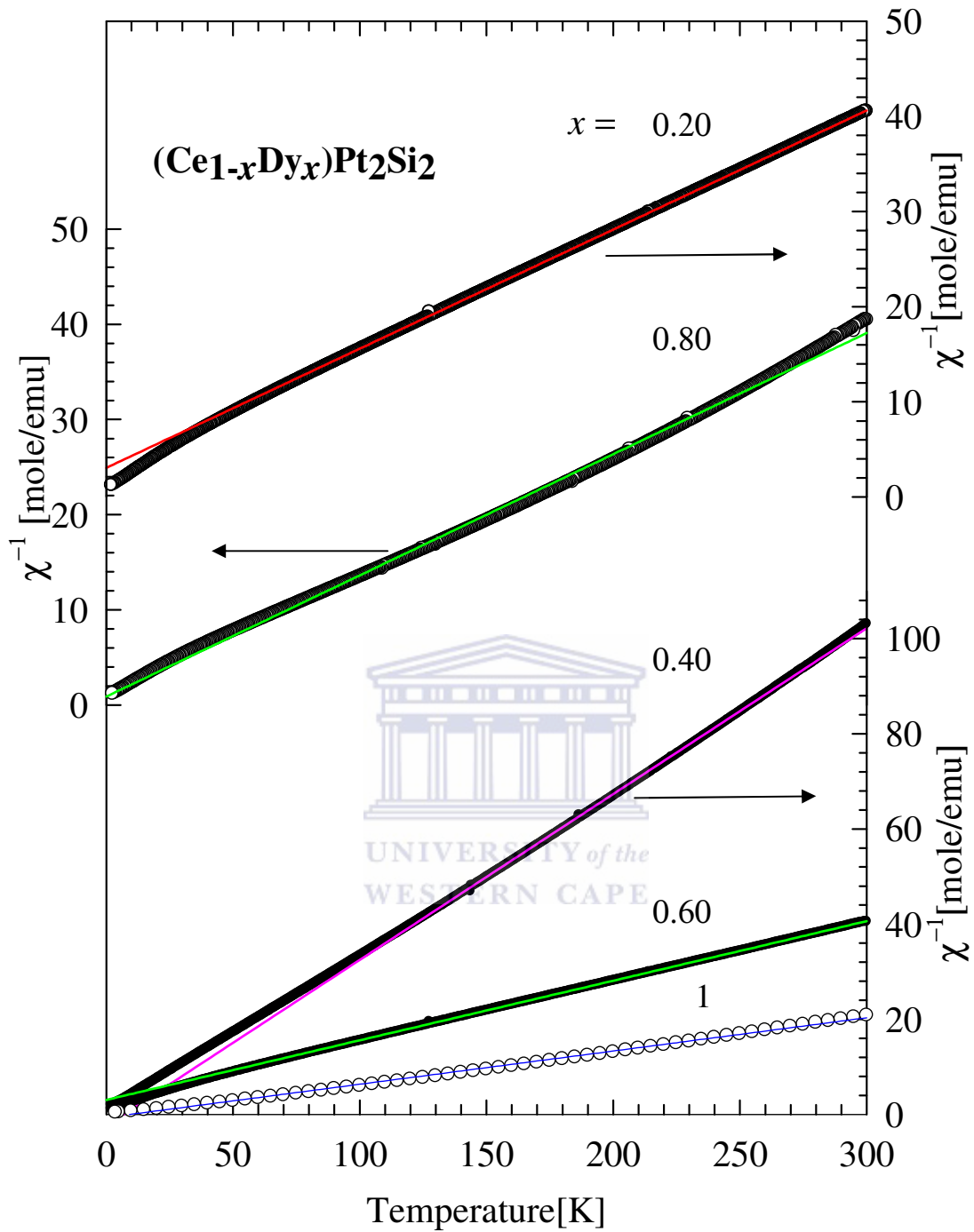


**Figure IV-11:** Temperature variation of the inverse susceptibility  $\chi^{-1}(T)$  for  $(\text{Ce}_{1-x}\text{Dy}_x)\text{Pt}_2\text{Si}_2$ . The data refer to a mole of rare-earth atoms. The solid lines through the data points represent LSQ fits of the measured data to a Curie-Weiss relationship (Eq. IV-8).

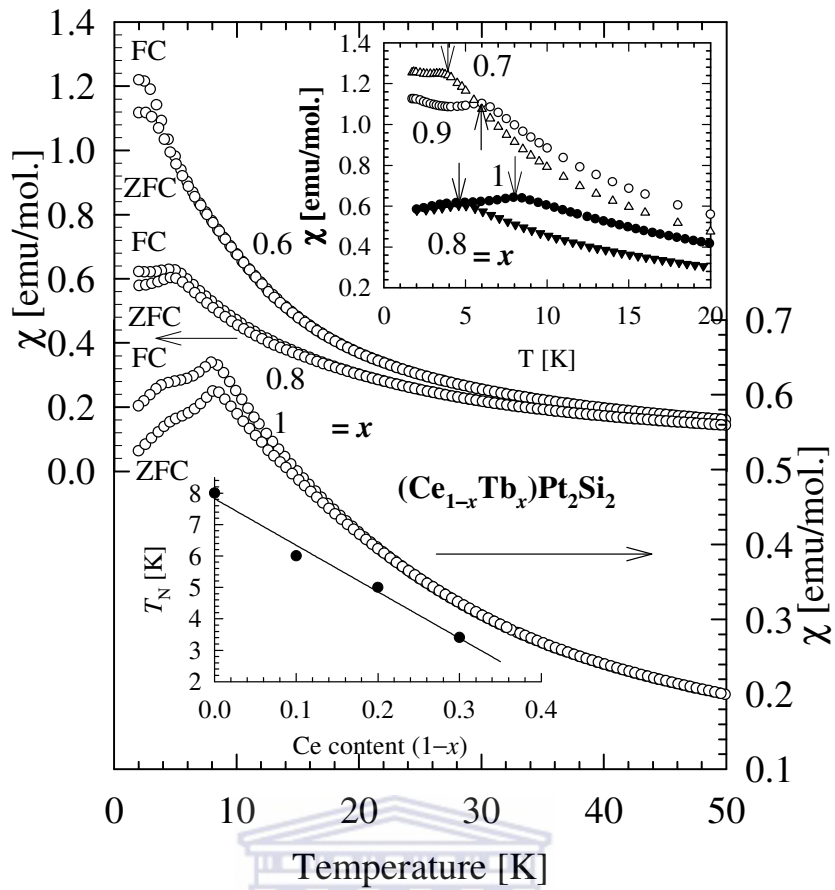


**Figure IV-12:** The low temperature ZFC and FC  $\chi(T)$  data for the  $(\text{Ce}_{1-x}\text{Tb}_x)\text{Pt}_2\text{Si}_2$  alloy system with  $x = 1, 0.8$  and  $0.6$ . The top inset displays the low temperature FC  $\chi(T)$  data in a field of 0.1 T for compositions showing magnetic order and the bottom inset shows the variation of  $T_N$  as a function of Ce content. The arrows at the top inset indicate the magnetic phase transition temperature.

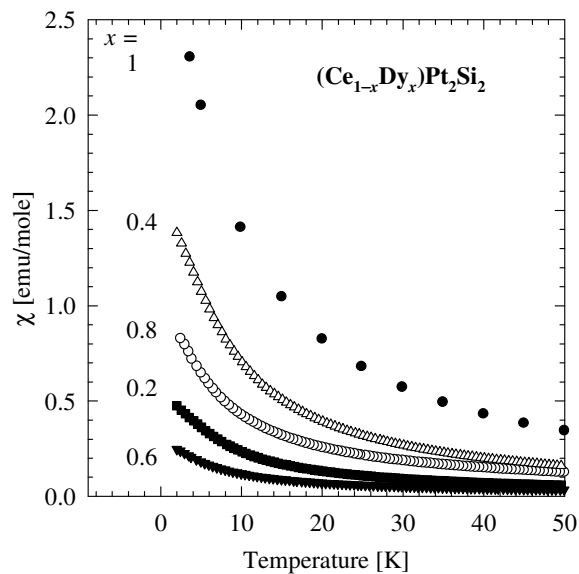


**Figure IV-13:** The low temperature variation of magnetic susceptibility  $\chi(T)$  for the  $(\text{Ce}_{1-x}\text{Dy}_x)\text{Pt}_2\text{Si}_2$  alloy system.

#### IV-4 Conclusion

The study of  $(\text{Ce}_{1-x}\text{RE}_x)\text{Pt}_2\text{Si}_2$  (RE = Tb or Dy) alloy systems indicate evolution from a coherent Kondo lattice behaviour for the Ce concentrated alloys ( $x \leq 0.2$ ) to a dominantly single-ion Kondo scattering ( $0.3 \leq x \leq 0.9$ ). Metallic behaviour is observed for both  $\text{TbPt}_2\text{Si}_2$  and  $\text{DyPt}_2\text{Si}_2$  compounds. Alloys with  $x \geq 0.7$  in  $(\text{Ce}_{1-x}\text{Tb}_x)\text{Pt}_2\text{Si}_2$  system exhibit antiferromagnetism. No evidence of magnetic order was observed for the  $(\text{Ce}_{1-x}\text{Dy}_x)\text{Pt}_2\text{Si}_2$  system as well as metamagnetic behaviour for both systems. A remarkable feature of the two systems is the robustness of the Kondo properties against large moment – bearing substitutions of Tb - and Dy – ions on the Ce site.



## References:

---

- 1) L. Vegard, *Z. Phys.* **5**, 17 (1927); *Z. Krist.* **67**, 239 (1928).
- 2) C. Ayache, J. Beille, E. Bonjour, R. Calemczuk, G. Creuzet, D. Gignoux, A. Najib D. Schmitt J. Voiron and M. Zerguine, *J. Magn. Magn. Mater.* **63 / 64**, 329 (1987).
- 3) D. Rossi, R. Marazza and R. Ferro, *J. Less – Common Met.* **66**, 17 (1979).
- 4) K. Hielb and P. Rogl, *J. Magn. Magn. Mater.* **50**, 39 (1985).
- 5) M. Lavagna, C. Lacroix and M. Cyrot, *J. Phys. F: Met. Phys.* **13**, 1007 (1983).
- 6) M. B. Tchoula Tchokonte, P. de V. du Plessis and D. Kaczorowski, *J. Phys.: Condens. Matter.*, **15**, 3767 (2003).
- 7) S. B. Roy, M. R. Lees G. R. Stewart and b. R. Coles, *Phys. Rev.* **B 43**, 8264 (1991).
- 8) E. Bauer, E. Gratz, M. Maikis, H. Kirchmayr, S. Roy and B. R Coles, *Physics* **B 186 – 188**, 586 (1993).
- 9) F. J. Blatt, *Physics of Electronic Conduction in Solids*, (New York, McGraw – Hill) (1968).
- 10) F. C. Ragel and P. de V. du Plessis., *J. Phys: Condens. Matter.*, **20**, 05521 (2008).
- 11) M. J. Besnus, J. P. Kappler, A. Meyer, J. Sereni, E. Siaud, R. Lahiouel and J. Pierre, *Physica* **B 130**, 240 (1985).
- 12) H. Balster, H. Ihrig, A. Kockel and S. Methfessel, *Z. Phys.* **B 21**, 241 (1975)
- 13) E. Gratz and M. J. Zuckermann, *Handbook on the Physics and Chemistry of Rare Earths*, **vol. 5**, ed K. A. Gschneidner Jr and L. Eyring (Amsterdam: Elsevier) p 117 and references therein.
- 14) H. Nagano, N. Aroaka, A. Mitsuda, H. Wada, M. Ichihara, M. Isobe, and Y. Ueda, *ICM2012 Proceeding*.
- 15) R. N. Shelton, H. F. Braun and E. Musick, *Solid State Commun.* **52**, 797 (1984).
- 16) M. B. Tchoula Tchokonte, K. G. Tshabalala P. de V. du Plessis and D. Kaczorowski, *J. Phys. Chem. of Solids.*, **71**, 181 (2010).

## Chapter V:

---

### Kondo behaviour in $(\text{Ce}_{1-x}\text{Tb}_x)\text{Cu}_5\text{In}$

The present chapter investigates Kondo behaviour in  $(\text{Ce}_{1-x}\text{Tb}_x)\text{Cu}_5\text{In}$  by illustrating the evolution from coherent Kondo lattice behaviour to incoherent single – ion Kondo scattering with increasing Tb concentration. This evolution is clearly observed from the resistivity results.

#### V-1 X – ray diffraction

##### V-1-1 Structural characterisation

The room temperature X-ray powder diffraction patterns indicates an orthorhombic  $\text{CeCu}_6$ -type structure with space group  $Pnma$  up to 40% Ce substitution for the  $(\text{Ce}_{1-x}\text{Tb}_x)\text{Cu}_5\text{In}$  alloy series. For compositions above  $x > 0.4$ , XRD patterns indicates a phase change as evident in Fig.V-1. Thus, the orthorhombic region of the  $(\text{Ce}_{1-x}\text{Tb}_x)\text{Cu}_5\text{In}$  alloy series that is amenable for study, only extends up to  $x = 0.4$ . XRD patterns for compositions in the range  $0 \leq x \leq 0.4$  could be successfully refined by the Rietveld and CAILS – Pawley method using the space group  $Pnma$ . The final results from the Rietveld refinements with observed, calculated and difference plots for XRD pattern of  $\text{CeCu}_5\text{In}$  at room temperature are shown in Fig.V-1(i). The atomic coordinate's results, from this analysis are given in Table V-1 and the orthorhombic crystal structure in Fig.V-2.

##### V-1-2 Lattice parameters

The orthorhombic lattice parameters  $a$ ,  $b$  and  $c$  and the unit cell volume  $V$  for the  $(\text{Ce}_{1-x}\text{Tb}_x)\text{Cu}_5\text{In}$  alloys series are depicted in Fig.V-3. A linear decrease in lattice parameters  $a$  and  $b$  and the unit cell volume  $V$  is observed in our investigated concentration range of  $0 \leq x \leq 0.4$ , indicating the validity of Vegard's rule [1]. This linear behaviour suggest that there is no sudden change in Ce and Tb valence as well as the number of conduction electrons which ensure a metallic bonding in the system as one moves from  $\text{CeCu}_5\text{In}$  to  $(\text{Ce}_{0.6}\text{Tb}_{0.4})\text{Cu}_5\text{In}$ . The decrease in the  $a$ -,  $b$ - and  $c$  – axes and the unit cell volume  $V$  amount to a relative change of 0.6 %; 0.6 %; 0.85%; and 2.0% respectively between  $\text{CeCu}_5\text{In}$  and  $(\text{Ce}_{0.6}\text{Tb}_{0.4})\text{Cu}_5\text{In}$  in accordance with the lanthanide contraction.



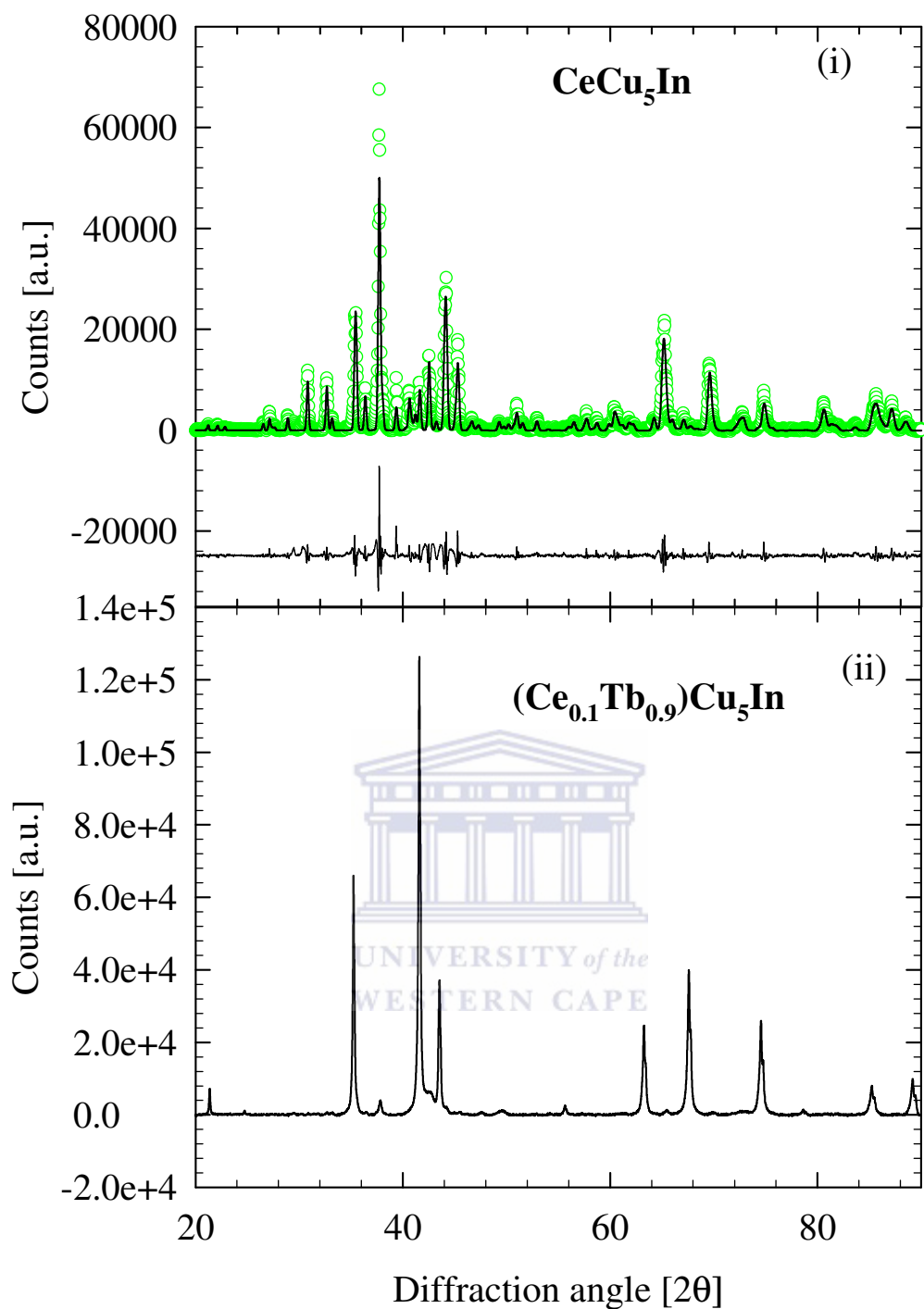


**Figure V-1:** X-ray diffraction pattern for the polycrystalline specimen  $\text{CeCu}_5\text{In}$  (i) and  $(\text{Ce}_{0.1}\text{Tb}_{0.9})\text{Cu}_5\text{In}$  (ii) showing a phase change. The top figure (i) shows the Rietveld refinement method. The open circles are the experimental data. The solid lines through the data points are the results of the Rietveld refinement and the bottom curves are the difference between the calculated and the experimental data.

**Table V-1:** Atomic coordinate and occupation factors for CeCu<sub>5</sub>In obtained from the Rietveld refinement method using the *Pnma* space group. The occupation factor of all the atoms was kept fixed.

Atom	Wyckoff position	<i>x</i>	<i>y</i>	<i>z</i>	Occupation Factor 100%
Ce	<i>4c</i>	0.763(1)	1/4	0.9402(8)	100
Cu1	<i>8d</i>	0.065(1)	0.488(2)	0.312(1)	100
Cu2	<i>4c</i>	0.565(1)	0.169(1)	0.401(1)	100
In1	<i>4c</i>	0.652(1)	1/4	0.6277(8)	100
In2	<i>4c</i>	0.823(1)	1/4	0.2616(8)	100
In3	<i>4c</i>	0.913(1)	1/4	0.490(1)	100

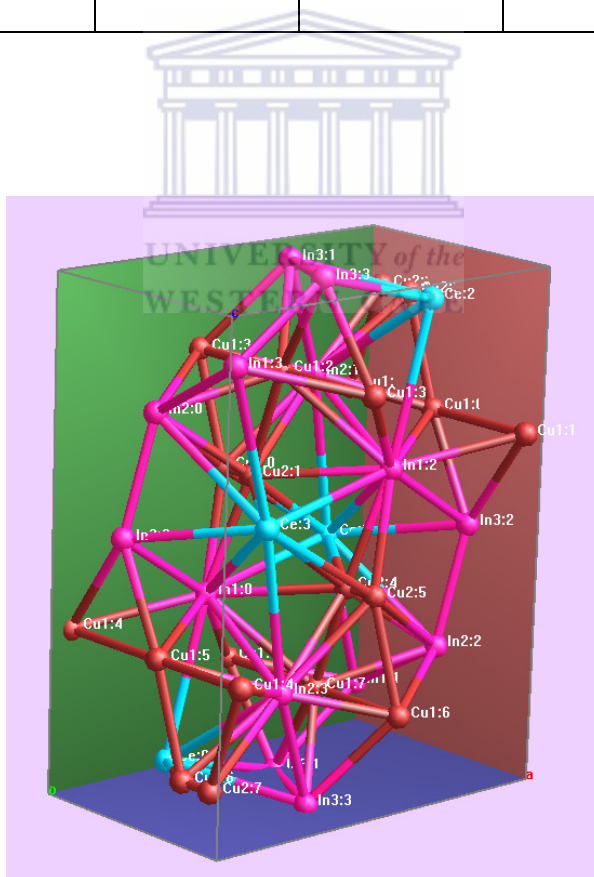


**Figure V –2:** The orthorhombic crystal structure of CeCu<sub>5</sub>In. The blue circles represent the Ce atom. The brown circles represent Cu atoms occupying two different sites, *8d* and *4c* and the pink circles represent In atoms.

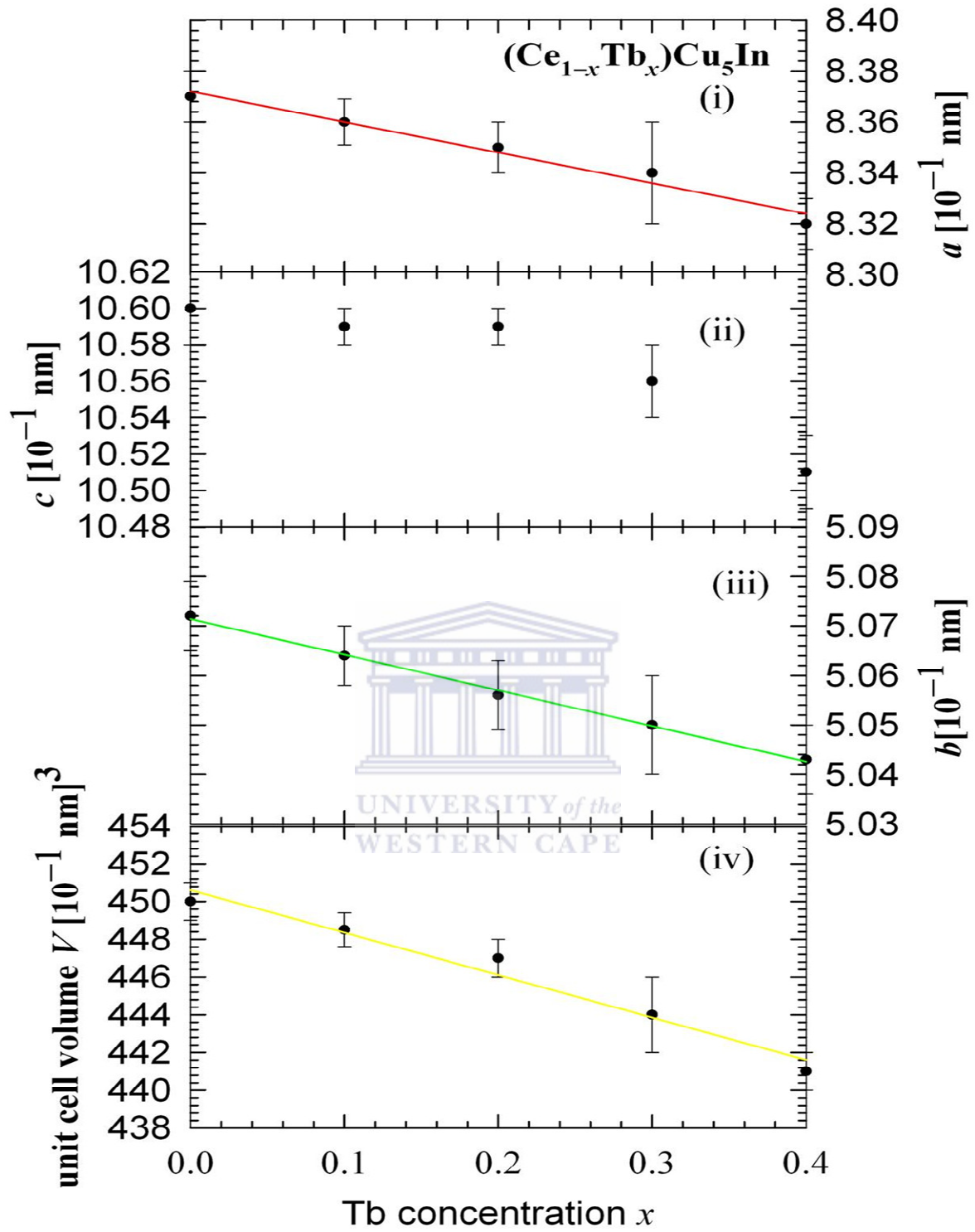


**Figure V-3:** The orthorhombic lattice parameters  $a$  (i),  $b$  (ii) and  $c$  (iii) and the unit cell volume  $V$  (iv) as a function of Tb concentration  $x$  for the  $(\text{Ce}_{1-x}\text{Tb}_x)\text{Cu}_5\text{In}$  ( $0 \leq x \leq 0.4$ ) alloy system.

## V-2: Electrical Resistivity

The temperature dependence of the room temperature normalized electrical resistivity  $\rho(T)/\rho_{300K}$  for the  $(Ce_{1-x}Tb_x)Cu_5In$  are depicted in Fig. V-4 in the coherent (top Fig. V-4) and incoherent region (middle Fig.V-4) together with the total resistivity of the non-magnetic counterpart  $LaCu_5In$  (phonon contribution: bottom Fig.V-4). Similar to the  $(Ce_{1-x}RE_x)Pt_2Si_2$  alloy systems it is observed that  $\rho(T)$  data show evolution from coherent Kondo lattice behaviour at concentrated Ce alloys ( $0 \leq x \leq 2$ ) with a well-defined Kondo peak ranging from 32 K to 20 K (Fig. V-4(i)) to incoherent single-ion Kondo scattering with increasing Tb content  $x$  up to  $x = 0.4$  (Fig V-4 (ii)).  $\rho(T)$  of  $LaCu_5In$  shows normal metallic behaviour with a negative  $d\rho/dT$  at higher temperature (departure from the Bloch – Grüneissen relationship) originating from the  $s - d$  interband scattering of the conduction electron described by the Mott term  $-cT^3$ . The solid line through the data points of the total resistivity of the  $LaCu_5In$  compound in Fig. V-4 represents the LSQ fit of the measured data to the Bloch – Grüneissen – Mott relation given by:

$$\rho(T) = \rho_0 + \left(\frac{4\kappa}{\theta_R}\right) \left(\frac{T}{\theta_R}\right)^5 \int_0^{\theta_R/T} \frac{x^5 dx}{(e^x - 1)(1 - e^{-x})} - cT^3, \quad V-1$$

where  $\rho_0$  is the residual resistivity originating from the scattering of electrons from defects and impurities. The second term represents the electron – phonon scattering with  $\kappa$  representing the electron – phonon coupling constant and  $\theta_R$  the resistivity Debye temperature. LSQ fit of the resistivity data of the  $LaCu_5In$  to the Eq. V-1 yields the following values  $\rho_0 = 86 \times 10^{-8} \Omega.m$ ;  $\kappa = 2875 \times 10^{-8} \Omega.m/K$ ;  $\theta_R = 143$  K and  $c = 16 \times 10^{-16} \Omega.m/K^3$ . The values of  $\rho_0$ ,  $\kappa$  and  $c$  obtained from the LSQ are large compared to those obtained in ref. [2]. However, the resistivity Debye temperature is comparable to the value of 149 K in [2] as is to be expected for the similar lattice vibration spectra as a consequence of the same atomic mass of La for the two compounds. The residual resistivity ratio of  $LaCu_5In$  ( $RRR = \rho_{300K}/\rho_{4K}$ ) is 1.43 which is relatively small to describe the high degree of crystallinity in this sample and indicates that a large amount of disorder induced scattering at low temperature in the sample. This may also explain the large values obtained for the resistivity parameters  $\rho_0$ ,  $\kappa$  and  $c$ . The magnetic contribution to the total resistivity of each composition was obtained by subtracting

an interpolated  $\rho_{La}(T)$  data of the non-magnetic phonon contribution of  $LaCu_5In$  from  $\rho_i(T)$  of each composition of  $(Ce_{1-x}Tb_x)Cu_5In$  samples:

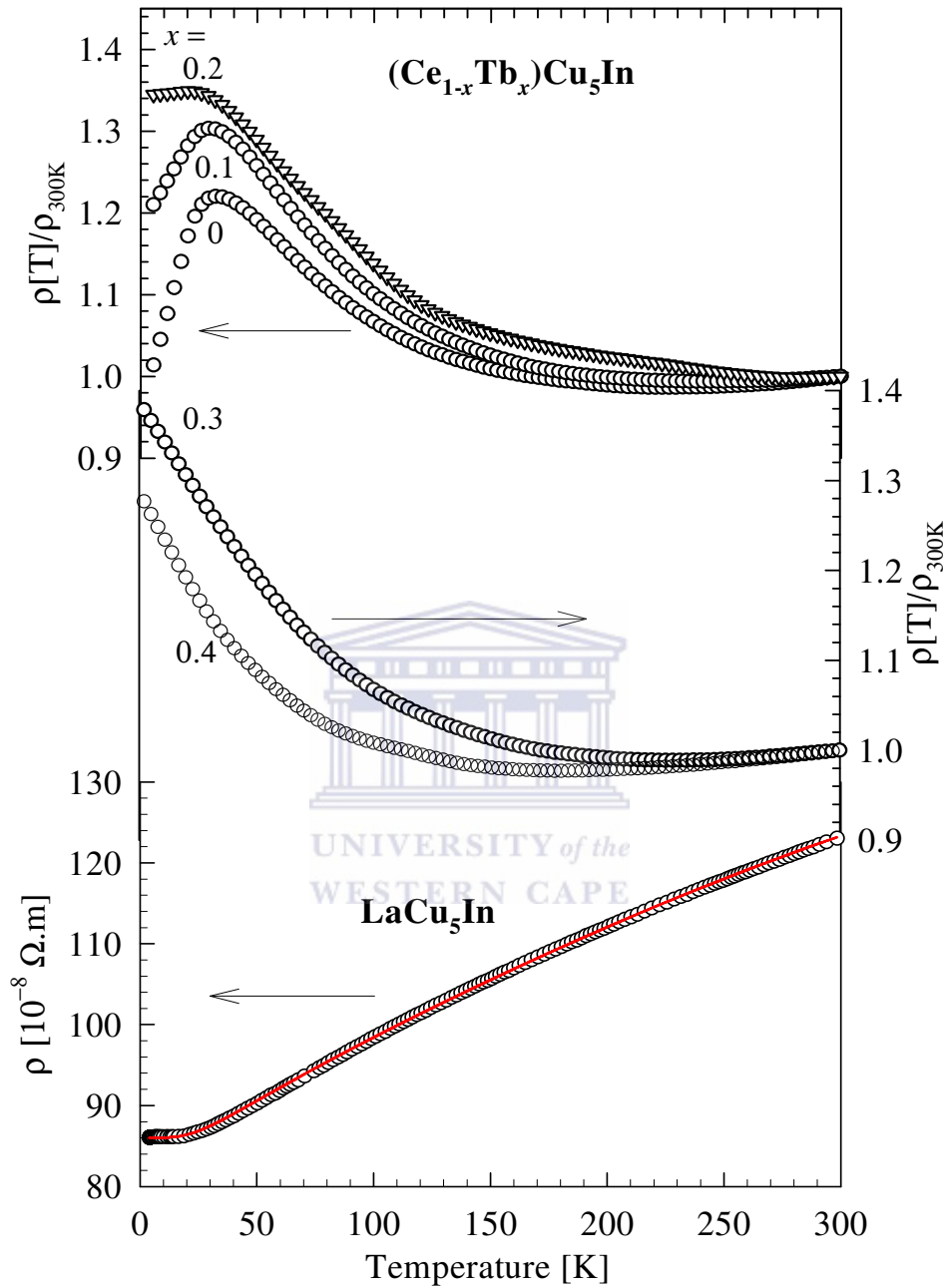


**Figure V-4:** Electrical resistivity normalized to its room temperature value,  $\rho(T)/\rho_{300K}$ , versus temperature  $T$  for various value of  $x$  in the range  $0 \leq x \leq 0.4$  for the  $(Ce_{1-x}Tb_x)Cu_5In$  system. The red solid line through the data points of the  $LaCu_5In$  is the LSQ fits of the measured data to Eq. V-1.

$$\rho_{mag}(T) = \rho_i(T) - (\rho_{La}(T) - \rho_{0La}), \quad V-2$$

where  $\rho_{0La}$  is the temperature independent residual resistivity of the La compound, which comprises the sample defect scattering contributions. The resulting  $\rho_{mag}(T)$  curves are depicted in Fig. V-5 in a logarithmic scale. It is observed that the incoherent single-ion Kondo scattering is characterized by a  $-\ln T$  behaviour at high temperature, for all composition in the range  $0 \leq x \leq 0.4$ . Hence LSQ fits of  $\rho_{mag}(T)$  data at high temperatures to equation:

$$\rho_{mag}(T) = \rho_{spd} \left[ 1 + \alpha N(E_F) J_{sf} \ln \frac{T}{T_k} \right] \approx \rho_{0K} - C_k \ln T \quad V-3$$

are shown by solid lines through the experimental data points in Fig. V-5. In Eq. V-2  $\rho_{0K}$  accounts for the spin-disorder contribution, which is suppressed with the strength of Kondo interaction and  $C_k$  describes the strength of the Kondo interaction, which are mathematically related the value of the Kondo temperature  $T_K$ . As a result of this, an intrinsic value of  $T_K$  cannot be determined unambiguously from the resistivity measurements. The other parameters in Eq. V-3 are defined in chapter 1 (Eq. I-25). LSQ fits give values of  $\rho_0$  and  $C_k$  listed in Table V-7. The observed values of  $C_K$  for the different compositions do not clearly show the suppression of the strength of the Kondo interaction with Ce substitution. In order to observe the suppression of the Kondo interaction with decreasing Ce content, an effort is made to estimate the value of  $T_K$  for the different compositions using Eq. V-3 and another simplified expression of Eq. V-3 given in the form:

$$\rho_{mag}(T) = \rho_{0TK} - C_K \ln \left( \frac{T}{T_K} \right) = (\rho_{0TK} + C_K \ln(T_K)) - C_K \ln(T), \quad V-4$$

where  $\rho_{0TK}$  is the resistivity at very low temperature when  $T \rightarrow 0$ . The combination of Eqs. V-3 and V-4 gives an expression of  $T_K$  in the form:

$$T_K \propto \exp \left[ \frac{\rho_{0K} - \rho_{0TK}}{C_K} \right]. \quad V-5$$

The value of  $C_K$  is obtained for each composition from LSQ fits in Fig. V-3.  $\rho_{0TK}$  is approximated to the value of  $\rho(T)$  at the lowest measured temperature, within the uncertainty of the approximation method use in the thesis. It should be noted that Eq. V-4 is derived from the second – order perturbation theory and is only valid at a temperature well above the Kondo temperature ( $T \gg T_K$ ). For temperatures below  $T_K$  ( $T \leq T_K$ ), the perturbation theory

breaks down [3]. The values of  $T_K$  thus derived from Eq. V-5 are listed in Table V-2 and plotted in Fig. V-6.

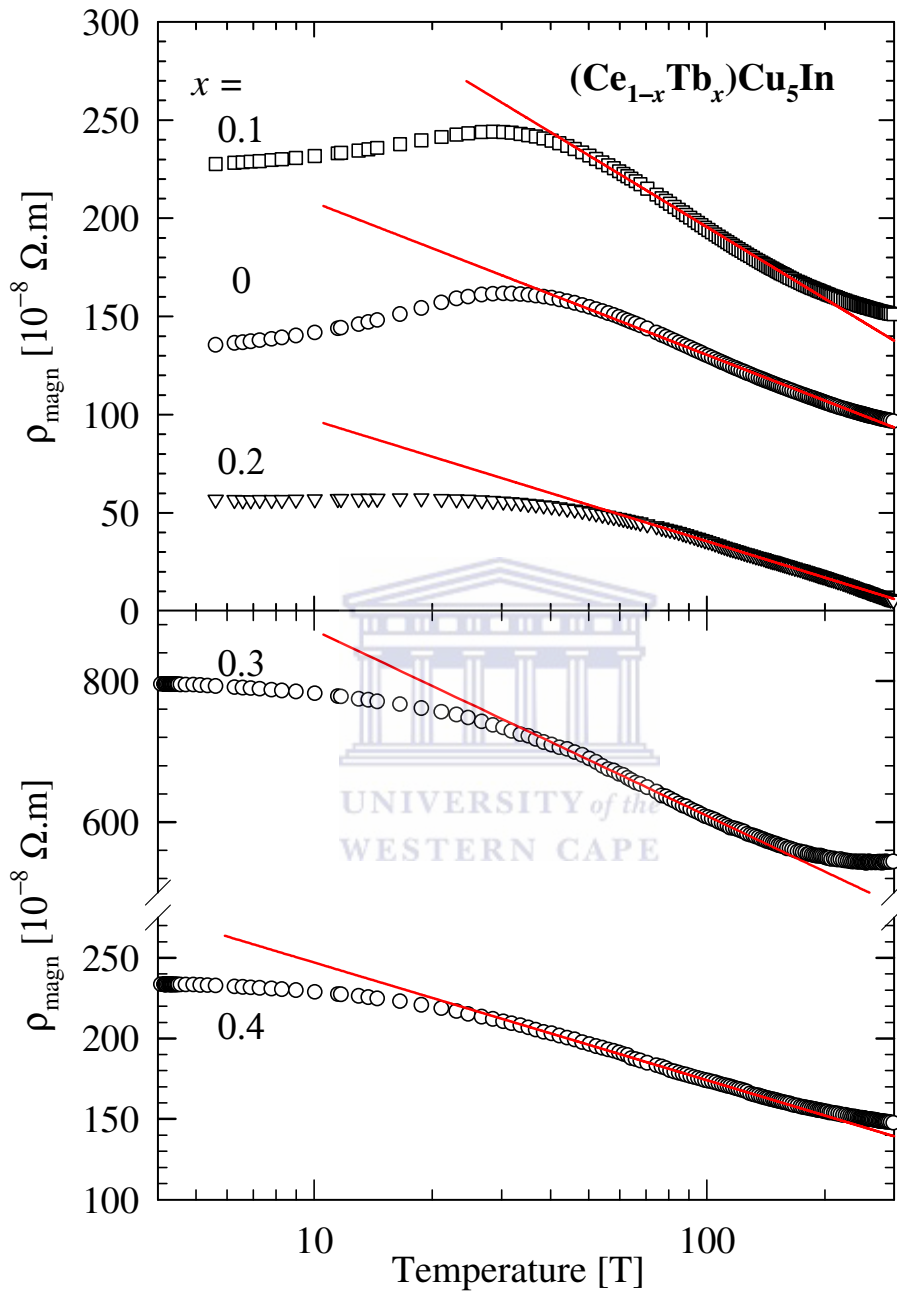


**Figure V-5:** The temperature dependence of the magnetic contribution to the total resistivity for the  $(\text{Ce}_{1-x}\text{Tb}_x)\text{Cu}_5\text{In}$  system shown on semi – log plots. The solid red lines through the data points are least – squares fits of the experimental data to Eq. V-3.



The value of  $T_K$  obtained from this approximation method for the parent compound  $\text{CeCu}_5\text{In}$  is roughly 3 times larger compared to the value of 28 K obtained by Kasaya *et al.* [4] using different approaches. It should be noted that  $T_K$  for Kondo lattice may also be expressed in the form:

$$T_K = \frac{D}{k_B} \exp \left[ -\frac{1}{|\mathfrak{S}_{sf} N(E_F)|} \right], \quad \text{V-5}$$

where the parameters  $D$ ,  $k_B$ ,  $\mathfrak{S}_{sf}$  and  $N(E_F)$  are defined in chapter 1 (Eq. I-26). The on – site exchange interaction  $\mathfrak{S}_{sf}$  is related to the strength of the 4f – electrons and the conduction band hybridization  $V_{sf}$ , which according to Schrieffer – Wolff transformation [5] is given as:

$$\mathfrak{S}_{sf} = \frac{|V_{sf}|^2}{E_F - E_f}, \quad \text{V-6}$$

with  $E_F$  and  $E_f$  being the Fermi and the 4f – energy levels respectively and  $V_{sf}^2$  the hybridization matrix element (chapter I, Eq. I-15). From Eq. V-6, it is evident that the strongest dependence of  $T_K$  is expected to be on the conduction electrons / 4f – electrons hybridization ( $\mathfrak{S}_{sf} \propto V_{sf}^2$ ). This dependence corroborates with the calculated decrease in  $T_K$  with increase in Tb concentration, suggesting the suppression of the Kondo interaction in this system also observed in  $(\text{Ce}_{1-x}\text{RE}_x)\text{Pt}_2\text{Si}_2$  (RE = Tb, Dy) system in chapter 2.

**Table V–2:** The LSQ fits parameters values of the magnetic contribution to the total resistivity for the  $(\text{Ce}_{1-x}\text{Tb}_x)\text{Cu}_2\text{In}$  alloys system using Eq. V-3 and the observed values of  $\rho_{0TK}$  at the lowest measured temperature, as well as the calculated values of  $T_K$  using Eq. V-5.

$x$	$\rho_{0K}[10^{-8}\Omega.\text{m}]$	$C_K[10^{-8}\Omega.\text{m}]$	$\rho_{0TK}[10^{-8}\Omega.\text{m}]$	$T_K$ [K]
0	285(1)	33.7(2)	135.5	87(5)
0.1	438(2)	52.7(4)	227.6	54.2(3)
0.2	158.7(5)	26.8(1)	56.8	44(1)
0.3	1135(3)	114.3(6)	795.7	19.5(8)
0.4	320.1(1)	31.7(1)	233.6	15.3(2)

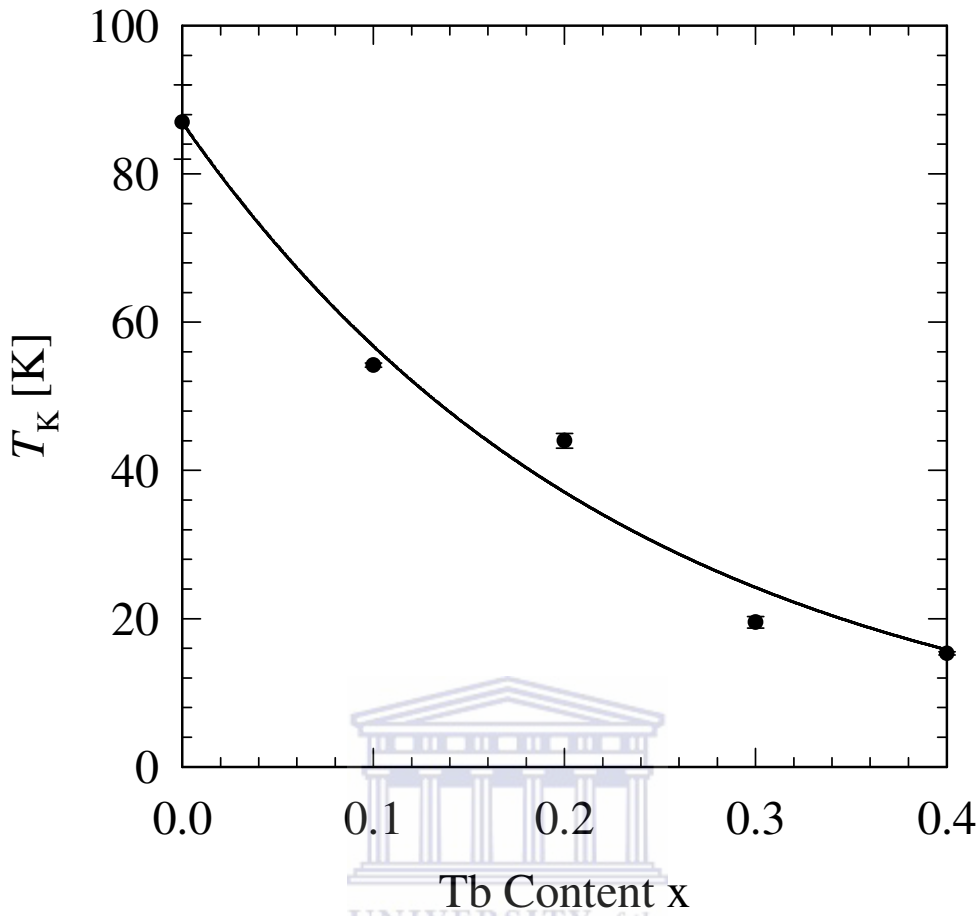


**Figure V-6:** Plot of  $T_K$  against Tb concentration  $x$  for the  $(\text{Ce}_{1-x}\text{Tb}_x)\text{Cu}_5\text{In}$  alloy system. The solid line represents the exponential decrease of  $T_K$  with increasing Tb concentration  $x$ .

### V-3: Magnetization and Magnetic susceptibility

The fields dependence of the magnetization  $\sigma(\mu_0H)$  measured at 1.7 K in field up to 6 T are shown in Fig. V-7 for the pseudo-ternary alloy system  $(\text{Ce}_{1-x}\text{Tb}_x)\text{Cu}_5\text{In}$  with  $0 \leq x \leq 0.4$ . After an initial linear behaviour at lower fields ( $\mu_0H \leq 0.5$  T) all curves shows a downward curvature at higher values of applied field with a tendency toward saturation to the maximum applied field of 6 T. No evidence of metamagnetic behaviour was observed for all compositions.

Results of the inverse magnetic susceptibility  $\chi^{-1}(T)$  measurements in a field of 0.1 T in the temperature range  $2 \leq T \leq 300$  K are depicted for all investigated compositions of the  $(\text{Ce}_{1-x}\text{Tb}_x)\text{Cu}_5\text{In}$  alloy system in Fig.V-8. The applied field of 0.1 T was chosen since for all

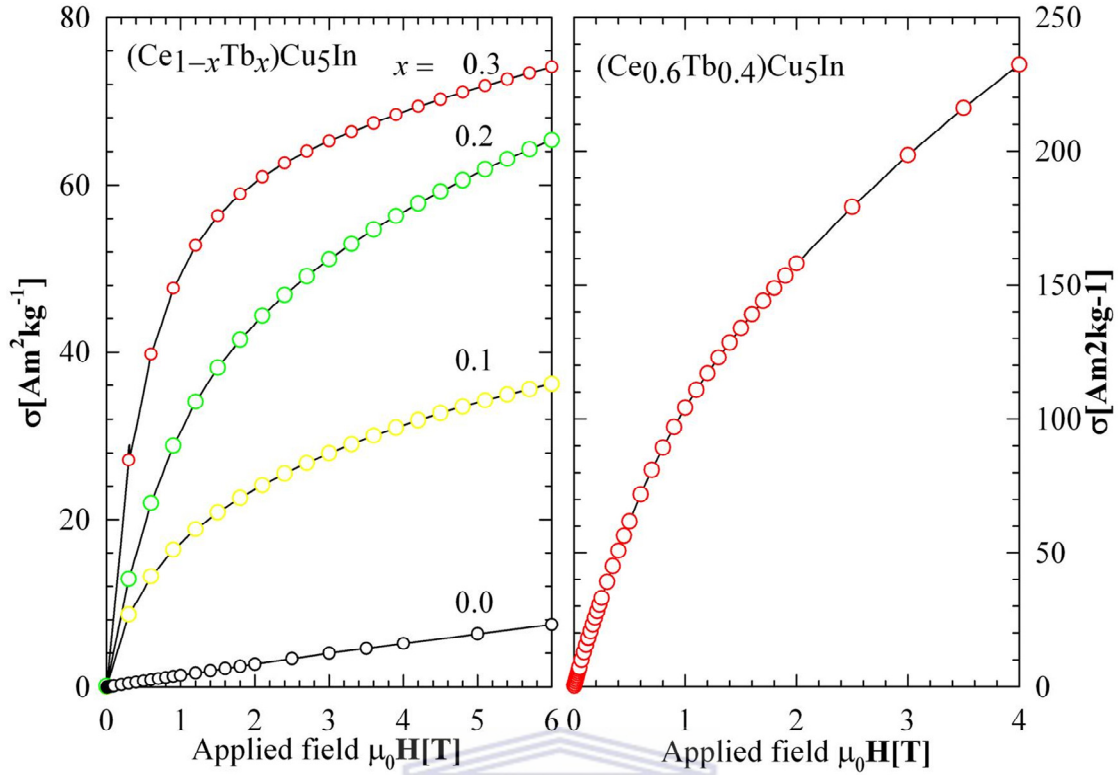


**Figure V-7:** The field variation of the magnetization  $\sigma(\mu_0 H)$  measured at 1.7 K for the alloy system  $(\text{Ce}_{1-x}\text{Tb}_x)\text{Cu}_5\text{In}$  with  $0 \leq x \leq 0.4$ .

compositions in the  $(\text{Ce}_{1-x}\text{Tb}_x)\text{Cu}_5\text{In}$  system,  $\sigma(\mu_0 H)$  curves are linear in this field (Fig.V-7). Above a certain temperature, as shown by solid lines fits, the paramagnetic reciprocal susceptibility obeys a Curie-Weiss relationship:

$$\chi^{-1}(T) = \frac{3k_B(T - \theta_p)}{N_A \mu_{\text{eff}}^2}, \quad \text{V-7}$$

where  $k_B$ ,  $N_A$ ,  $\theta_p$  and  $\mu_{\text{eff}}$  got their usual meaning (see section IV-3-2). LSQ fits of the measured data to Eq. V-8 give values of  $\theta_p$  and  $\mu_{\text{eff}}$  effective listed in Table V-2. Similar to the  $(\text{Ce}_{1-x}\text{RE}_x)\text{Pt}_2\text{Si}_2$  alloy systems (section IV-3-2) and other related systems such as  $(\text{Ce}_{1-x}\text{Gd}_x)\text{Pt}_2\text{Si}_2$  [6],  $(\text{Ce}_{1-x}\text{Gd}_x)\text{Cu}_6$  [7] and  $(\text{Ce}_{1-x}\text{RE}_x)\text{In}_3$  [8], a gradual increase in  $\mu_{\text{eff}}$  is observed between  $\text{CeCu}_5\text{In}$  and  $\text{Ce}_{0.4}\text{Tb}_{0.6}\text{Cu}_5\text{In}$  compounds. As discussed in chapter 4, at higher temperature Ce and Tb ions contribute independently to the total moment. The calculated effective moment based on the independent contributions of Ce and Tb are also listed in Table V-2 and are in reasonable agreement with the observed  $\mu_{\text{eff}}$ .

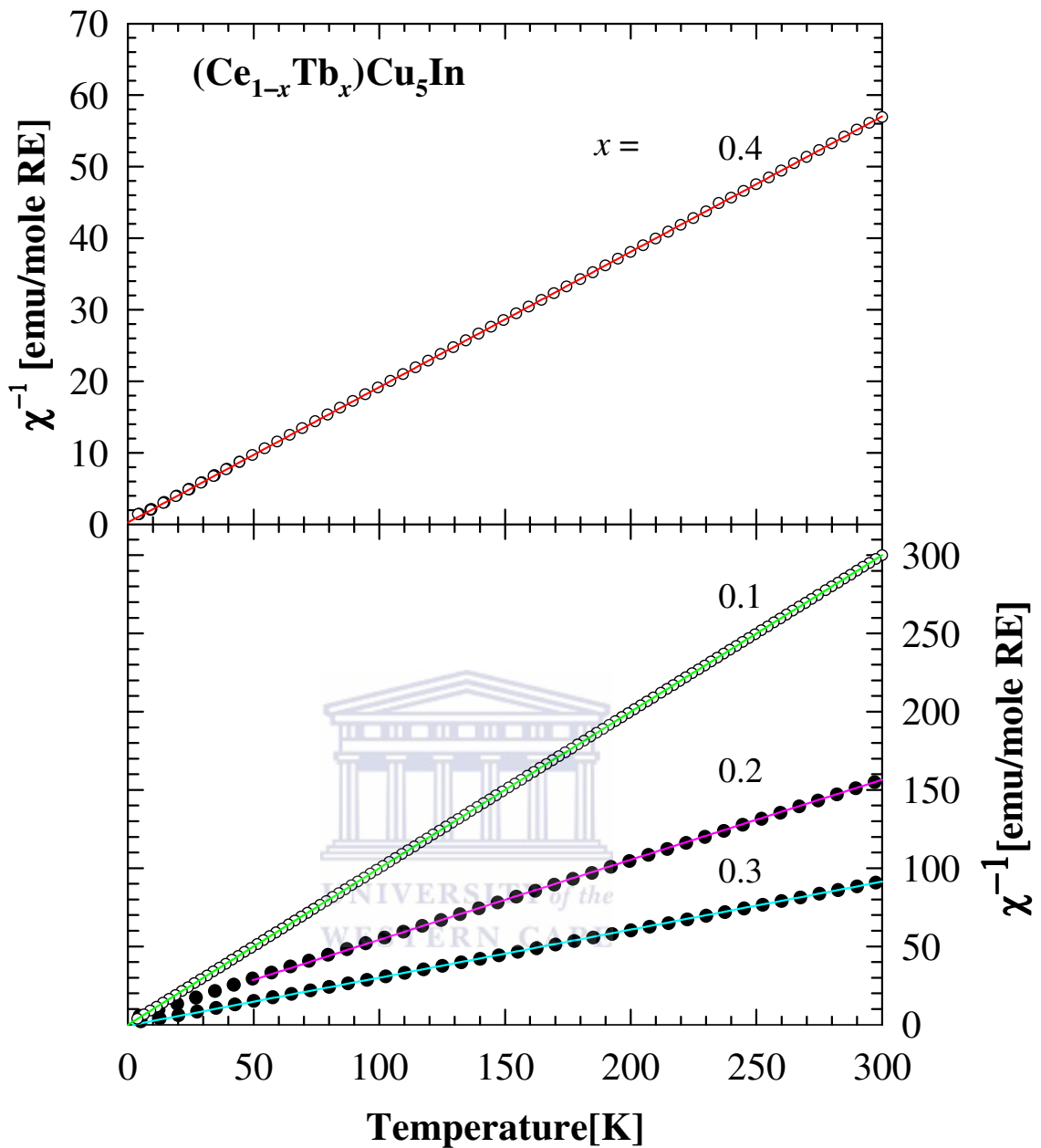


**Figure V-8:** Temperature variation of the inverse susceptibility  $\chi^{-1}(T)$  for  $(\text{Ce}_{1-x}\text{Tb}_x)\text{Cu}_5\text{In}$ . The data refer to a mole of rare-earth atoms. The solid lines through the data points represent LSQ fits of the measured data to a Curie-Weiss relationship (Eq.V-8).

**Table V-3:** Magnetic susceptibility data for the  $(\text{Ce}_{1-x}\text{Tb}_x)\text{Cu}_5\text{In}$ . The effective magnetic moment  $\mu_{\text{eff}}$  as well as the paramagnetic Curie temperature  $\theta_{\text{p}}$  was obtained from LSQ fits of the experimental data in Fig. V-8 to the Curie – Weiss relationship (Eq. V-8). Values of  $\mu_{\text{eff}}$  calculated for the alloys as described in the text are also included for comparison.

$x$	0	0.1	0.2	0.3	0.4
$\theta_{\text{p}}[\text{K}]$	-104(1)	-6.08(1)	2.1(1)	-10.51(3)	-1.70(2)
$\mu_{\text{eff\_Exp}}$	2.65	3.96	5.11	6.72	6.51
$\mu_{\text{eff\_Calc}}$	2.54	3.26	3.98	4.69	5.41

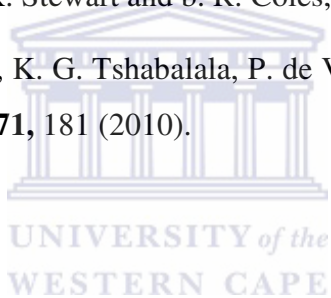
#### V-4: Conclusion

In summary the present study indicates that the  $(\text{Ce}_{1-x}\text{Tb}_x)\text{Cu}_5\text{In}$  alloys retained the orthorhombic  $\text{CeCu}_6$ -type structure with space group  $Pnma$  up to 40% Ce substitution from the XRD results. Furthermore, the resistivity results indicate that, this system evolved from coherent Kondo lattice behaviour for Ce concentrated alloys to incoherent single – ion Kondo behaviour with increasing in Tb content  $x$  up to  $x = 0.4$ . The calculated Kondo temperature for each composition indicates the suppression of the Kondo interaction with increase in Tb content. From the susceptibility and magnetization results, no evidence of magnetic phase transition or metamagnetic behaviour was observed for all compositions in the concentration range of our studies down to 2 K. This suggests the absence of the RKKY interaction and the dominance of the Kondo effect against the large moment bearing substitution of Tb – ions on the Ce – site.

## References:

---

- 1) L. Vegard's, *Z. Phys.* **5**, 17 (1927); *Z. Krist.* **67**, 239 (1928).
- 2) M. B. Tchoula Tchokonté, P. De V. Du Plessis, A. M. Strydom, D. Kaczorowski, A. Czopnik and Z. Kletowski, *J. Phys.: Condens Matter* **16**, 1981 (2004).
- 3) A. C. Hewson "The Kondo problem to heavy – fermions" (1993) Cambridge Press.
- 4) M. Kasaya, N. Satoh, T. Miyazaki and H. Kumazaki, *Physica B* **206 & 207**, 314 (1995).
- 5) J. R. Schrieffer and P. A. Wolff, *Phys. Rev* **149**, 491 (1966).
- 6) M. B. Tchoula Tchokonté, P. de V. du Plessis and D. Kaczorowski, *J. Phys.: Condens. Matter.*, **15**, 3767 (2003).
- 7) S. B. Roy, M. R. Lees G. R. Stewart and b. R. Coles, *Phys. Rev.* **B 43**, 8264 (1991).
- 8) M. B. Tchoula Tchokonté, K. G. Tshabalala, P. de V. du Plessis and D. Kaczorowski, *J. Phys. Chem. of Solids.*, **71**, 181 (2010).



## Chapter VI

---

### Conclusion

In summary, XRD diffraction studies have confirmed the tetragonal  $\text{CaBe}_2\text{Ge}_2$  – type structure with space group  $P4/nmm$  for all compositions in the alloys series  $(\text{Ce}_{1-x}\text{RE}_x)\text{Pt}_2\text{Si}_2$  with  $\text{RE} = \text{Tb}$  or  $\text{Dy}$  while for the alloy series  $(\text{Ce}_{1-x}\text{Tb}_x)\text{Cu}_5\text{In}$ , the orthorhombic  $\text{CeCu}_6$  – type structure with space group  $Pnma$  only extend up to 40 % Ce substitution.

The studies of electrical resistivity of all the systems investigated, shows coherent effect at large Ce – concentration alloys ( $x \leq 0.2$ ) and incoherent effect in the concentration range  $x \geq 0.3$ . The evolution from coherent Kondo scattering to incoherent single – ion Kondo scattering, corresponding to the decrease of the temperature of the resistivity maximum  $T_{\text{max}}$ , hence  $T_{\text{K}}$  (since  $T_{\text{max}}$  is often related to  $T_{\text{K}}$ ) with the decrease in RE content is associate with the reduction of Ce content, responsible of the Kondo effect. Indeed the increases of Tb or Dy ion increase the number of 4f – electrons which is expected to increase the RKKY interaction. As a result of this the Kondo interaction strength decreases going from  $\text{CePt}_2\text{Si}_2$  or  $\text{CeCu}_5\text{In}$  to  $\text{REPt}_2\text{Si}_2$  or  $(\text{Ce}_{0.6}\text{Tb}_{0.4})\text{Cu}_5\text{In}$ .

Magnetic properties studies indicate antiferromagnetic ordering at concentrated Tb – alloys ( $0.7 \leq x \leq 1$ ) only for the  $(\text{Ce}_{1-x}\text{Tb}_x)\text{Pt}_2\text{Si}_2$  system, with a Néel temperature in the range  $3.4 \text{ K} \leq T_{\text{N}} \leq 8.0 \text{ K}$ . No evidence of magnetic phase transition was observed for the alloy systems  $(\text{Ce}_{1-x}\text{Tb}_x)\text{Pt}_2\text{Si}_2$  and  $(\text{Ce}_{1-x}\text{Tb}_x)\text{Cu}_5\text{In}$ . The magnetization results reveal no evidence of metamagnetic behaviour for the three systems.

The common remarkable feature of all the systems investigates, is the robustness of the Kondo properties against large moment bearing substitution of Tb – and Dy – ions on the Ce site.